Developments for the ^{6}He $\beta - \bar{\nu}$ angular correlation experiment

David W. Zumwalt

A dissertation
submitted in partial fulfillment of the
requirements for the degree of

Doctor of Philosophy

University of Washington

2015

Reading Committee:

Alejandro García, Chair

Peter Mueller

Subhadeep Gupta

Program Authorized to Offer Degree:
UW Physics

University of Washington

Abstract

Developments for the ^{6}He $\beta - \bar{\nu}$ angular correlation experiment

David W. Zumwalt

Chair of the Supervisory Committee:
Professor Alejandro García
Physics

This thesis describes developments toward the measurement of the angular correlation between the beta and the antineutrino in the beta decay of ^{6}He. This decay is a pure Gamow-Teller decay which is described in the Standard Model as a purely axial vector weak interaction. The angular correlation is characterized by the parameter $a_{\beta\nu} = -1/3$ in the Standard Model. Any deviation from this value would be evidence for tensor components in the weak interaction and would constitute new physics.

A new method will be used to measure the parameter $a_{\beta\nu}$ from ^{6}He decays, featuring a magneto-optical trap that will measure the beta particle in coincidence with the recoiling ^{6}Li daughter ion. This neutral atom trapping scheme provides cold, tightly confined atoms which will reduce systematic uncertainties related to the initial position of the decay. By knowing the initial position of the decay and measuring the time of flight of the recoiling ^{6}Li daughter ion in coincidence with the beta, the angular correlation between the beta and the antineutrino can be deduced. We aim to measure $a_{\beta\nu}$ first to the level of 1%, and eventually to the 0.1% level, which would represent an order of magnitude improvement in precision over past experiments.

Towards this goal, we have designed, built, and successfully tested a liquid lithium target to provide $> 2 \times 10^{10}$ ^{6}He atoms/s to a low-background environment, which is the most intense source of ^{6}He presently available. This allowed for an additional

measurement of the ^{6}He half-life ($806.89 \pm 0.11_{stat}{}^{+0.23}_{-0.19 syst}$ ms) to be made with unprecedented precision, resolving discrepancies in past measurements. We have also tested our trapping and detection apparatus and have begun to record preliminary coincidence events.

Table of Contents

List of Figures

List of Tables

Acknowledgments

Performing my PhD research at the University of Washington has afforded me many opportunities to work on interesting projects and to expand my idea about what it means to do science and to be a scientist. In part, this is due to the fantastic facilities we are privileged to have at the Center for Experimental Nuclear Physics and Astrophysics (CENPA), and the general attitude of encouraging students to learn how to machine parts or to use a laser cutter, even if one uses them more often to create Batarangs than to move the experiment forward. More principal to my education and fulfillment, however, were the many people with whom I was fortunate to spend my time and to whom I owe a great many thanks.

I must first thank my thesis advisor, Alejandro García, for his patience and enthusiasm for physics. He was always in the lab and available for questions. He troubleshoots your problems as if they were his own, and I appreciated his willingness to work alongside his students.

I want to thank Peter Mueller for being a wonderful mentor and friend, and I am greatly indebted to him for both his academic as well as financial support. He taught me everything I know about atomic physics, and anything I don't know is not for a lack of trying on his part. He is the hardest working physicist I know, and has spent nearly as much time reading, re-reading, and remarking on this thesis as I have spent writing it. His constant optimism is remarkable, and he showed me it's possible to

still be happy after a 12 hour day of unsuccessfully trying to get a laser trap working, though I still don't actually know how he does it. Thank you, Peter, for all the help you've given me at Argonne and at CENPA.

I am grateful to Derek Storm, who has been a constant source of guidance and support through both academic hurdles as well as injuries. His humor is made even more funny by how dry it is, and it took me several months before I learned to pause for a moment after he spoke just in case he was making a joke that would have gone over my head. They still sometimes do, but I appreciate them after the fact. He is very practical, and is always able to ground our group discussions with insightful observations to keep them from veering too far off course, and I admire that about him.

Greg Harper in his retirement is dearly missed at CENPA. He taught me how to operate the Van de Graaff accelerator and its principles with clarity and humor, and whenever I needed to know how to build, well, anything, Greg was the first person I asked - partially because his explanations were concise and he always told me exactly, and only, what I wanted to know, but also because I think it bugged him to be asked so many questions all the time, and it's great fun to bother Greg. His off-color humor is absolutely hilarious and I'm grateful to have occasionally been the subject of his many jokes. It's Dr. Zoom now, Greg.

I couldn't have asked for better post-docs than Matt Sternberg, Arnaud Leredde, and Andreas Knecht. Each of them has shown me a different way to approach problems both in the lab and in life. The experiment is in good hands with my fellow group members Ran Hong and Yelena Bagdasarova. I enjoyed many riddle-solving discussions with Ran, Tim Major, and Rachel Osofsky that helped to break up the day when writing was going nowhere. Finally, I would like to thank the entire administrative and technical staff at CENPA who are the backbone of every experiment.

Dedication

To my parents, for their years of support, encouragement, and love.

Chapter 1

Introduction

1.1 The History of beta decay

In 1899 Rutherford followed Becquerel's investigations of radiation emitted from uranium, which Becquerel discovered when a photographic plate was accidentally exposed in the presence of uranium. Rutherford's studies led to the coining of two kinds of "rays." Alpha rays could be easily stopped and would not expose the photographic plate if the plate was wrapped in paper. Beta rays were much more penetrating and could go through considerable thicknesses of metal and other materials. In 1900 Becquerel was able to measure the charge-to-mass ratio of the beta rays by means of a magnetic field and determined that they were in fact electrons [1].

Curiously, the beta rays were measured to be emitted over a wide energy range, in contrast to previous observations with alpha and gamma rays whose energies were equal to the differences between the initial and final nuclear energy states. This apparent violation of the conservation of energy was a source of considerable controversy within the physics community. Bohr concluded that the dearly held energy conservation law may only be true in the statistical sense, but may be violated in individual decays. Calorimetry measurements made by Ellis and Wooster in 1927 [2] confirmed that the spectrum was truly continuous and that the previous measurements were

not simply an error due to the betas losing energy elsewhere, as was suggested by Rutherford and others.

The situation was made hairier due to the fact that angular momentum was also apparently violated in these decays, since the 1/2 integer spin carried away by the beta did not match the integer changes in angular momentum observed in nuclei. It wasn't until 1930 that Pauli solved both of these problems by suggesting a neutral, spin 1/2, highly penetrating, nearly or perhaps entirely massless particle is also involved in beta decays, which he called a neutron. Two years later, Chadwick discovered what we now call a neutron [3], prompting Fermi to suggest Pauli rename his particle to a neutrino. While this proposal set off a chain reaction of theoretical development, it would not be until 1956 before Cowan and Reines directly detected the neutrino experimentally [4].

1.2 The Fermi Model

After Pauli's suggestions, Fermi began to formulate this four-particle interaction following Dirac's recent developments in quantum electrodynamics. He imagined a point contact, four fermion vector-vector interaction in analogy with the vector interaction describing the electromagnetic interaction (see Figure 1.1).

$$\mathcal{L}_\beta = \frac{G_F}{\sqrt{2}}(\bar{\psi}_p\gamma^\mu\psi_n)(\bar{\psi}_e\gamma_\mu\psi_\nu) + h.c. \tag{1.1}$$

The interaction is composed of currents of hadrons and leptons mediated by a γ^μ vector operator, where γ_μ is one of the Dirac matrices. This warrants comparison with the electromagnetic interaction which inspired Fermi's formulation.

$$\mathcal{L}_{EM} = e(\bar{\psi}_p\gamma^\mu\psi_p)A_\mu \tag{1.2}$$

The differences here are small. There is a change in the coupling strength from e to $\frac{G_F}{\sqrt{2}}$, and instead of a gauge boson A_μ there is an additional vector current $\bar{\psi}_e\gamma_\mu\psi_\nu$.

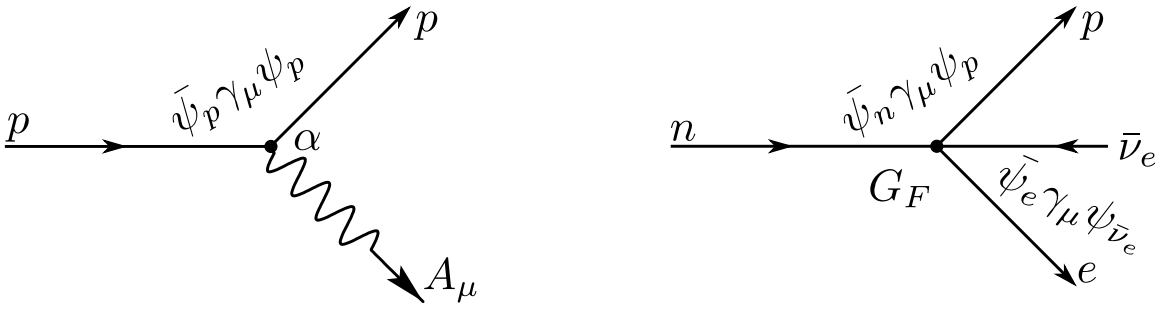

Figure 1.1: Electromagnetic interaction (left) compared with Fermi's model of beta decay (right).

Fermi used perturbation theory under the assumption that this new interaction was weak to derive a differential decay rate which would govern β decay (given in natural units):

$$P(E_e)dE_e = \frac{G_F^2}{(2\pi)^5}|\mathcal{M}_{fi}|^2 F(Z, E_e) E_e (E_0 - E_e)^2 \sqrt{E_e^2 - m_e^2} dE_e \tag{1.3}$$

where E_e is the β energy, E_0 is the endpoint energy, $F(Z, E_e)$ is the Fermi function which accounts for the electrical interaction between the charged β particle and the daughter nucleus that distorts the energy spectrum, and can be written as follows [5]:

$$F(Z, E_e) = \frac{2(1+S)}{((2S)!)^2}(2p_e\rho)^{2S-2} e^{\pi\eta} |(S - 1 - i\eta)!|^2 \tag{1.4}$$

where $S = \sqrt{1-(\alpha Z)^2}$, $\rho = R/(\hbar/m_e c)$, $\eta = \pm Z e^2 E_e/\hbar c^2 p_e$, Z is the charge of the daughter nucleus, R is the nuclear charge radius, and α is the fine structure constant. G_F is the Fermi coupling constant which characterizes the strength of the interaction, and $\mathcal{M}_{fi}$ is the matrix element for the decay.

Fermi's intuitive description has stood the test of time with few amendments. By the time Fermi had published his theory, Pauli had shown that there could be at most five interaction forms that could satisfy Lorentz invariance: Scalar (S), Pseudoscalar (P), Vector (V), Axial Vector (A), and Tensor (T) (see Table 1.1).

Type	Operator	Parity
Scalar, S	1	+
Pseudoscalar, P	γ_5	−
Vector, V	γ_μ	−
Axial Vector, A	$\gamma_\mu\gamma_5$	+
Tensor, T	$\gamma_\mu\gamma_\nu - \gamma_\nu\gamma_\mu$	N/A

Table 1.1: All possible Lorentz-invariant operators

While in general it cannot be said that there are no pseudoscalar contributions to the weak interaction, or even that the coupling strength is small, it can be shown that these possible contributions vanish in the nonrelativistic limit present for beta decay, where the typical energies (MeV) are much smaller than the mass of the nucleons (GeV). Gamow and Teller went on to show that the possible operators involved in the weak interaction generate specific nuclear spin selection rules in the low-energy case of nuclear beta decay. The Scalar and Vector operators cannot change the spin of the nucleus, and so for these interactions, $\Delta J = 0$. These are the so-called Fermi decays, named so due to his intuitions about the vector form of the interaction. The Tensor and Axial Vector operators have their own rules, $\Delta J = 0, \pm 1$ except for the $0 \rightarrow 0$ case, which is only allowed for Fermi decays. These decays are named Gamow-Teller decays, and it is these decays about which this thesis is concerned.

1.3 Beyond the Fermi Model

At this time, there wasn't enough experimental evidence to eliminate Axial Vector, Scalar, or Tensor interactions from the Hamiltonian, and so in general they needed to be added. Furthermore, the implicit assumption that the weak interaction, like

the strong interaction and the electromagnetic interaction before it, was parity conserving came into question in the 1950s when Lee and Yang surveyed the existing experiments and found that parity had never been tested to be conserved in the weak interaction [6]. They suggested a set of experiments which could test this property. One such experiment was carried out by Wu and collaborators [7] by measuring the beta asymmetry in the decay of spin-polarized ^{60}Co, which confirmed the presence of parity violations when it was discovered that the direction of beta emission tended to be opposite the direction of the spin of the nucleus. While the momentum vector $\vec{p}_\beta$ would reverse under a parity transformation, the spin of the nucleus $\vec{J}_{^{60}\mathrm{Co}}$ would not. This result was quickly followed up by a similar experiment measuring the beta asymmetry in the decay chain of $\pi^\pm \to \mu^\pm \to e^\pm$. Thus, the weak interaction is unique among the fundamental forces in that it discriminates between the left-handedness and right-handedness of the involved particles.

Including all parity conserving and violating interaction terms, we can write out the most general form of the Hamiltonian

$$\begin{aligned}
\mathcal{H}_{int} &= (\bar{\psi}_p\psi_n)(C_S\bar{\psi}_e\psi_\nu + C'_S\bar{\psi}_e\gamma_5\psi_\nu) \\
&+ (\bar{\psi}_p\gamma^\mu\psi_n)(C_V\bar{\psi}_e\gamma_\mu\psi_\nu + C'_V\bar{\psi}_e\gamma_\mu\gamma_5\psi_\nu) \\
&+ \frac{1}{2}(\bar{\psi}_p\sigma^{\lambda\mu}\psi_n)(C_T\bar{\psi}_e\sigma_{\lambda\mu}\psi_\nu + C'_T\bar{\psi}_e\sigma_{\lambda\mu}\gamma_5\psi_\nu) \\
&- (\bar{\psi}_p\gamma^\mu\gamma^5\psi_n)(C_A\bar{\psi}_e\gamma_\mu\gamma_5\psi_\nu + C'_A\bar{\psi}_e\gamma_\mu\psi_\nu) \\
&+ (\bar{\psi}_p\gamma^5\psi_n)(C_P\bar{\psi}_e\gamma_5\psi_\nu + C'_P\bar{\psi}_e\psi_\nu) + h.c. \qquad (1.5)
\end{aligned}$$

The parity violating experiments were not just consistent with parity violation, but with maximum parity violation. If we assume that the couplings C and C' are the same we can see the source of this parity violation by rewriting the Hamiltonian

in the following way

$$\begin{aligned}
\mathcal{H}_{int} &= C_S(\bar{\psi}_p\psi_n)(\bar{\psi}_e(1+\gamma_5)\psi_\nu) \\
&+ C_V(\bar{\psi}_p\gamma^\mu\psi_n)(\bar{\psi}_e\gamma_\mu(1+\gamma_5)\psi_\nu) \\
&+ \frac{C_T}{2}(\bar{\psi}_p\sigma^{\lambda\mu}\psi_n)(\bar{\psi}_e\sigma_{\lambda\mu}(1+\gamma_5)\psi_\nu) \\
&- C_A(\bar{\psi}_p\gamma^\mu\gamma^5\psi_n)(\bar{\psi}_e\gamma_\mu\gamma_5(1+\gamma_5)\psi_\nu) \\
&+ C_P(\bar{\psi}_p\gamma^5\psi_n)(\bar{\psi}_e\gamma_5(1+\gamma_5)\psi_\nu) + h.c.
\end{aligned}$$

Under the convention that $\gamma_5 = i\gamma_0\gamma_1\gamma_2\gamma_3$, the operator $P_L = \frac{(1+\gamma_5)}{2}$ can be shown to project only the left-handed chirality states of the Dirac spinor of the neutrino, and so parity is maximally violated in the weak interaction when $C = C'$. It can further be shown that $P_L^2 = P_L$, so that introducing any number of $1+\gamma_5$ operators into the lepton current should only change the current by a multiplicative constant to be absorbed by redefinition of C and C'. The γ_5 matrix anticommutes with all other γ_μ matrices, such that $\gamma_\mu\frac{(1+\gamma_5)}{2} = \gamma_\mu P_L = \frac{(1-\gamma_5)}{2}\gamma_\mu = P_R\gamma_\mu$. In addition, the Dirac spinor is defined such that $\bar{\psi} = \psi^\dagger\gamma_0$. Therefore, just as we can write $P_L\psi_\nu = \psi_\nu^L$, we can also write $\bar{\psi}_e P_L\psi_\nu = \psi_e^\dagger\gamma_0 P_L P_L\psi_\nu = \psi_e^\dagger P_R\gamma_0 P_L\psi_\nu = \bar{\psi}_e^R\psi_\nu^L$. The example just used is precisely the form of the scalar current, implying that scalar currents couple opposing chirality states between the electron and the neutrino. A similar line of reasoning will show that this is true for tensor currents as well, while vector, axial vector, and pseudoscalar currents all couple the same chirality states for the electron and the neutrino. This will have consequences when discussing angular correlations in beta decay.

Ignoring the pseudoscalar currents in the non-relativistic regime of beta decay, we can separate the Hamiltonian into two general forms according to how they couple to chirality states of the leptons: a vector and axial vector Hamiltonian, and a scalar

and tensor Hamiltonian

$$\mathcal{H}_{int} = \sum_{i=V,A} (\bar{\psi}_p O^i \psi_n)((C_i + C_i')\bar{\psi}_e^L O_i \psi_\nu^L + (C_i - C_i')\bar{\psi}_e^R O_i \psi_\nu^R) \quad (1.6)$$

$$\mathcal{H}_{int} = \sum_{i=S,T} (\bar{\psi}_p O^i \psi_n)((C_i + C_i')\bar{\psi}_e^R O_i \psi_\nu^L + (C_i - C_i')\bar{\psi}_e^L O_i \psi_\nu^R) \quad (1.7)$$

1.4 The Standard Model

An early experiment in 1955 studying the beta decay of ^{6}He by measuring the coincidence rate between recoil ions and betas of a selected energy as a function of the angle between the particles found that the interaction was mediated purely by tensor currents [8]. However this experiment was later shown to be prone to systematic effects which reversed the result to being purely axial vector. After a number of followup experiments studying the decays of ^{6}He, ^{23}Ne, and ^{35}Ar [9, 10, 11], a picture began to emerge of a weak interaction which is of a purely axial vector and vector form.

The modern view of the weak interaction in the Standard Model is one which is mediated purely by left-handed gauge bosons (Eqn. 1.6). Unlike the electromagetic interaction, which is mediated by one massless boson which we call the photon, the weak interaction is mediated by three: two charged bosons, the $W^{\pm}$, whose masses are approximately 80 GeV/c^2, and one neutral boson, the Z, whose mass is approximately 91 GeV/c^2. It is due to the large masses of these mediators that the interaction governing β decay is so weak, as the range of a force is inversely proportional to the mass of the mediator ($R \propto 1/M_W$), and coupling strength is inversely proportional to the square of this mass($G_F \propto 1/M_W^2$). In the case of electromagnetism, the massless photon results in an infinitely long range force, while the weak interaction is limited to ranges of $\sim 10^{-3}$ fm. This extremely short range, coupled with the relatively low

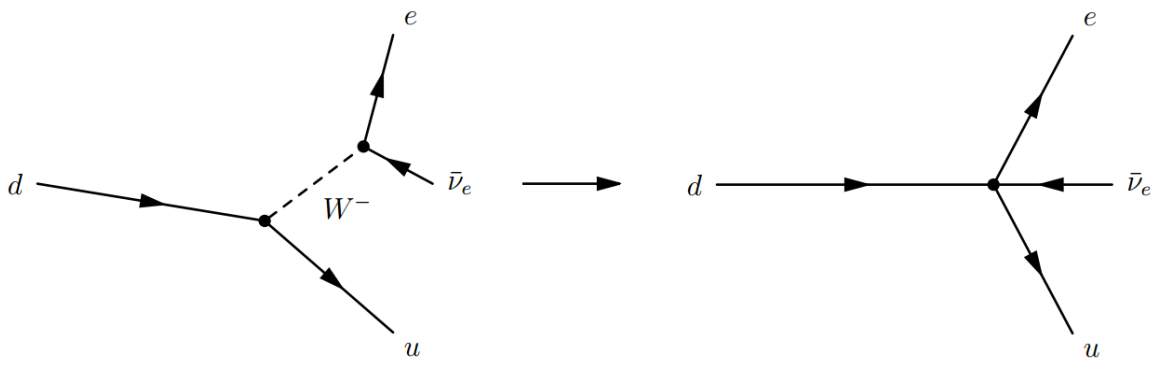

Figure 1.2: In the low energy limit of beta decay, the short range of the $W^{\pm}$ boson behaves the same as Fermi's contact interaction.

energies involved in β decay which result in slow-moving nuclei, means that the more complete Feynman diagram describing the interaction can be reduced to a point-like interaction which explains the remarkable success Fermi achieved using this model (see Figure 1.2).

In equations 1.6 and 1.7, the coefficients C_i and C_i' represent the relative amplitudes of each interaction, and C and C' can be different from each other depending on parity. In general these coefficients can be complex. Under maximum parity violation, however, their magnitudes are equal. Reference [12] gives a treament of these coefficients and shows that in the Standard Model, these coefficients resolve to two real coefficients, $C_A = C_A'$ and $C_V = C_V'$. All other terms are zero.

These coupling constants must ultimately be determined by experiment and cannot be determined from theory. From the experimental literature, limits have been placed on each of the coupling constant ratios (see Table 1.2) [13].

Jackson, Treiman, and Wyld [14] connected these coefficients to observables in the differential beta decay rate, which for an unpolarized nucleus is given as follows

$$\frac{d\Gamma}{dE_\beta d\Omega_\beta d\Omega_\nu} \propto F(Z, E_\beta) p_e E_e (E_0 - E)^2 \left(1 + a_{\beta\nu} \frac{\boldsymbol{p}_e \cdot \boldsymbol{p}_\nu}{E_e E_\nu} + b_{\text{Fierz}} \frac{m_e}{E_e}\right) \tag{1.8}$$

$$-1.272 < C_A/C_V < -1.265$$
$$-0.064 < C_S/C_V < 0.066$$
$$-0.064 < C'_S/C_V < 0.065$$
$$-0.077 < C_T/C_A < 0.086$$
$$-0.077 < C'_T/C_A < 0.087$$

Table 1.2: Experimental limits on coupling constant ratios from Ref. [13].

where m_e is the mass of the β, E_e its energy, p_e its momentum, E_0 the $\beta-$endpoint, p_ν and E_ν the momentum and energy of the antineutrino, respectively, and $F(Z, E_\beta)$ is again the Fermi function for the nucleus of interest. The Fierz interference term, b_{Fierz}, accounts for the interference between axial-vector and tensor couplings when squaring the matrix element $\mathcal{M}_{fi}$. The term $a_{\beta\nu}$ is the angular correlation coefficient between the beta and the antineutrino, and its determination is the focus of this thesis. According to Jackson, Treiman, and Wyld, this coefficient can be written in the form of the C_i and C'_i coefficients for a pure Gamow-Teller decay:

$$a_{\beta\nu} = \frac{1}{3}\left(\frac{|C_T|^2 + |C'_T|^2 - |C_A|^2 - |C'_A|^2}{|C_T|^2 + |C'_T|^2 + |C_A|^2 + |C'_A|^2}\right) \tag{1.9}$$

which under the assumption that $|C_i| = |C'_i|$ reduces to

$$a_{\beta\nu} = -\frac{1}{3}\left(\frac{|C_A|^2 - |C_T|^2}{|C_A|^2 + |C_T|^2}\right) \tag{1.10}$$

In the Standard Model, of these two coefficients only $C_A \approx -1.27$ is non-zero, yielding $a_{\beta\nu} = -1/3$. Therefore the presence of any tensor currents will make the true value of $a_{\beta\nu}$ deviate from this result in the positive direction. This result can also be understood from simple helicity arguments. Consider an example consistent with the Standard Model of a pure Fermi decay, *i.e.* with the change of the nuclear spin $\Delta M = 0$. In this case, to conserve angular momentum the beta and the antineutrino

must have their spins anti-aligned in the final state, as each of these leptons has $J = 1/2$. Both leptons are left-handed chirally, but the beta is a particle and the antineutrino is an antiparticle. This means that in the limit of high energy, the helicity of the beta will tend to be negative, such that its spin along an axis of quantization tends to point opposite its motion. The helicity of a left-handed antiparticle, such as the antineutrino, will tend to be positive in the limit of high energy. Since the antineutrino is essentially massless, we can take its helicity to be positive. If we take the direction of the antineutrino to be the quantization axis $+z$, then the spin of the antineutrino will also be in the $+z$ direction. From elementary quantum mechanics it is known that if a particle has its spin aligned opposite with its motion and is emitted at some angle θ relative to the quantization axis, then the probability that you will measure the spin to be in the $+z$ direction is equal to $\sin^2\theta/2$. Likewise, the probability of measuring it with spin in the $-z$ direction is $\cos^2\theta/2$. However, this assumes that the particles spin is always in the opposite direction of its motion. For massive particles, such as the β, the helicity is velocity dependent, since an observer who measures a positive helicity for a particle could boost past that particle and suddenly see a negative helicity. The probability of measuring the spin of the β to be opposite the direction of the spin of the antineutrino must therefore incorporate the probability of having a positive or negative helicity. This probability is for left-handed particles proportional to $1 - p/E$ for positive helicities, and $1 + p/E$ for negative helicities. Incorporating both probabilities yields the total probability of a β emitted at an angle θ being measured to have its spin opposite the direction of the antineutrino, and therefore satisfying the non-spin-flip condition $\Delta M = 0$, which can be written as

$$(1 + \frac{p_e}{E_e})\cos^2\theta/2 + (1 - \frac{p_e}{E_e})\sin^2\theta/2 = 1 + \frac{p_e}{E_e}\cos\theta \tag{1.11}$$

which is equivalent to

$$1 + \frac{\boldsymbol{p}_e}{E_e} \cdot \frac{\boldsymbol{p}_\nu}{E_\nu} \tag{1.12}$$

These same arguments can be applied to the case where a nucleon does flip its spin, requiring the two leptons to carry off 1 unit of angular momentum. In this case the resulting probability is given by

$$1 - \frac{\boldsymbol{p}_e}{E_e} \cdot \frac{\boldsymbol{p}_\nu}{E_\nu} \tag{1.13}$$

As mentioned, equation 1.12 is applicable to pure Fermi decays. From this we can see that $a_{\beta\nu} = +1$ for these decays. However, in this thesis we are interested in pure Gamow-Teller decays, and in particular the decay of ^{6}He. Here $\Delta J = 1$, such that the two leptons are in a triplet state after emission since $\Delta M = -1, 0, 1$. In this case there are two transitions which flip the spin of a nucleon, and one that does not flip the spin. Because each of these transitions is equally populated, the angular correlation is the average of these cases, resulting in $a_{\beta\nu} = -1/3$ for pure Gamow-Teller decays.

Each of these arguments were presented under the assumption that we are dealing with left-handed leptons, consistent with the Standard Model. However, equation 1.7 demonstrates that scalar and tensor interactions couple opposite chirality states. Therefore all of these helicity arguments invert, such that for purely scalar interactions, $a_{\beta\nu} = -1$, and for purely tensor interactions, $a_{\beta\nu} = +1/3$. We therefore have an observable handle on whether or not interactions outside the Standard Model contribute to weak decays.

Experimentally, b_{Fierz} (see Eq. 1.8) has been determined to be consistent with the Standard Model prediction of 0 [15]:

$$b_{\text{Fierz}} = -(C_S + C'_S)/C_V = -0.0022(26) \tag{1.14}$$

however a non-zero Fierz term would also modulate the decay spectrum, and therefore our observable modulation should more properly be expressed as

$$\tilde{a} \simeq \frac{a_{\beta\nu}}{1 + b_{\text{Fierz}} \frac{m_e}{E_e}} \tag{1.15}$$

1.5 Past measurements

Past angular correlation measurements can provide context for understanding the benefits and challenges different methods introduce, and to motivate our own experimental methods. Table 1.3 compiles several historical angular correlation measurements. Briefly described here are a few of the most precise angular correlation measurements for both tensor and scalar currents to date.

Table 1.3: Compilation of several previously measured $a_{\beta\nu}$ values listed chronologically.

Year	Isotope	Decay type	Method	Trap	SM value	Value	Error	Reference
1963	^{6}He	β^-, GT	Recoil spectrum	No	$-\frac{1}{3}$	-0.3308	0.003	[16],[17]
1963	^{23}Ne	β^-, GT	Recoil spectrum	No	$-\frac{1}{3}$	-0.33	0.03	[18]
1978	n	β^-, F/GT	Recoil spectrum	No	-0.1	-0.1017	0.0051	[19]
1997	^{18}Ne	β^+, F	γ Doppler shift	No	1	1.06	0.095	[20]
1999	^{32}Ar	β^+, F	Proton spectrum	No	1	0.9989	0.0065	[21]
2002	n	β^-, F/GT	Recoil spectrum	Ion[1]	-0.1	-0.1054	0.0055	[22]
2005	^{38m}K	β^+, F	Recoil TOF[2]	MOT[3]	1	0.9981	0.0045	[23]
2008	^{21}Na	β^+, F/GT	Recoil TOF	MOT	0.553	0.5502	0.0060	[24]
2011	^{6}He	β^-, GT	Recoil TOF	Ion[4]	$-\frac{1}{3}$	-0.3335	0.011	[25]
2013	^{8}Li	β^-, GT	$\alpha - \alpha$ energy	Ion[5]	$-\frac{1}{3}$	-0.3307	0.0090	[26]

1.5.1 1963 Oak Ridge experiment with ^{6}He

In the early 1960s, Johnson *et al* [16] made a determination of $a_{\beta\nu}$ for the pure Gamow-Teller decay of ^{6}He, and to this day remains the most stringent bound of tensor currents coming from angular correlation measurements[6]. They produced their ^{6}He using neutrons from the Oak Ridge Research Reactor on 150 g of beryllium oxide powder via the $^9\mathrm{Be}(n,\alpha)^6\mathrm{He}$ reaction. The ^{6}He atoms are then swept via water vapor to a conical decay volume, with the water vapor having been removed along the way by a series of cold traps. The ^{6}Li ions produced by the decays are collimated through a 1/2 in aperture at the end of the conical volume, where they are analyzed by magnetic and electrostatic deflectors and finally detected by an electron multiplier to read the ion energy (see Figure 1.3 left). The shape of the ion energy spectrum (see Figure 1.3 right) is then used to infer $a_{\beta\nu}$, yielding a 0.9% determination, and a value of $a_{\beta\nu} = -0.3343 \pm 0.0030$. After more than 30 years, this result was corrected by Glück [17] to account for radiative corrections, yielding a modified result of $a_{\beta\nu} = -0.3308 \pm 0.0030$.

The majority of the uncertainty in this measurement comes from "Random variations in the spectra", amounting to 0.5%, and is said to arise from unknown and unaccounted for systematic variations in the experiment along with statistical uncertainties. Because this experiment measured the energy spectrum, it was also sensitive to uncertainties particularly at the endpoint. Figure 1.3 (right) shows the high sensitivity of a to uncertainties in the recoil energy at the endpoint. This uncertainty

---

[1] quasi-Penning trap

[2] Time-of-flight

[3] Magneto-optical trap

[4] Spherical Paul trap

[5] Linear Paul trap

[6] Soon to be published results from an experiment studying angular correlations in the decay of ^{8}Li will have similar or slightly more stringent limits [27].

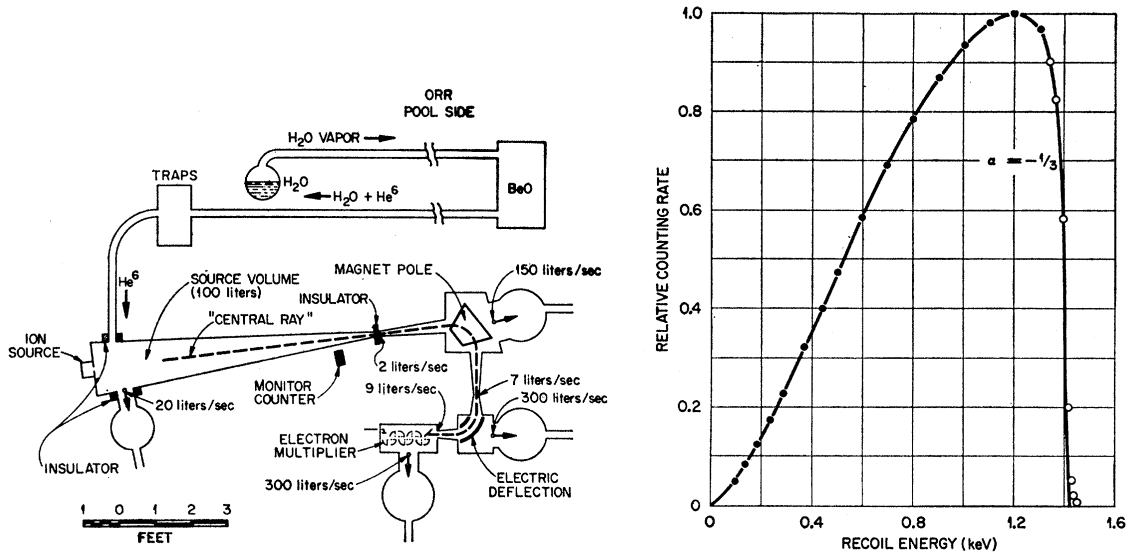

Figure 1.3: (left panel) Apparatus used in the 1963 Johnson *et al* ^{6}He decay measurement. (right panel) Results of the Johnson *et al* recoil ion energy spectrum measurement (points) showing consistency with the Standard Model axial vector current (curve). Figures taken from Ref. [16].

amounted to 0.4%. While this result is remarkable and still sets the bar for a precise determination of a, modern experimental techniques and improved computational power for Monte Carlo simulations of the experimental system and particle tracking provide motivation for improving upon this experiment.

1.5.2 2005 TRINAT experiment with laser-trapped ^{38m}K

In 2005 the TRIUMF[7] neutral atom trap (TRINAT) collaboration published their limits on scalar interactions in the pure Fermi decay of magneto-optically trapped ^{38m}K [23]. The ISAC[8] facility at TRIUMF in Vancouver, Canada, which provides

[7]TRI University Meson Facility

[8]Isotope Separator and Accelerator

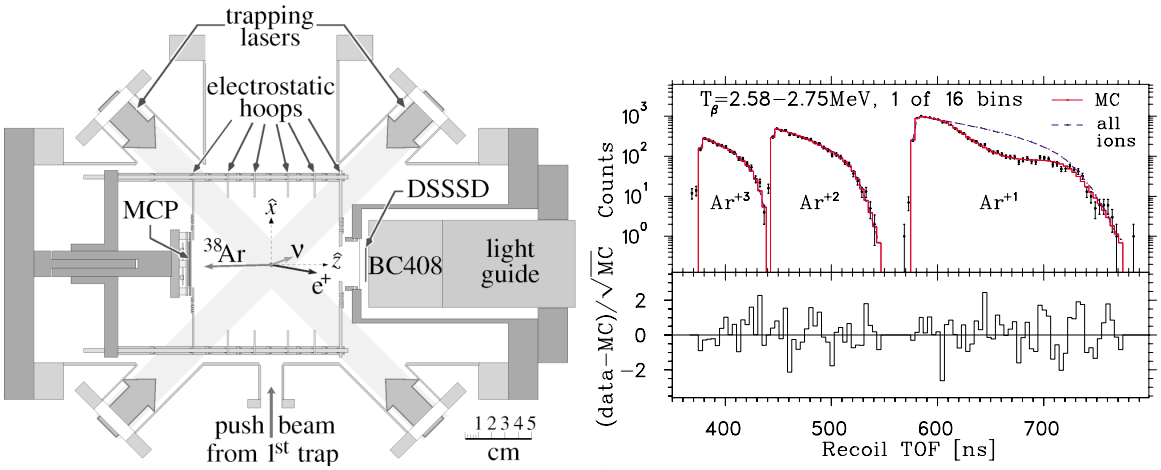

Figure 1.4: (left panel) Neutral atom trap apparatus used in the 2005 Gorelov *et al* ^{38m}K decay measurement. (right panel) Results of the recoil time-of-flight spectrum measurement fitted to curves generated by Monte Carlo simulations for three different charge states along with residuals. Acronyms: MCP means microchannel plate, DSSSD means double-sided silicon strip detector, and MC mean Monte Carlo generated data. Figures reproduced from Ref. [23].

^{38m}K and ground state ^{38}K atoms through spallation and fragmentation reactions from a 500 MeV proton beam. Due to the isotopically and isomerically-selective nature of laser-trapping, the ^{38m}K atoms could be selectively transported via a two-stage magneto-optical trap (MOT) to the final detection chamber, well-separated from the untrapped ground state ^{38}K atoms which mostly stick to the walls and decay in the preceding stages. By measuring the time-of-flight (TOF) of the recoiling ^{38}Ar ions in coincidence with the β^+ and fitting the results to Monte Carlo generated TOF spectra, the angular correlation could be determined. This experiment represents the first successful determination of a using an atom trap, yielding $a_{\beta\nu} = 0.9981 \pm 0.0030_{\text{stat}}\ ^{+0.0032}_{-0.0037}\ _{\text{syst}}$, consistent with the Standard Model prediction of $a_{\beta\nu} = 1$ for this $0^+ \rightarrow 0^+$ decay.

In this experiment, the β^+ is detected using a combination of a double-sided silicon

strip detector (DSSD) and a scintillator/PMT. The recoil ion is focused and guided using an electric field provided by six electrostatic hoops whereupon it is detected using a position-sensitive microchannel plate (MCP) (see Figure 1.4). The cold, well-localized source that a MOT provides is used along with the TOF and MCP position to reconstruct the recoil ion momentum. The DSSD provides a measurement of the β^+ direction. This is sufficient in this over-determined system to extract the relative angle of the β^+ and ν.

Because this experiment relies on comparison with Monte Carlo simulations, it is critical that systematic effects associated with the uncertainties in the MOT cloud size, shape, and position are studied carefully. These effects, along with uncertainties in the electric field uniformity are the leading systematic limitations in the quoted result. This experiment provides inspiration for the present experiment and validation of neutral atom trapping as a viable method for angular correlation measurements, and there are plans to further upgrade this experiment for a 0.1% determination of $a_{\beta\nu}$ for Fermi decays [28].

1.5.3 2006 Fléchard *et al* experiment using ion-trapped $^6He^+$

In 2011 the LPCTrap[9] collaboration published analysis results from a 2006 experiment searching for tensor currents using ^{6}He [25]. The LIRAT[10] beamline at the GANIL-SPIRAL[11] coupled cyclotron facility in Caen, France provides ^{6}He by bombarding a graphite target with a 75 MeV/nucleon beam of ^{13}C, where the atoms are ionized using an ECR[12] ion source. After an RF-cooling and bunching stage, the $^6He^+$ ions are injected into a Paul trap. Similarly to the TRINAT group, the researchers

[9]Laboratoire de Physique Corpusculaire de CAEN

[10]Ligne d'Ions Radioactifs A Très basse énergie – Low Energy Radioactive Beamline

[11]Grand Accélérateur National d'Ions Lourds – System for Producing Online Accelerated Radioactive Ions

[12]Electron Cyclotron Resonance

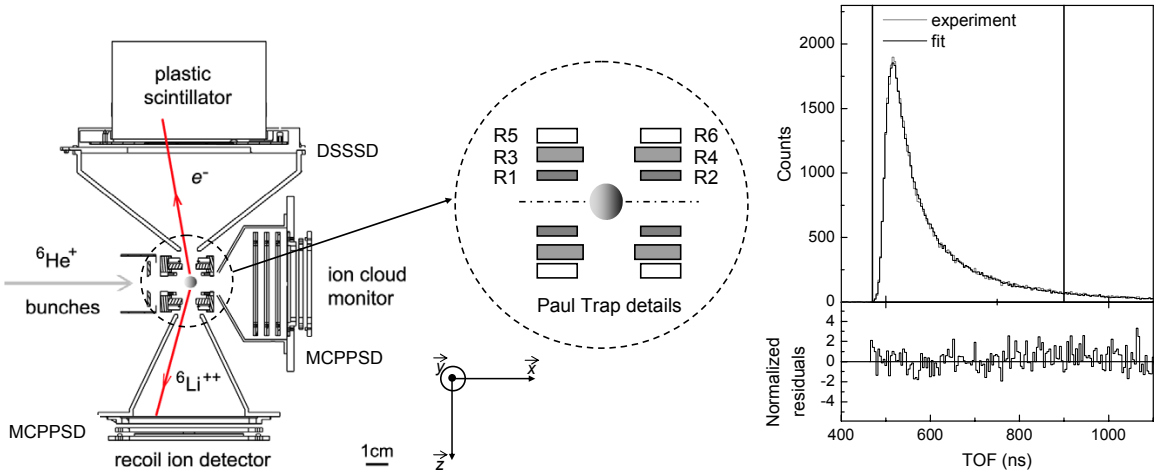

Figure 1.5: (left panel) Ion trap apparatus used in the 2006 Fléchard *et al* ^{6}He decay measurement. (right panel) Results of the recoil time-of-flight spectrum measurement fitted to curves generated by Monte Carlo simulations along with residuals.

determined the angular correlation coefficient by fitting the time-of-flight distribution of the recoiling $^6Li^{++}$ ions in coincidence with the β detected by a DSSD and plastic scintillator to spectra generated by Monte Carlo simulations. Using this method, the group reported a measured value of $a_{\beta\nu} = -0.3335 \pm 0.0073_{\text{stat}} \pm 0.0075_{\text{syst}}$. While not as precise than the 1963 Oak Ridge experiment, this result is the most precise determination of $a_{\beta\nu}$ in pure Gamow-Teller decays using coincidence measurements.

An ion trap is an attractive choice for trapping, as it generally can be used with a variety of isotopes. However, ion traps are much hotter and less well-localized than MOTs are. Also as opposed to MOTs, the ions interact via the Coulomb interaction, leading to space charge effects. The spatial extent and temperature of the ion cloud must be carefully understood to reduce systematic errors in such measurements. The cloud temperature presents the largest systematic uncertainty in this experiment and combined with the statistics during this run, the precision of this determination was at the 2% level, however more recent and higher statistics data are currently under

analysis [29]. Using a MOT would reduce systematic uncertainties associated with trap size and temperature.

1.6 Limits in the LHC era

In accordance with Equations 1.6 and 1.7, we typically express bounds on tensor and scalar couplings in terms of $C_T + C'_T$ and $C_T - C'_T$ which couple entirely to left-handed and right-handed neutrinos, respectively. Figure 1.6 shows an analysis performed in Ref. [30] which expresses these limits as a fraction of C_A for selected nuclear beta decays. For left-handed neutrinos, nuclear beta decay limits are not competitive with the limits set by radiative pion decays. However, more stringent bounds are present when including data from neutron decay, which has a strong Gamow-Teller character even though it isn't a pure Gamow-Teller decay.

While radiative pion decay dominates the limits for left-handed neutrinos, limits on right-handed neutrinos are dominated by two experiments: the Johnson *et al* [16] as discussed in Section 1.5.1, and the relative longitudinal polarization of positrons emitted from pure Fermi and pure Gamow-Teller decays, $P_{\mathrm{F}}/P_{\mathrm{GT}}$ in ^{14}O and ^{10}C, respectively [31].

Collider experiments at the CERN[13] LHC[14] can also probe the weak interaction for tensor and scalar contributions. However, the signals from these experiments depend on whether or not the new particles involved in these exotic interactions are kinematically accessible at the collider energies, *i.e*, whether the new particles are too heavy to be produced on-shell. If one assumes that the new interactions remain point-like at the TeV scale, then model-independent statements can be made using effective field theories. Under this assumption, direct probes using $pp \to e\nu + X$ channels can be analyzed by looking for an excess of events at high transverse mass

[13]Conseil Européen pour la Recherche Nucléaire/European Organization for Nuclear Research

[14]Large Hadron Collider

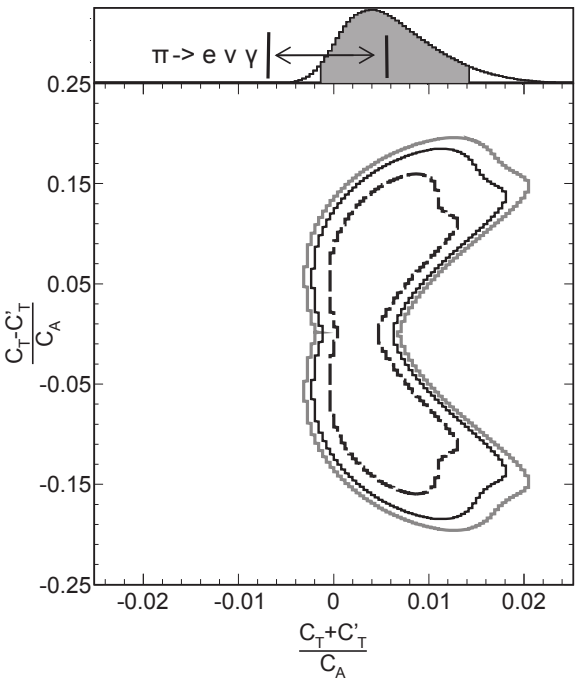

Figure 1.6: Limits on C_T and C'_T from neutron and nuclear beta decays. The contour plots show the 68%, 90%, and 95% confidence intervals. At the top is a comparison of these limits overlaid with limits from radiative pion decay for left-handed neutrinos. Figure reproduced from Ref. [30].

defined as

$$m_T \equiv \sqrt{2E_T^e E_T^\nu (1 - \cos \Delta\phi_{e\nu})} \tag{1.16}$$

where E_T^e is the transverse momentum of the electron/positron, E_T^ν is is the missing transverse momentum of the neutrino, and $\Delta\phi_{e\nu}$ is the angle between the leptons, where transverse is defined to be perpendicular to the direction of the axis of the collider beam. Events due to Standard Model processes fall away at high m_T relative to exotic tensor and scalar interactions, so setting a large transverse mass threshold $\overline{m}_T$ allows for a removal of Standard Model backgrounds (see Figure 1.7). A recent analysis published by the CMS collaboration places bounds on new couplings. Shown

Experiment	Reference	$\lvert\epsilon_T\rvert$,$\lvert\tilde{\epsilon}_T\rvert$
LHC-7	CMS [33]	2.9×10^{-3}
LHC-8	Projection	2.2×10^{-3}

Table 1.4: CMS analysis of LHC bounds (first row) and projected bounds (second row) on $|\epsilon_T|$ and $|\tilde{\epsilon}_T|$ at the 90% confidence level.

in Figure 1.8 is the CMS data used in the analysis. For a given number of expected background (Standard Model) events compared with the number of actually observed events, the limits in Table 1.4 were achieved. These values are given in terms of the parameters used in Reference [32], and are related to C_T and C'_T in the following way:

$$\left|\frac{C_T + C'_T}{C_A}\right| = \left|8\frac{g_T}{g_A}\epsilon_T\right| \tag{1.17}$$

$$\left|\frac{C_T - C'_T}{C_A}\right| = \left|8\frac{g_T}{g_A}\tilde{\epsilon}_T\right| \tag{1.18}$$

where $|g_T| \approx 1$ and $|g_A| \approx 1.26$.

Assuming the new physics does indeed occur above the TeV energy scale, the limits from existing LHC data on tensor couplings are on the 10^{-3} order, which poses a large challenge for competition coming from low-energy beta decay experiments involving angular correlations. However, beta decay experiments do not make any assumptions about the new physics being above a particular energy scale, and therefore have the advantage of being entirely model-independent even if the limits obtained from such experiments are not as stringent if the high-energy assumption is permitted. Therefore these two approaches should be seen as complementary with each other. Figure 1.9 overlays the present limits shown in Figure 1.6 with the limits achieved by the LHC [32] and the limits achieved by Johnson *et al* which constrain the $C_T - C'_T$ space, as well as indicating the hypothetical limits which we expect to obtain by making a 0.1% measurement of $a_{\beta\nu}$ assuming no deviation from the Standard Model.

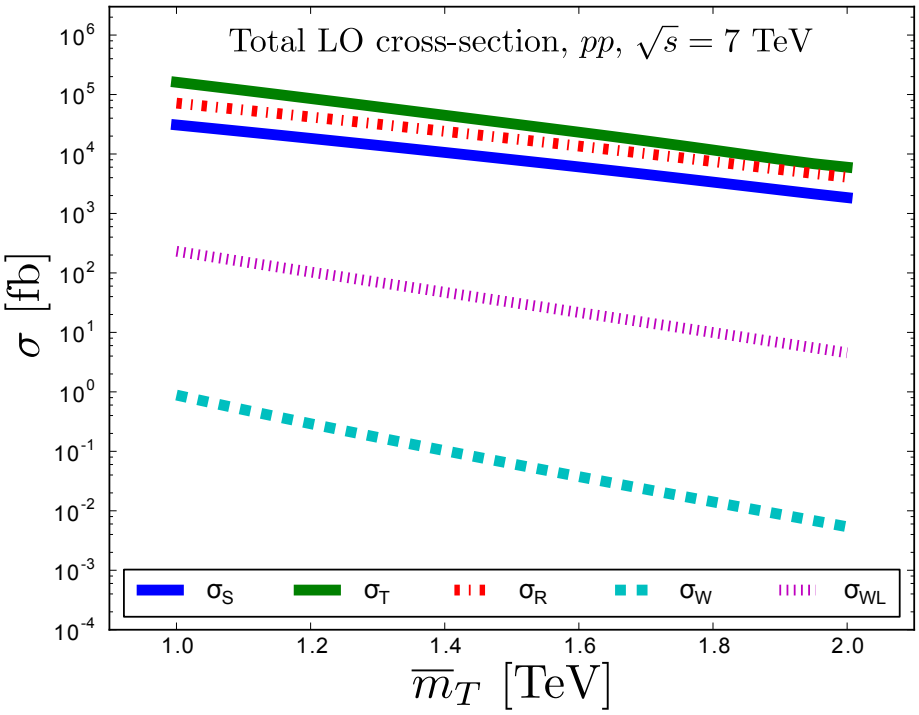

Figure 1.7: Cross-sections as a function of the transverse mass threshold $\overline{m}_T$ as defined in the formalism of Ref [32] for $\sqrt{s} = 7$ TeV. A comparison between σ_T and σ_W shows the relative cross-section enhancement for tensor (and scalar) couplings compared with standard model predictions (σ_W) at high $\overline{m}_T$. $\sigma_{\rm R}$, $\sigma_{\rm S}$, and $\sigma_{\rm WL}$ are described in Ref. [32], from which this figure was reproduced, and represent new physics outside the scope of this thesis.

1.7 The present experiment

The experiment we are preparing to perform has many similarities to some of the past experiments described in Section 1.5. In particular, the as-mentioned TRINAT group at TRIUMF has used a double-magneto optical trap (MOT) setup for studying scalar interactions in the beta decay of ^{38m}K [23]. The attractive qualities of a MOT, which can provide a cold, pure, backing-free source of radioactivity has led us to also use

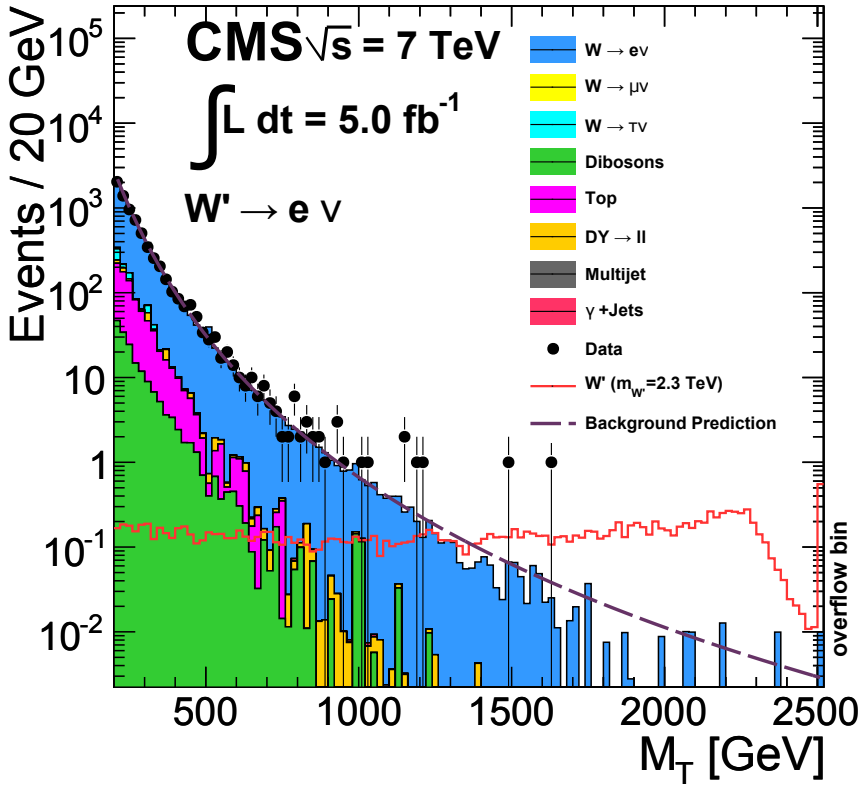

Figure 1.8: CMS data from $pp \to e\nu + X$ channels. The red line indicates the predicted events as a function of the tranverse mass distribution due to electron decays from a new heavy gauge boson W'. No significant excess of events above the standard model expectation (background prediction) was found. Figure reproduced from Ref. [33].

a double-MOT setup. Each MOT chamber is optimized for different characteristics. Focusing on the second chamber, we find the beta telescope back-to-back with the recoil ion detector. The beta telescope consists of a multiwire proportional chamber (MWPC) acting as the ΔE detector as well as measuring the beta's position, and a plastic scintillator to measure the total energy of the beta. The recoil ions are accelerated towards a position sensitive microchannel plate (MCP) ion detector by a uniform electric field generated by an array of stainless steel electrodes (see Section 5.4

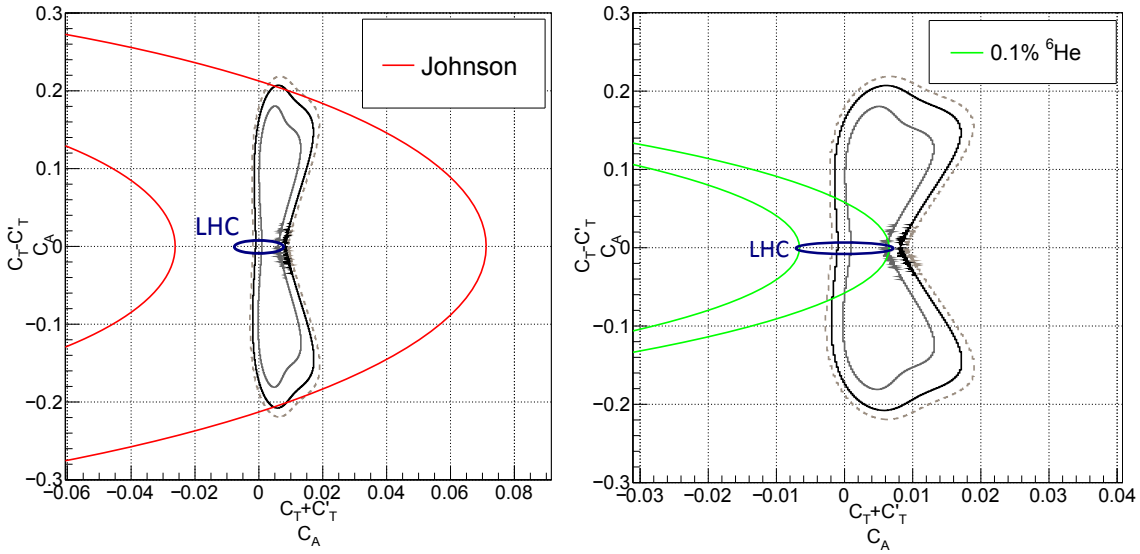

Figure 1.9: (left panel) Limits on C_T and C'_T from nuclear beta decay overlayed with LHC data and the Johnson *et al* limits. (right panel) LHC limits overlayed with with our proposed 0.1% limits on $a_{\beta\nu}$ using ^{6}He.

for a detailed description).

As we are interested in the angular-correlation of the beta and antineutrino, it is useful to understand what we are required to measure. To get a complete picture of the kinematics of this decay, we would need to know nine parameters, three for each component of momentum of three different particles. However, momentum conservation reduces this number to six, as any three components can be kinematically deduced if the others are known. Energy conservation restricts an additional parameter, leaving five free parameters which must be measured if one is interested in the relative angle of the particles upon emission. In our experiment, we measure six parameters, and therefore our system is over-determined.

The beta telescope defines the initial beta direction as well as starting the time of flight clock. The MCP defines the recoil ion final position and stops the time of flight clock, which when combined is sufficient to determine the recoil ion's initial momen-

tum. This experiment is therefore well-suited to measuring the angular correlation of the beta and the antineutrino and the search for tensor-type interactions.

1.8 ^{6}He as a candidate nucleus

The choice of ^{6}He as the nucleus of choice is made easy as it is the only case of a pure Gamow-Teller decay [34] and is thus uniquely sensitive to tensor couplings. The atomic and nuclear structures of ^{6}He are simple and calculable which allows for easier comparison with theory and are not expected to contribute to uncertainties at our proposed level of precision. The half-life of ^{6}He of approximately 800 ms [35] allows sufficient time to cool, trap, and manipulate the atoms before decay. The beta endpoint energy of 3.508 MeV and low mass of the daughter ^{6}Li ion (see decay scheme in Fig. 1.10) causes the recoil energy to be relatively high at 1.405 keV, which allows for easier detection.

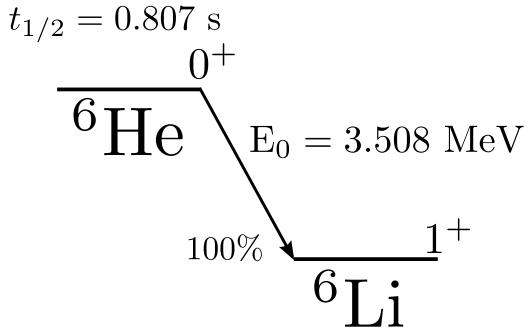

Figure 1.10: Decay scheme of ^{6}He.

Using helium in a neutral atom trap is not without its challenges, however. It is a noble gas, and the excitation energy from the ground state to the next excited state is approximately 20 eV. This is not an accessible transition energy for laser cooling and trapping and requires alternative methods of excitation such as an RF discharge which we implement to excite many atomic levels, some of which relax into an excited

metastable state. This process is very inefficient, leaving only 1 in 10^5 atoms in the metastable state under optimal conditions. It is for this reason that we require such high production in order to gather sufficient statistics.

Chapter 2

Production of ^{6}He

Performing a measurement of the $\beta - \bar{\nu}$ angular correlation requires large coincidence rates to gather sufficient statistics to lower experimental uncertainties. Toward this end, we have designed and constructed a molten lithium target to produce a high-intensity source of ^{6}He for weak interaction studies using the ^{7}Li(d,^{3}He)^{6}He reaction. Deuteron energies up to 18 MeV and intensities exceeding 15 μA are made possible using a HVEC[1] model FN tandem Van de Graaff accelerator located in house at the Center for Experimental Nuclear Physics and Astrophysics (CENPA) of the University of Washington. The following chapter describes the design of the lithium target and measurements demonstrating an extracted ^{6}He rate of more than 2×10^{10} atoms/s to a low-background experimental area.

2.1 Some methods to produce ^{6}He

As discussed in sections 1.5.1 and 1.5.3, ^{6}He has a history as a nucleus of interest for a determination of the angular correlation parameter $a_{\beta\nu}$ in pure Gamow-Teller decays. Since it is a light nucleus, it has served as a useful tool in understanding nuclear structure through comparisons with *ab initio* calculations, and has been useful to

[1] High Voltage Engineering Corporation

this end through nuclear charge radius measurements [36] as well as interaction cross-section measurements which revealed the neutron halo structure through comparison with a theoretical relativistic mean field model [37]. Recent proposals in neutrino physics seek to use ^{6}He as a source of collimated antineutrinos to measure flavor oscillations [38]. It is therefore worth considering some of the ways in which to produce ^{6}He, and to compare these methods with our own.

2.1.1 Neutron capture

The Oak Ridge experiment (see Section 1.5.1) used the $^9\mathrm{Be}(n,\alpha)^6\mathrm{He}$ reaction. Figure 2.1 shows the cross section for this reaction, which is as high as 100 mbarn. Neutrons provided by the Oak Ridge reactor reacted with very fine BeO powder [39], producing an estimated 7.2×10^{11} atoms/s from a neutron flux of 2×10^{13} n/cm^2-s. Water vapor swept the ^{6}He to the spectrometer using a water boiler and a series of cold traps and condensers to remove the water vapor prior to entry into the decay volume. In this process, 1.4% of the initial yield, or about 9.9×10^{10} ^{6}He atoms/s were delivered to the spectrometer.

A recent effort to produce a high-intensity source of ^{6}He was made at the ISOLDE[2] facility at CERN, which like the Oak Ridge source also uses the $^9\mathrm{Be}(n,\alpha)^6\mathrm{He}$ reaction via neutrons on BeO powder. A pulsed beam of 1.4 GeV protons delivered from the Proton Synchrotron (PS) accelerator is used to create spallation neutrons by impinging on the ISOLDE neutron converter, which produces neutrons in a wide energy range of $0.1 - 1400$ MeV. Of these neutrons, only those within the $1 - 15$ MeV energy window contribute to the final reaction. The BeO target is heated to 1400 °C to enhance the ^{6}He extraction efficiency, and at this temperature 82% of the ^{6}He is extracted from the target [41]. In each pulse of protons, approximately 1.5×10^{10} ^{6}He atoms are produced in the target.

---

[2]Isotope mass Separator On-Line

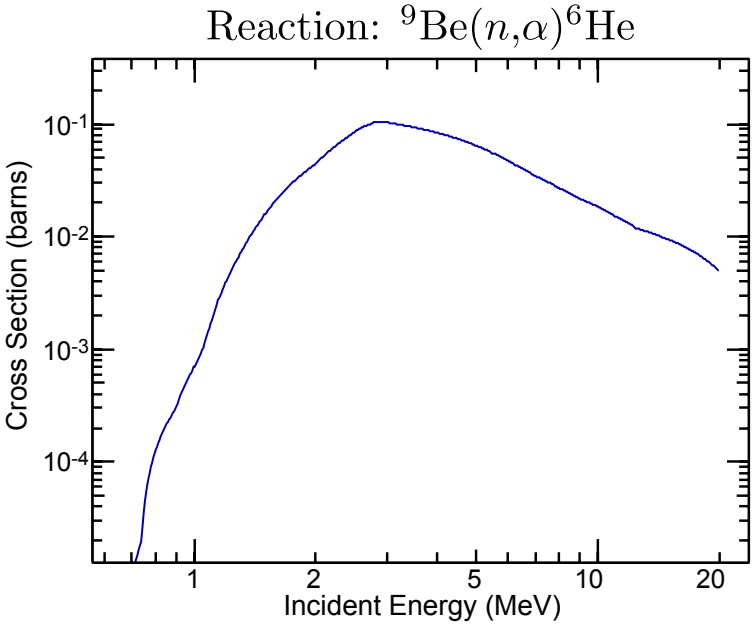

Figure 2.1: Nuclear cross section for the ^{9}Be$(n,\alpha)^{6}$He reaction taken from [40].

2.1.2 Beam Fragmentation

The LPCTrap experiment discussed in section 1.5.3 produces $^{6}He^{+}$ ions using a primary ^{13}C beam at 75 MeV/A to bombard a graphite target which is coupled to an ECR ion source [25]. The ion beam is then mass separated using dipole magnets and delivered to the experimental area. This production method yields an overall $^{6}He^{+}$ production rate of 1.5×10^{8} ions/s.

2.1.3 Nucleon Transfer reaction

We have chosen to use the ^{7}Li(d,^{3}He)^{6}He, making use of the facilities at the University of Washington where we have a tandem Van de Graaff accelerator capable of > 15 μA deuteron beam currents. When bombarded with deuterons, ^{7}Li undergoes a nucleon transfer reaction whereby the deuteron strips off a proton, becoming ^{3}He, and leaving behind ^{6}He. The cross section for this reaction is shown in Figure 2.2. It peaks at

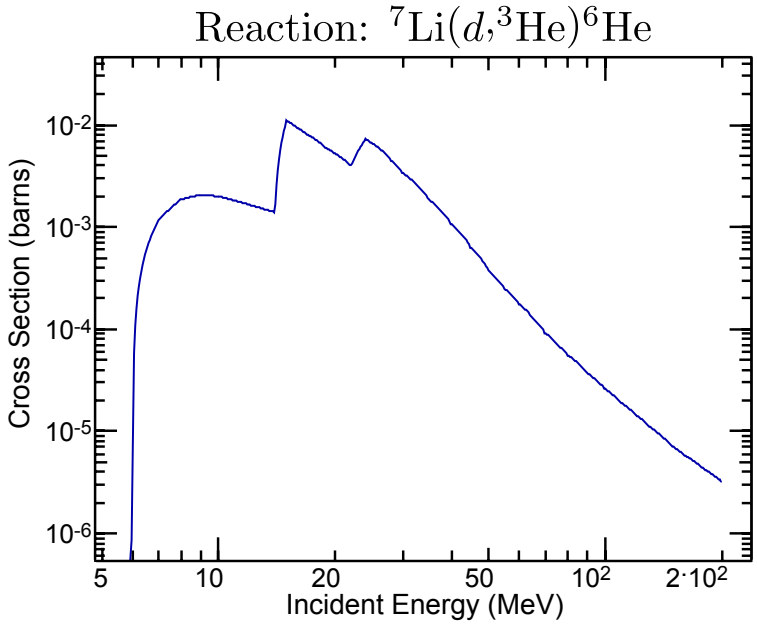

Figure 2.2: Theoretical nuclear cross section for the ^{7}Li(d,^{3}He)^{6}He reaction taken from [40].

$\sim$10 mbarn for 18 MeV incident beam energy, which is well matched to our accelerator. With our deuteron intensity we can produce a large amount of ^{6}He, as the rest of this chapter will detail. Lithium also has few radioactive reaction products when struck with deuterons. Due to the selective nature of this nucleon transfer reaction, only tritium, ^{3}He, and ^{8}Li are made. We can therefore produce a clean source of ^{6}He using this method.

2.2 Lithium properties and handling

Lithium is a soft, silver-white alkali metal which does not occur freely in its elemental form in nature due to its high chemical reactivity. Its single valence electron is readily given up to form ionic bonds with more electronegative elements. When exposed to moist air, lithium very quickly reacts with water vapor and nitrogen to form dark, thin layers of lithium nitride, and eventually a chalky white color to form solid lithium

hydroxide. When dropped directly into water, lithium reacts rapidly, and though it is not nearly as violent a reaction as other alkali metals such as potassium or cesium the reaction can produce flames. The reaction with water strips off a hydroxide group, forming an aqueous solution of LiOH and releasing hydrogen gas. Because lithium is about half the density of water ($0.534\ \frac{g}{cm^3}$), it floats on the surface of all liquids except for liquid hydrogen and helium.

Because of these properties, elemental lithium must be stored out of contact with the many materials with which it reacts. We store it in mineral oil when not in use. Even here, care must be taken to ensure that most of the lithium is submerged in the mineral oil, since it will float to the top and could be exposed to air if the container is not sufficiently sealed. We purchase our lithium from Alpha Aesar [42] as 12.7 mm (0.5 inch) diameter rods in a mylar bag filled with mineral oil. When handling lithium, we use a glove box under positive pressure with argon gas. Argon is a noble gas which does not react chemically with lithium, and it is heavier than oxygen and nitrogen, so it tends to displace air. At the top of the glove box is an exhaust port through which any overpressure can escape. This helps to flush out the air which would otherwise be trapped inside the glove box and could contaminate the lithium. We also use a reservoir bag which serves to store additional argon gas while the glove box is being used. The glove box is designed for use under positive pressure and retracting the gloves can lower the pressure inside the box below atmosphere. This would cause air to leak into the glove box and spoil the quality of the argon atmosphere. The reservoir bag expands or contracts during use and provides a relatively constant air pressure inside the glove box, diminishing or eliminating any air from leaking inside.

Surrounding the base perimeter of the interior of the glove box is a copper tube with regularly spaced holes which allows the argon to uniformly fill the box and displace the more buoyant air (see Figure 2.3). There is an additional flexible line which can be used to manually direct the flow of argon into places where air may become trapped, such as in the transport container. To be sure that the atmosphere

is low in oxygen, we use an oxygen meter to determine when the lithium is safe to handle. Once we have determined that there is no oxygen in the glove box, we remove a rod of lithium stored under mineral oil. To prevent contaminating the freshly cut lithium surface, we use shears to cut a small, 10 mm long pellet while still under an extra container of mineral oil. To remove the excess mineral oil from the lithium, we immerse the pellet into a bath of hexanes, which acts as a solvent for the mineral oil, but quickly evaporates from the surface of the lithium.

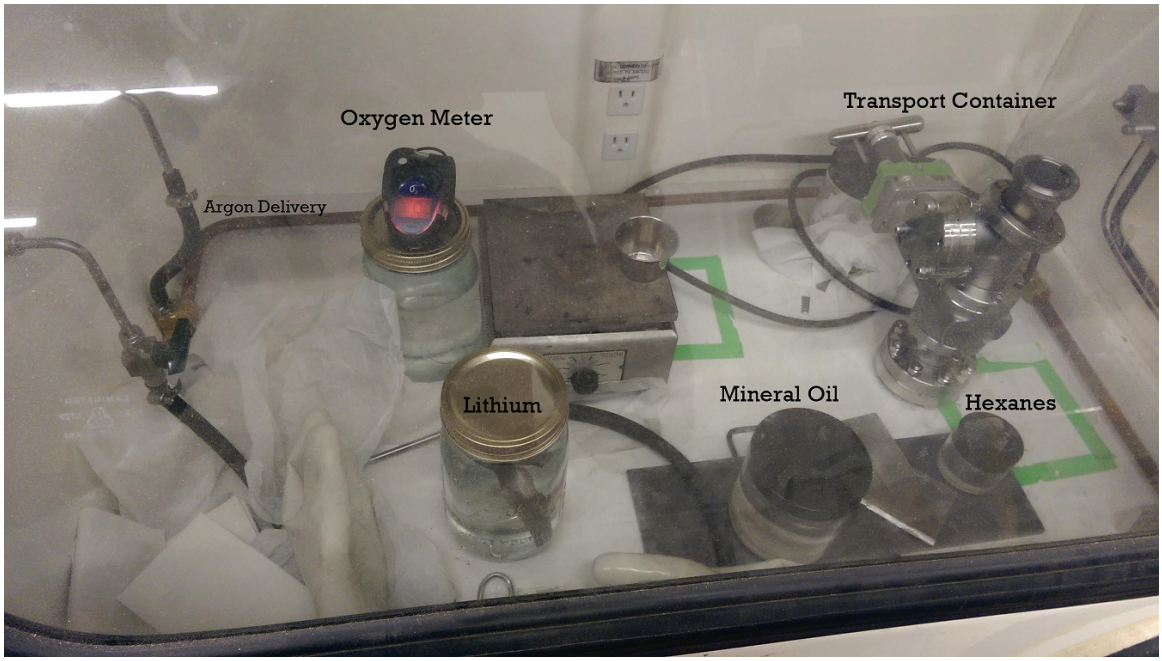

Figure 2.3: An inside view of the glove box. Shown here is the oxygen meter, the lithium container filled with mineral oil, and additional containers of mineral oil and hexanes.

The cleaned pellet of lithium is then dropped into a transport container, also flushed with argon and which is sealed on the top with a gate valve. On the bottom of the transport container is a viewport through which we can verify that the lithium looks clean and free of corrosion (see Figure 2.4). The transport container is then

connected to the final target chamber via conflat flanges and the gate valve is opened to let the lithium fall into the target cup which has either been evacuated or also filled with an argon atmosphere.

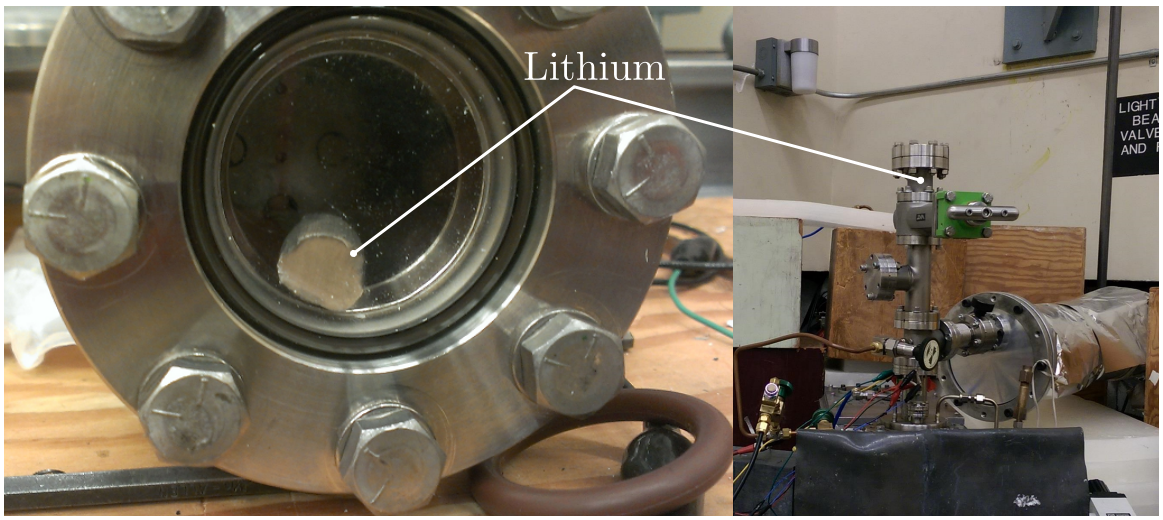

Figure 2.4: (left) A lithium pellet after being cut, cleaned, and sealed as seen through the viewport of the transport container, still silvery and shiny on the freshly cut surface, indicating that it has not been contaminated by exposure to air. (right) The transport container is connected to the target vacuum. Opening the gate valve (green) will drop the lithium into the pre-heated target.

2.3 Target development

When designing a suitable target for ^{6}He production, some basic considerations needed to be addressed. First, the bombardment of lithium using deuterons produces substantial neutron radiation, so we need to deliver the ^{6}He to a low-background environment outside the target room. We therefore must separate the beamline vacuum from the target vacuum where the atoms are produced to maximize the delivery rate. This

can be done either by separating the lithium from the beamline via a foil, or by using a collimating aperture in combination with differential pumping. Secondly, the ^{6}He diffusion rate through the bulk lithium metal must be maximized to ensure a high extraction efficiency. This can be achieved by displacing the level of the lithium metal such that the deuteron beam strikes the lithium just beneath its surface. Finally, we need to have a large conductance between the experimental areas to minimize losses due to decay during transport.

The process of developing our target station went through several iterations, but the core principle has remained the same. High-energy deuterons pass through a thin foil, originally a 51 μm stainless steel foil (see Section 2.9), separating the target vacuum from the beam line vacuum, whereupon they undergo a nuclear reaction with ^{7}Li housed within an opening 14 mm in diameter and 35 mm in height inside a stainless steel cup. In this process, the beam loses about 1.3 MeV in the foil, and penetrates less than half a centimeter into the lithium. The cup is heated to an operating temperature of 250 °C by means of a 300 W resistive heater attached to a copper block mounted to the back of the target. This is above the 180 °C melting point of lithium, so the metal is in liquid form when the nuclear reaction occurs. The ^{6}He extraction efficiency is improved by a factor of $\sim$20 when using liquid lithium instead of solid lithium as originally measured by a scintillator/photomultiplier tube which was displaced from the target and shielded with lead bricks (see Figure 2.6). In front of the stainless steel foil we mount an electrically isolated 9 mm diameter graphite collimator and read the beam current on that collimator in order to assess the alignment and focus of the beam. The lithium cup is electrically isolated from the vacuum housing by means of a ceramic break and can be biased to +300 V in order to serve as a Faraday cup and monitor the deuteron beam current. High-vacuum electrical feedthroughs were used to provide heating power, measure the target temperature via a platinum resistance temperature detector (RTD) or later via thermocouples, and measure the beam current on the target and the collimator. Stainless steel was chosen for the foil

and target cup principally because it is one of the few metals that does not react chemically with lithium. It is also sufficiently strong to withstand one atmosphere without failure, even at these small thicknesses. Using stainless steel as a foil is not without issues, and recent developments will be discussed in Section 2.9.

2.4 Low intensity target

Our earliest tests were run at low beam intensities of approximately 10 nA at 12 MeV. At these intensities and energies, the beam power deposited into the target is approximately 0.12 W, a very small amount which is easily conducted away without significantly raising the temperature of the system. For this reason no cooling mechanism was required. Although the resistive heater is in principle electrically isolated from the rest of the system, we nevertheless observed a small 50 nA leakage current flowing to the lithium cup whenever the heater was active. Since this is larger than the beam currents we were using at this time, we would first heat the target before disconnecting the heater during data taking cycles. The result of this was an approximately 30 °C temperature variation throughout these low current runs. This effect becomes negligible when running at higher beam currents.

We initially observed very little production when running in the configuration shown in Figure 2.6. Lead shielding ensured that the count rate measured by the thin plastic scintillator would be restricted to some background rate plus events that occurred within the 35 mm diameter, 381 mm long tube mounted at the top of the target assembly. However, mounting the scintillator at the very top of the system registered a count rate ten times higher, which could not be accounted for simply by solid angle considerations or shielding. This indicated that the helium was not efficiently diffusing out of the lithium bulk. At this time, our methods of handling lithium resulted in lithium which was partially corroded with oxide and nitride layers, which formed a crust upon the surface of the lithium. To solve this problem we

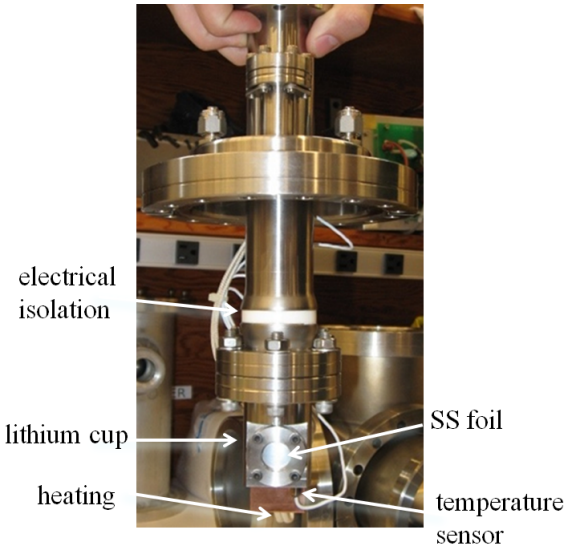

Figure 2.5: Initial target used at low-intensity.

installed a combined rotary and linear motion feedthrough onto the top of the target assembly (See part 4 of Figure 2.8). This feedthrough was attached to a rod with a stainless steel, semi-cylindrical paddle which could be lowered into the lithium to simultaneously displace the lithium vertically for fine adjustment of the height of the liquid as well as to rotate through the lithium and break up and surface contaminants that may have formed during handling or loading into the target. The addition of this device has proved instrumental in extracting the ^{6}He with the highest efficiency and allowed agreement between our expected and measured rates when configured as in Figure 2.6.

2.5 Target with cooling

The next iteration of the target needed to be modified to accommodate the full beam current and energy which deposits 180 W or more into the cup (see Figure 2.7).

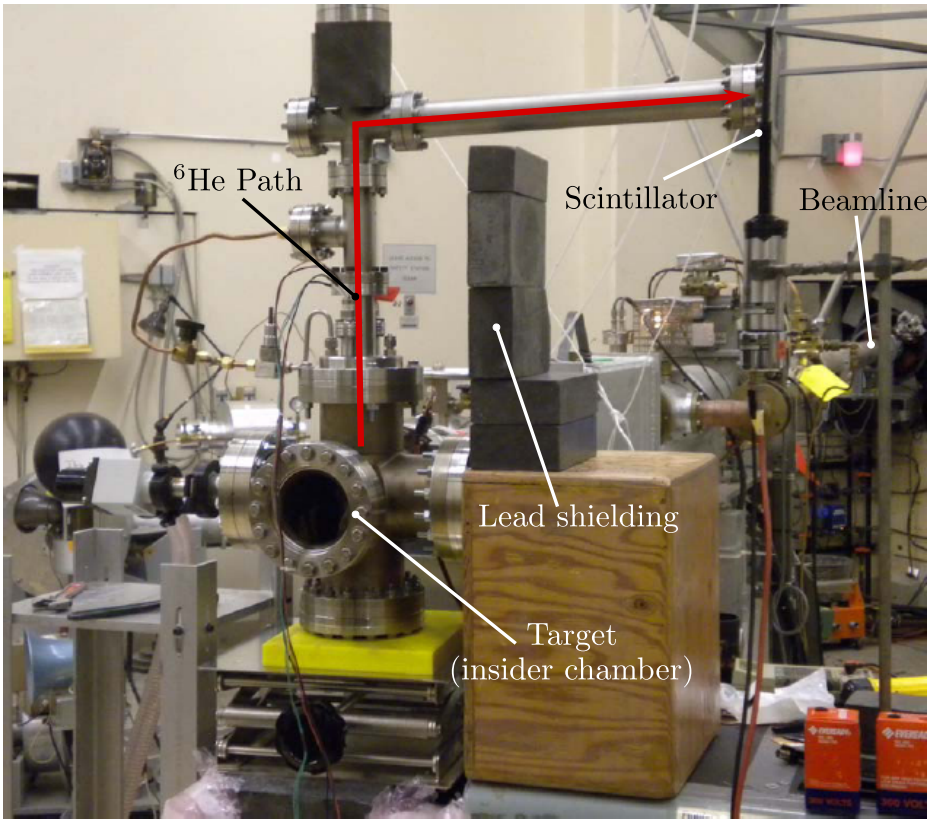

Figure 2.6: Initial target setup used for low-intensity production tests.

Since this beam power would otherwise heat the target up to $> 500\,^{\circ}\mathrm{C}$, well beyond the desired set point of around $250\,^{\circ}\mathrm{C}$, we modified the copper block housing the resistive heater to have a series of channels which allows compressed air or other gases to flow through and actively cool the target (see Figure 2.9 for the latest version of this copper block). We are able to heat the target from room temperature to $250\,^{\circ}\mathrm{C}$ within $\sim$10 minutes. At this temperature, we measured a radiative cooling power of approximately 95 W. Flowing compressed air through the copper block at a constant rate, we adjusted the power to the resistive heater via a Variac until an equilibrium temperature was reached. Accounting for the radiative cooling at the equilibrium temperature, we found the active cooling power from the compressed air

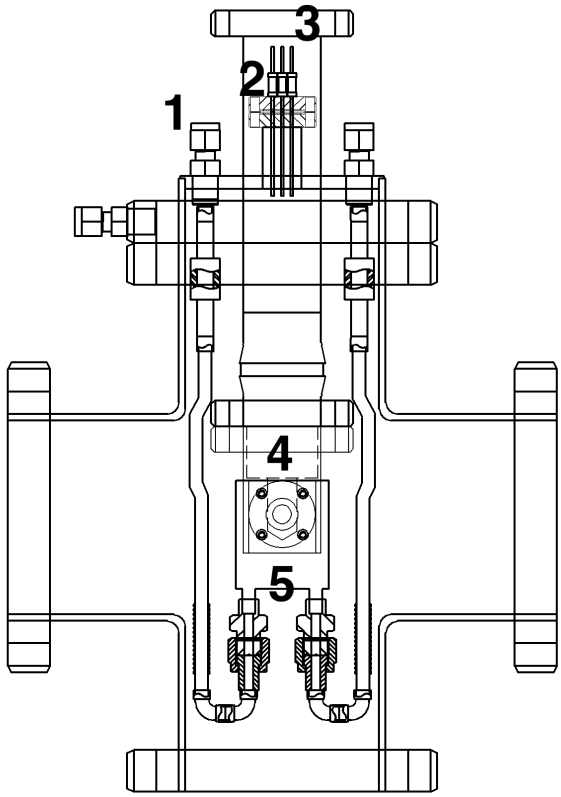

Figure 2.7: Upgraded lithium target station viewed along the direction of the deuteron beam. 1) Electrically isolated cooling lines. 2) Electrical feedthroughs for temperature sensor, beam current monitoring and powering the resistive heater. 3) Target vacuum volume for the extraction of ^{6}He. 4) Electrically isolated lithium target cup with collimator. 5) Cooling and heating copper block attached to the lithium target.

to be approximately 145 W. This can be made to be even larger by increasing the flow rate, though this is typically unnecessary, since the combined active and radiative cooling power at our operating temperature is equal to about 240 W, which is more than the deuteron beam typically can deposit.

Thermal contact between the copper block and the stainless steel lithium cup had been achieved in the first two iterations by bolting the copper block onto the

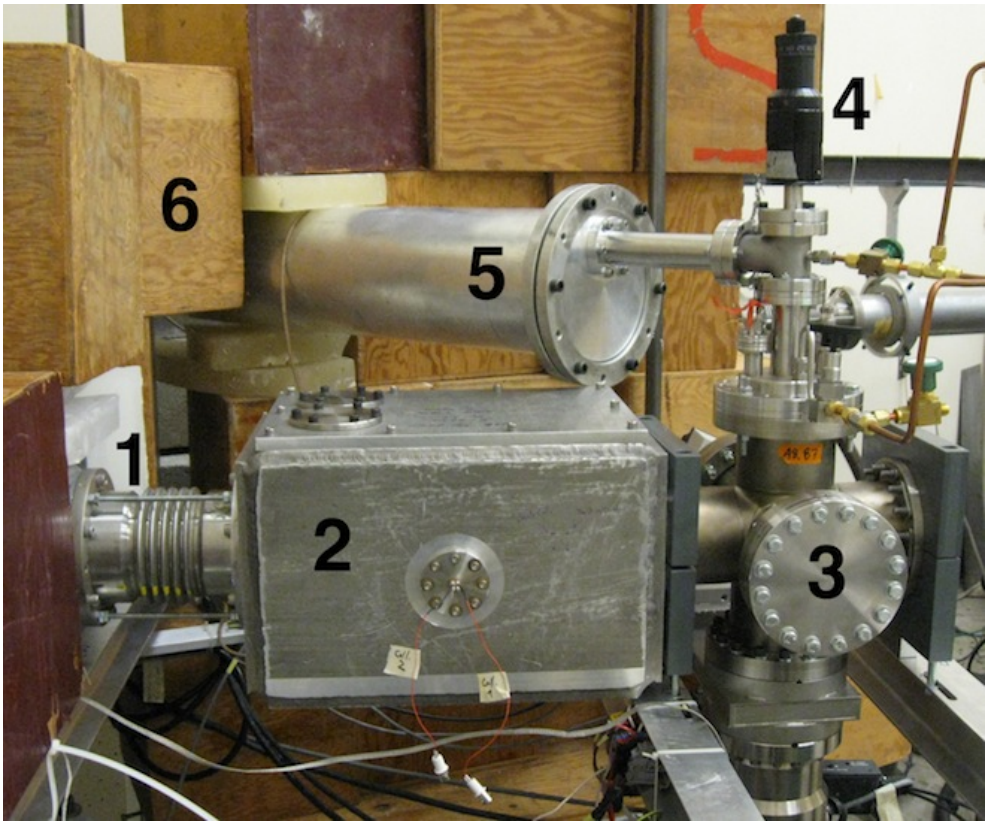

Figure 2.8: Setup of the lithium target on the beamline. 1) Vacuum housing of incoming deuteron beam. 2) Beam collimation. 3) Lithium target. 4) Mechanical manipulation of molten lithium. 5) Extraction tube to low background experimental area. 6) Neutron shielding.

cup to make direct contact. While this worked well initially, the copper block would eventually be thermally decoupled from the cup after several heating and cooling cycles and our ability to cool the cup would therefore be compromised. To remedy this problem, our next iteration of target cups were permanently bonded to the copper block via high-temperature silver soldering.

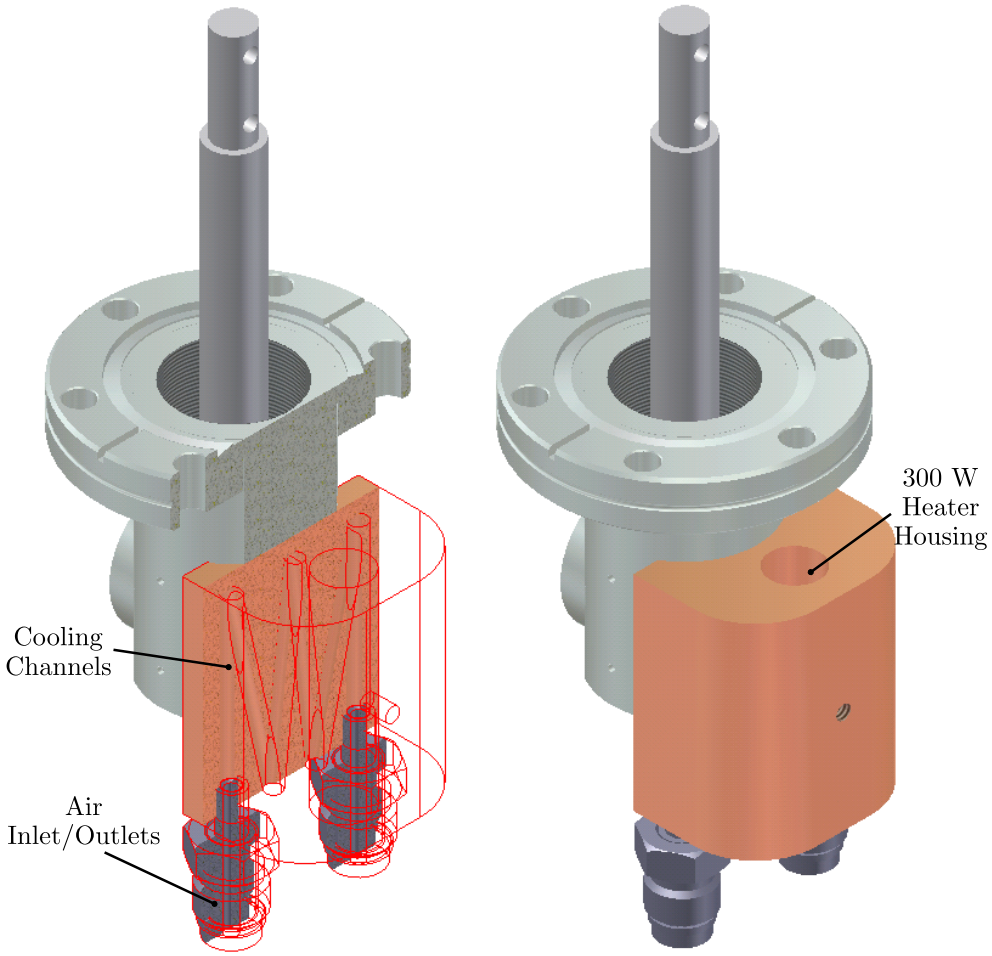

Figure 2.9: On the left is a cutaway of the copper block used to heat and cool the target cup. Cooling channels were cut into the copper block to allow compressed air to pass through. On the right is the copper block in total, which houses a 300 W resistive heater used to maintain the lithium at 250 °C while the beam is off.

2.6 The final target

The third iteration of the target was developed to remedy some vacuum problems introduced by the cooling air lines. These lines were made of copper and were silver

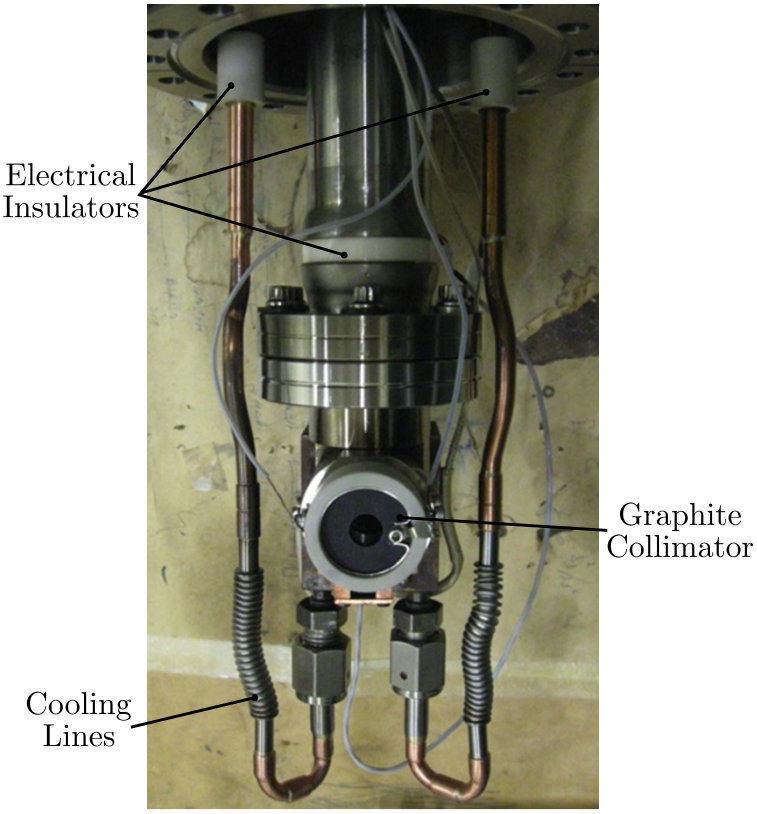

Figure 2.10: The second target incorporated cooling lines to allow compressed air to remove the heat deposited by the 180 W deuteron beam. These lines were kept electrically isolated from the rest of the system via ceramic insulators.

soldered to electrical isolators and flexible bellows (see Figure 2.10). At the time of the second target iteration, electrical insulation was important for accurately reading the amount of beam on target and thus this target design was used to collect the production results detailed in Section 2.8. However, the electrical insulators were made of ceramic and therefore presented a risk of breaking under torque loads generated, for example, during the attachment of the VCR fittings which connect the cooling lines to the copper block of the target. The cooling lines were fed through two Swagelok fittings welded to the outside of the target chamber which isolated the vacuum inside

the beam line from atmosphere. While these worked well for over a year, after many heating and cooling cycles one Swagelok fitting began to leak. Efforts to seal the leak with Torr-Seal and other leak sealants served as stop-gap measures, but ultimately the leak would return as the intense heat of the exhaust cooling air would cause cracks to reopen in the sealant (see Figure 2.11).

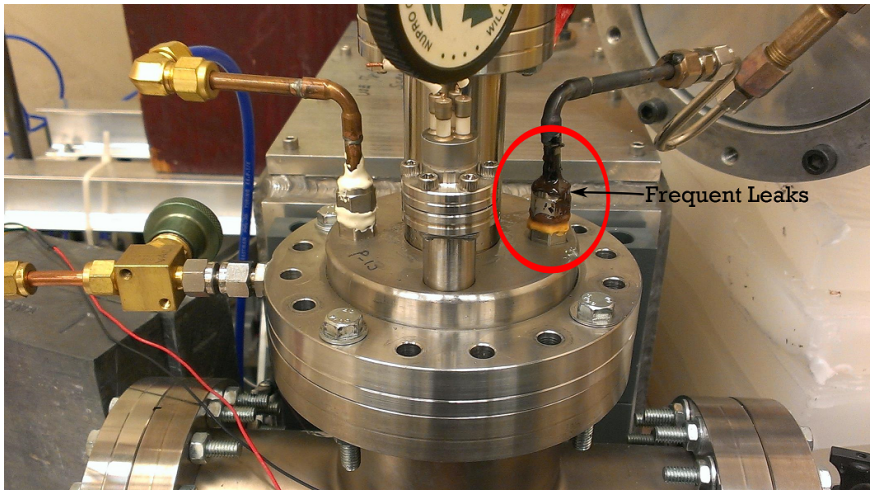

Figure 2.11: The Swagelok fittings used as feedthroughs for the cooling lines eventually began to leak after many temperature cycles. The fitting on the right is much darker than the one on the left because it is the exhaust line and thus is much hotter ($\sim 150 - 200\,^{\circ}\mathrm{C}$) than the cool ($\sim 15\,^{\circ}\mathrm{C}$) input line. Efforts to seal the leaks were temporary and eventually the system was replaced.

To remedy these issues and to make the system more robust for production, the third target replaced all copper lines with stainless steel and all ceramic insulators were removed (see Figure 2.12). The new stainless steel lines were welded instead of silver soldered where possible which further reduced the possibility that a line could get sufficiently hot to compromise a joint. The Swagelok connections were replaced with welds as well, further reducing the possibility of leaks. The ceramic insulators had served their purpose and were no longer needed, as we had become

solely interested in maximizing our ^{6}He production, and thus did not need to know precisely how much beam was on target. Isolated collimators were still in place and the current on them could be read to help center the beam on target.

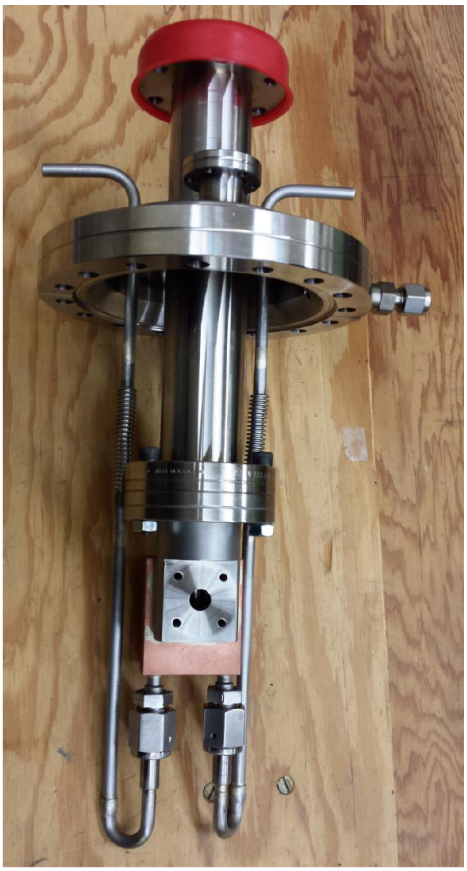

Figure 2.12: The latest target design eliminated areas of failure and is more suited to long-time, high-intensity use than previous iterations.

2.7 Shielding and background reduction

During production, copious amounts of neutrons and gamma rays are generated as a by-product of bombardment as well as activation of other materials such as the stain-

less steel foil. It is therefore impossible to make sensitive beta-decay measurements next to the target station while running large beam currents. Instead, the gaseous ^{6}He must diffuse out of the lithium and be transported to a low-background environment for experimentation. We achieve this via a 15 cm-diameter and 3 m-long tube (See part 5 of Figure 2.8) which passes through the shielded wall of the production room and into our experimental area (see Figure 2.13). At the end of the tube is a 360 l/s turbo-molecular pump which compresses the ^{6}He into its outlet (See Figure 2.14). The turbo-molecular pumping speed was chosen to match the calculated 300 l/s conductance of the 15 cm-diameter transport tube. We estimated that the time for the helium to travel through the tube based on conductance calculations as well as previously measured transit times through the turbo-molecular pump of $\sim$ 250 ms amounts to 2 s, which when combined with the ^{6}He decay time would result in a loss factor of about 5.6. Separating the target area from the experimental area is a $\sim$ 1.5 m thick concrete wall. However, the transport tube passes through a section of the wall which is made of stacked concrete bricks, which do not shield neutrons as effectively as the solid concrete. To minimize the neutron flux through this wall, as well as through a hole in the wall of the basement used as a cable tray, we stacked many wooden boxes filled with borated paraffin around the target, and especially in between the target and the wall of concrete bricks. The paraffin thermalizes and captures some of the neutrons, but to capture the remainder we also placed a 2.5 cm thick sheet of polyethylene loaded with 5% boron (by weight) (See Figure 2.14). The combination of these measures reduced the neutron flux in the experimental area down from 10 mSv/h to an acceptable 30 μSv/h at the highest beam currents.

2.8 Production results

We performed several measurements to determine the ^{6}He production rate using a ΔE-E plastic scintillator configuration triggering on a hardware-generated coincidence

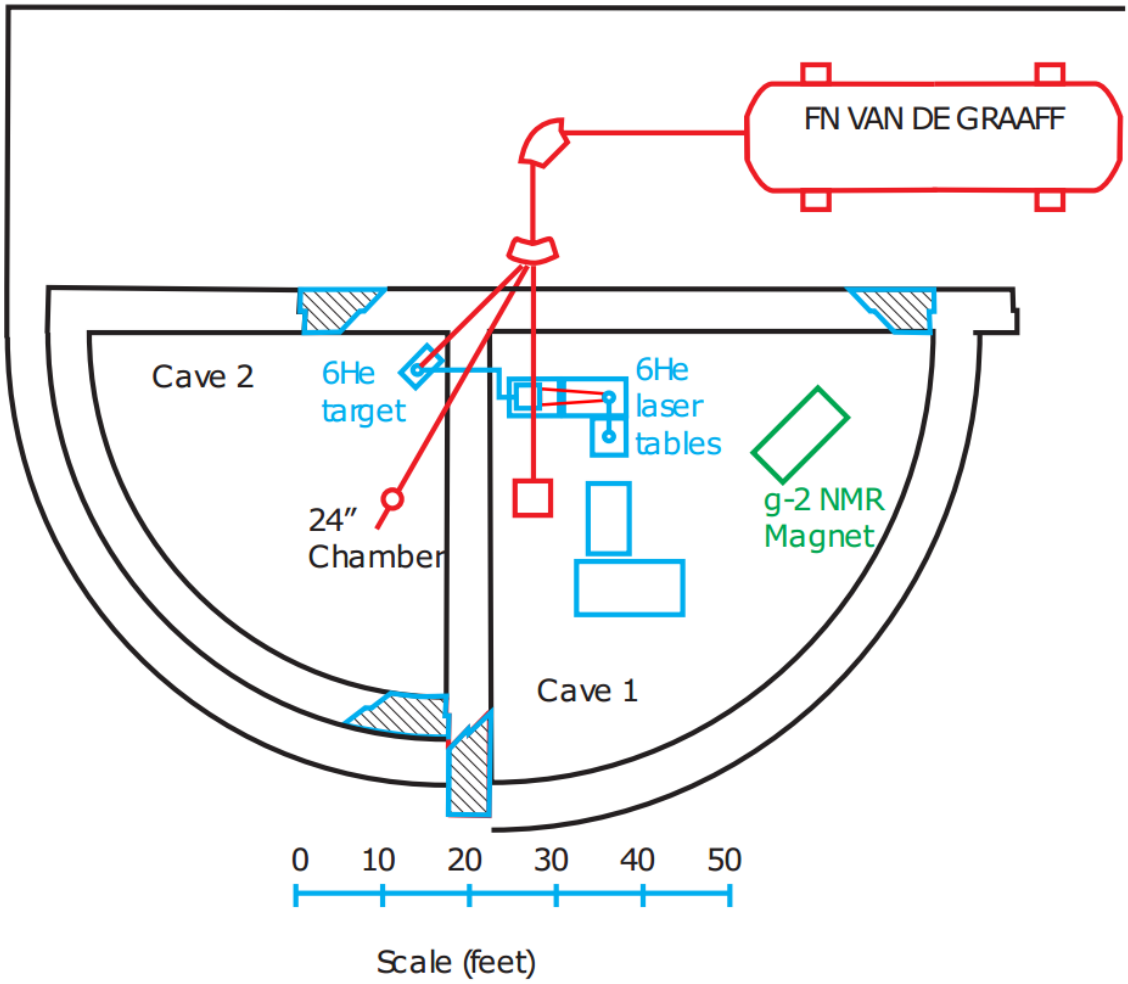

Figure 2.13: Schematic drawing of the layout of our experiment within the shielded CENPA experimental rooms.

signal between the two photomultiplier tubes. Typically a beta event would deposit about 300 keV into the ΔE scintillator. The signals from the photomultiplier tubes were shaped, amplified, and run through a peak-sensing CAMAC ADC[3] (model Ortec AD413A). The software package JAM [43] was used to communicate with the CAMAC

[3]Computer Automated Measurement And Control analog-to-digital converter

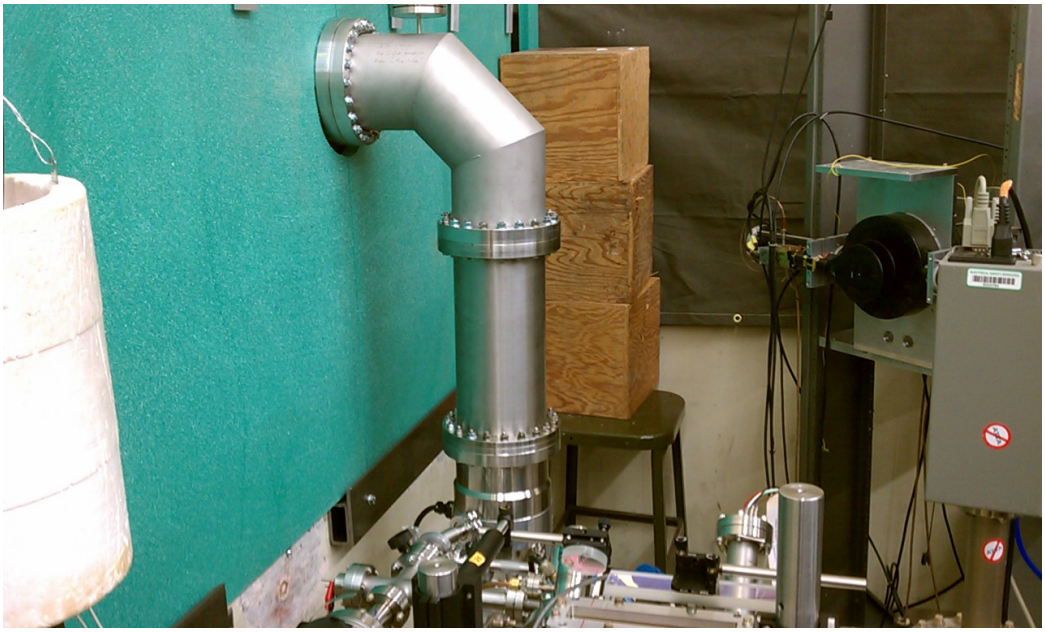

Figure 2.14: A 15 cm-diameter transport tube passes through a wall of stacked concrete bricks which are covered by a 2.5 cm thick sheet of polyethylene loaded with 5% boron (by weight) to absorb thermalized neutrons.

crate and also to provide time stamps for the data.

We measured the production rate using different configurations, but in each case a 35 mm diameter, 381 mm long tube was mounted in front of our ΔE-E plastic scintillators and was sealed at its end with a 254 μm thick copper foil which constituted an approximate energy loss of 300 keV. We would cycle the deuteron beam on and off, striking the target for 8 s, and then deflecting the beam at the low energy end of the accelerator to stop the beam and count events for an additional 8 s. For a given number N of observed decays, the known ^{6}He lifetime τ, the counting time T, detection efficiency of the betas ϵ, and the fraction of the measuring volume $V_{\rm meas}$ with respect to the total volume containing produced ^{6}He $V_{\rm tot}$, one can calculate the

^{6}He production rate R using the following equation:

$$R = \frac{N}{\epsilon\tau\left(1 - e^{-T/\tau}\right)^2}\frac{V_{\text{tot}}}{V_{\text{meas}}} \approx \frac{N}{\epsilon\tau}\frac{V_{\text{tot}}}{V_{\text{meas}}} \tag{2.1}$$

The necessity of the volume ratio is due to the fact that we estimated the beta detection efficiency ϵ taking into account only the geometry of the measuring volume. Using the simulation code Penelope [44], the detection efficiency was calculated to be 0.12% for our typical detector arrangement. This number is small because few events are emitted within the detector's solid angle except for those which are nearest to the copper sealing foil. We compared these simulation results with measurements using a point-like ^{90}Sr source at various distances from the detector and found that our measurements agreed with our simulation to within an uncertainty of 10%.

For our first measurements we mounted our scintillators and decay volume along with lead shielding in a configuration similar to that shown in Figure 2.6, where the single thin scintillator is replaced with our ΔE-E detector assembly (see Figure 2.15). A 5 cm thick stack of lead shielding prevents most beam-related background events from reaching the detector, as well as ensuring that the activity measured is coming from the measuring volume instead of any ^{6}He still trapped in the bulk lithium. To further protect the detectors from beam-related neutron or gamma ray damage, we ran with relatively low beam currents. For this configuration the ratio $V_{\text{tot}}/V_{\text{meas}}$ was 2.3 which accounts for the geometry of the lithium cup and chimney before the measuring tube. We made several measurements each at various beam energies, and averaged the results using the rate equation given by Equation 2.1 for each energy. The beam current provided by the accelerator is not always constant, so each rate was appropriately scaled to a beam current of 10 nA, which was our standard current for production comparisons. After each change in beam energy, we would manually stir the lithium and, if necessary, change the level of the stirring paddle to optimize production. Due to the difficulties in precisely reproducing beam tuning conditions and ^{6}He production, we assign a 50% uncertainty to our reported values. The rate as

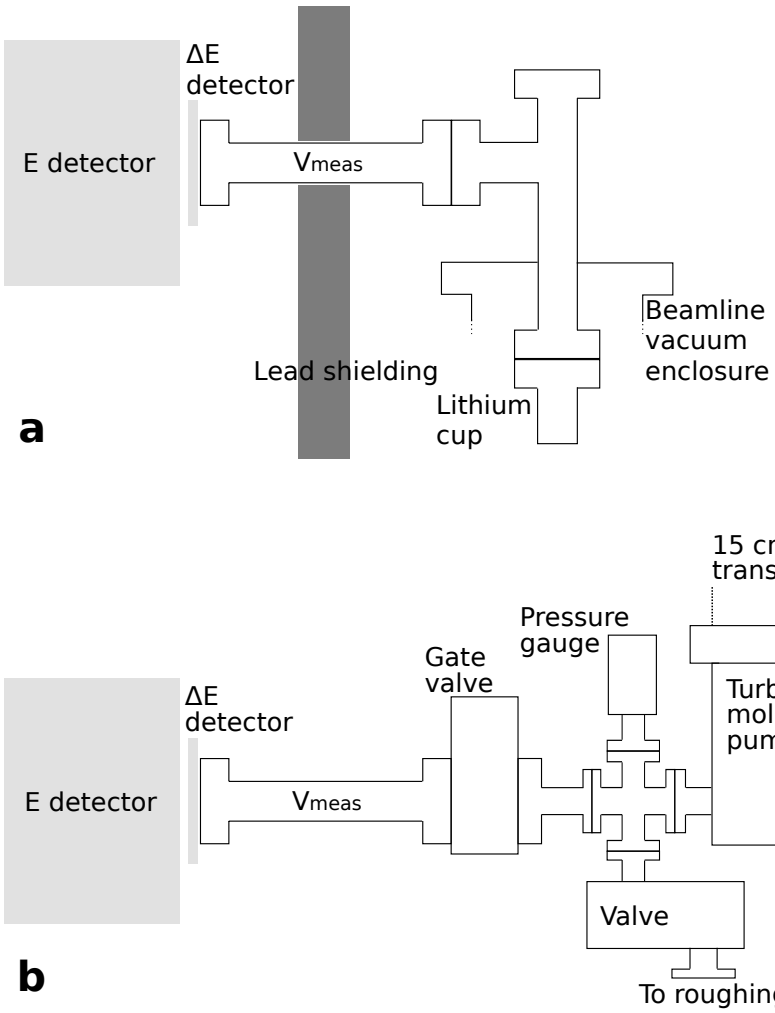

Figure 2.15: Setup of our ΔE-E detector for the ^{6}He rate measurements. Panel (a) shows the schematic of the installation close to the source (see Fig. 2.6 for a picture) while panel (b) shows the setup in the low-background experimental area. Dimensions are not to scale.

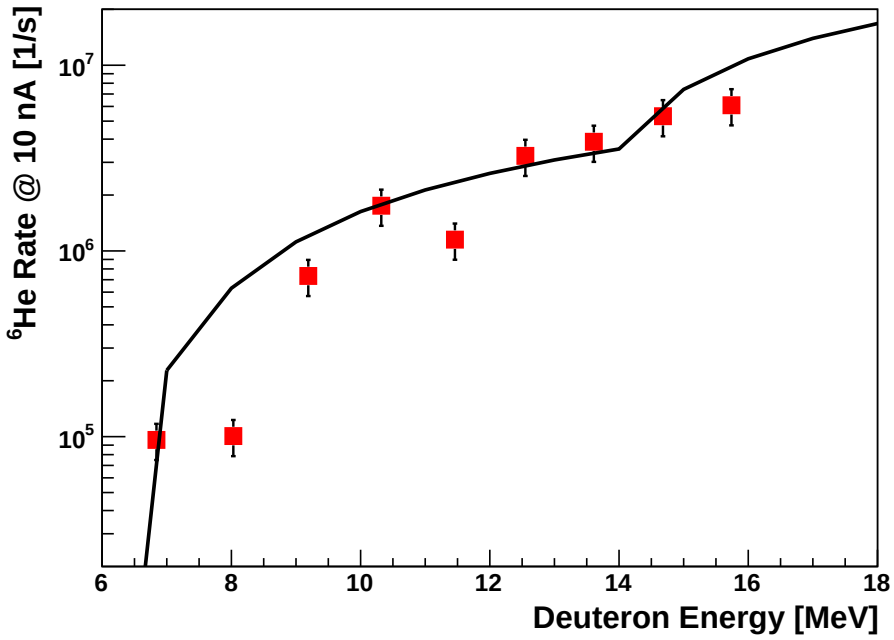

Figure 2.16: Extracted ^{6}He rates next to the lithium target station as a function of incident deuteron beam energy. The energy of the beam has been corrected for the calculated energy loss in the 51 μm thick stainless steel foil using SRIM [45]. The solid line depicts the predicted yields for ^{7}Li(d,^{3}He)^{6}He based on Ref. [40] scaled up by a factor of 3.

a function of beam energy is given in Figure 2.16 after accounting for the 1.3 MeV energy loss due to the 51 μm foil as calculated by the software package SRIM[4] [45].

Directly comparing our results with existing cross-section data for the ^{7}Li(d,^{3}He)^{6}He reaction is made difficult due to the small number of previous experimental measurements. Only two measurements are known to us: one was an inverse kinematics measurement using a lithium beam energy of 81 MeV [46], and the other was performed at a deuteron energy of 22 MeV [47], above what we can presently test. For the measurement performed at 22 MeV, a differential cross-section for ^{6}He was partially given in Figure 9 of the same paper. Integrating over this differential cross-section

[4]Stopping and Range of Ions in Matter

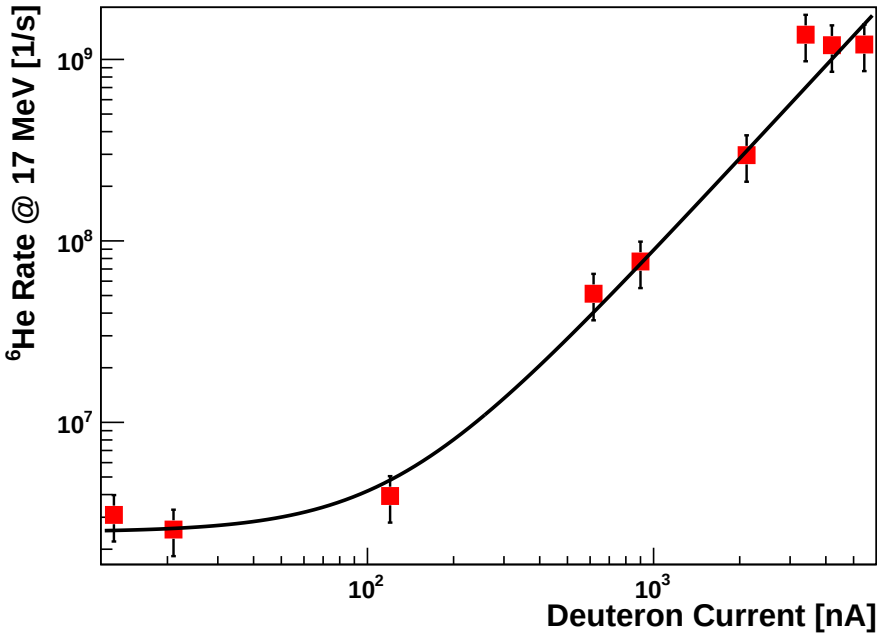

Figure 2.17: Extracted ^{6}He rate in the low-background experimental area as a function of deuteron beam current at an energy of 17 MeV. The data are fit with an empirical model: $R \approx 2.5 \times 10^6 + 656 \times I^{1.7}$ where the rate R is in decays/s and the current I in nA. The exponential factor of 1.7 hints at a somewhat improved extraction of ^{6}He at higher beam currents.

yields a total cross-section of ∼12 mb. The cross-section for this reaction has also been calculated in [40], although the calculations at 22 MeV yield 4 mb instead of 12 mb. For this reason, we overlay onto Figure 2.16 the calculated cross-section values reported by [40] scaled up by a factor of 3. The results show reasonable agreement indicating that the helium is diffusing out of the bulk lithium without much if any loss.

The second set of measurements recorded the rate of ^{6}He production as a function of incident deuteron beam intensity. Again, due to the large amount of radiation produced at high intensities, we used the ΔE-E detector configuration shown in Fig-

ure 2.15b. Because the turbo-molecular pump would otherwise constantly compress the helium found in the 15 cm transport tube into the measuring volume, we installed a pneumatically-actuated gate-valve at the entrance to our measuring volume which would close at the end of the 8 s beam cycle. We performed background measurements to determine whether our detectors saw activity originating from ^{6}He compressed at the back of the pneumatic gate-valve by running beam while the gate-valve was closed, but we saw no significant activity. For this reason lead shielding was not used here as it was used for the first set of measurements. In this configuration the ratio $V_{\mathrm{tot}}/V_{\mathrm{meas}}$ was 1.7, taking into account only the additional volume occupied by the vacuum hardware located after the exhaust of the turbo-molecular pump as we assumed the helium would entirely be compressed into this region. After again calculating the production rate according to Eq. 2.1 with a 50% uncertainty to account for changes in lithium and beam tuning as before, we report our results as a function of deuteron beam intensity in Figure 2.17. The data were then fit with an empirical model yielding the resulting fit function of $R(^6\mathrm{He/s}) \approx 2.5 \times 10^6 + 656 \times I(\mathrm{nA})^{1.7}$. That the fit is not entirely linear with intensity indicates better extraction efficiencies at higher beam currents. We speculate that this is due to the high-intensity beam locally heating the lithium at the site of production thereby increasing the diffusion rate and allowing for the helium to more easily escape the bulk. After the data shown in Figure 2.17 were taken, our engineers were able to extend the capabilities of the accelerator to provide beam currents of 15 μA. Subsequent tests at these beam currents show good linearity when compared with production rates at beam currents above the 1 μA level which suggests that above these currents the extraction efficiency is maximized. At currents of 15 μA and deuteron energies of $\sim$18 MeV, we routinely see production rates as high as $\sim 2 \times 10^{10}$/s, as measured in the low-background environment. We tried to determine whether the bulk lithium temperature due to the resistive heater changed the production rates. Between 200 °C and 350 °C, no obvious effect was seen. However, below the melting point of lithium at 180.5 °C, the production rates

fell precipitously.

We compared decay rates at the same beam current and energy between the two configurations shown in Figures 2.15a and 2.15b to determine the measured loss factor due to the transport time in the 15 cm tube and turbo-molecular pump. Comparing the results in Figures 2.16 and 2.17 at 10 nA and 17 MeV, we find production rates of 6.2×10^6 and 2.5×10^6 atoms/s, respectively. We therefore conclude the loss factor due to transport to be 2.5 ± 1.8, which is somewhat better than our expected loss factor from conductance calculations.

2.9 Foil development

Our production measurements were performed using 51 μm stainless steel foils to separate the beam line vacuum from the lithium inside the target. For low-intensity, short-length runs such as the ones performed in Section 2.8, these foils worked well. Stainless steel at this thickness is strong enough to withstand many pressure cycles of several atmospheres without obvious deformation, and the material does not react chemically with lithium at our operating temperatures of between 200 °C and 350 °C. However, stainless steel is a poor thermal conductor with a thermal conductivity (16-24 W/m·K) an order of magnitude lower than copper, and a melting point of around 1450 °C. The spot size of our beam on target is not precisely known as our beam profiler is located just upstream of a quadrupole magnet used for focusing and steering the beam on the target, but it is likely to be approximately 1 mm in diameter. A 1 mm diameter disk of stainless steel at a temperature of 1450 °C (emissivity = 0.9) would remove by blackbody radiation alone a power of order 1 W. This is insufficient to remove the nearly 20 W deposited into the foil by the 15 μA, 18 MeV deuteron beam. The lithium serves as a cooling bath to keep the stainless steel from immediately melting, but after only a few hours of constant beam the lithium begins to evaporate due to the intense heating, reducing or eliminating its capacity to cool the foil and

eventually leads to a foil rupture and loss of production. Figure 2.18 shows two stages of damage as the beam locally melts the stainless steel and eventually ruptures the foil, ending any appreciable production.

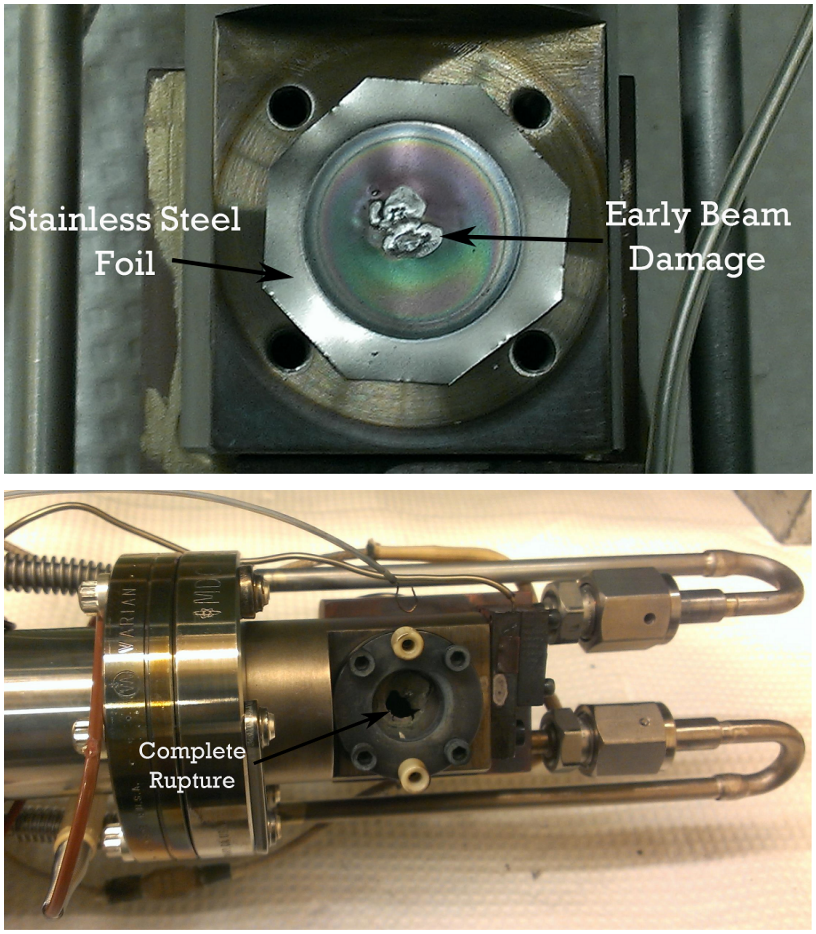

Figure 2.18: (top panel) Early signs of beam-related damage to the stainless steel foil can be seen. The pattern is made as the beam is drawn across the surface of the foil during tuning. (bottom panel) Complete foil rupture after 8 hours of integrated high-intensity beam time, requiring replacement.

To remedy this problem we looked at a number of alternative foils to serve as a replacement for stainless steel. One attempt was to use a copper foil electroplated

with chromium to prevent a reaction with lithium on copper. This attempt failed as the lithium migrated into the foil through the thin chromium coating and reacted with the copper, quickly compromising the integrity of the foil within a matter of 8 hours. Eventually we tried tantalum with success. Tantalum is one of a few metals or alloys which does not react with lithium at temperatures below 1000 °C [48]. It also has a melting point of 3020 °C (emissivity = 0.3 at this temperature), more than twice that of stainless steel. Its strength allows us to use foils as thin as 8 μm, reducing the deposited beam energy from 20 W to 3.75 W, including the higher stopping power due to the larger Z of tantalum as calculated by SRIM [45]. Assuming again a 1 mm diameter beam size and only blackbody radiation, the foil could radiate away between 1.75-2.5 W depending on the level of oxidation. This is still not quite sufficient to remove all of the deposited heat by radiation alone, but this is much better than stainless steel.

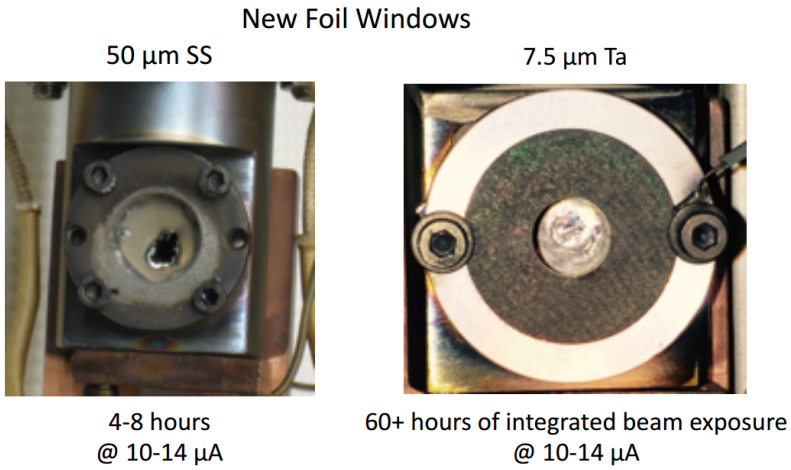

Figure 2.19: On the left, a stainless steel foil ruptured after several hours of beam. On the right, only minor signs of wear are seen on the new tantalum foil after several days of continuous beam exposure.

2.10 Remote Stirring System

Maintaining good contact with the bulk lithium is critically important for heat management, even with the improved properties of tantalum. While the metal can withstand much higher temperatures than stainless steel, the lithium behind it will still begin to evaporate if temperatures become too high. Without this cooling effect, even tantalum is at risk of beam damage. To this end we have developed and installed an auto-stirring device which actuates via remote control the stirring rod used to control the internal level of the lithium. Two motor drives, controlled by a LabVIEW VI [49] in our control room, serve as rotary and linear actuators (see Figure 2.20), allowing us to position the stirring paddle wherever we would like to maximize production. The VI also enables an automatic stirring sequence whereby the stirring paddle is lowered completely into the lithium and rotated for several revolutions to re-coat the tantalum foil. Typical cycling periods are 15 minutes.

Using the combination of the auto-stirrer and the use of 0.3 mil (0.75 μm) tantalum foils we have extended the operating life of our targets at maximum beam intensities from hours to weeks. Figure 2.19 shows a comparison between the effects of high-intensity beam exposure for stainless steel and tantalum foils. While the stainless steel foil suffered a complete rupture after several hours, the tantalum foil only begins to show signs of any kind of wear after more than 60 hours of uninterrupted beam.

2.11 Conclusions

We have built and demonstrated a molten lithium target station capable of delivering more than 10^{10} ^{6}He/s to a low-background experimental area using the ^{7}Li(d,^{3}He)^{6}He reaction. At our maximum operating conditions, the HVEC FN tandem Van de Graaff accelerator located in house at the Center for Experimental Nuclear Physics and Astrophysics can provide deuterons at energies up to ∼18 MeV and currents up

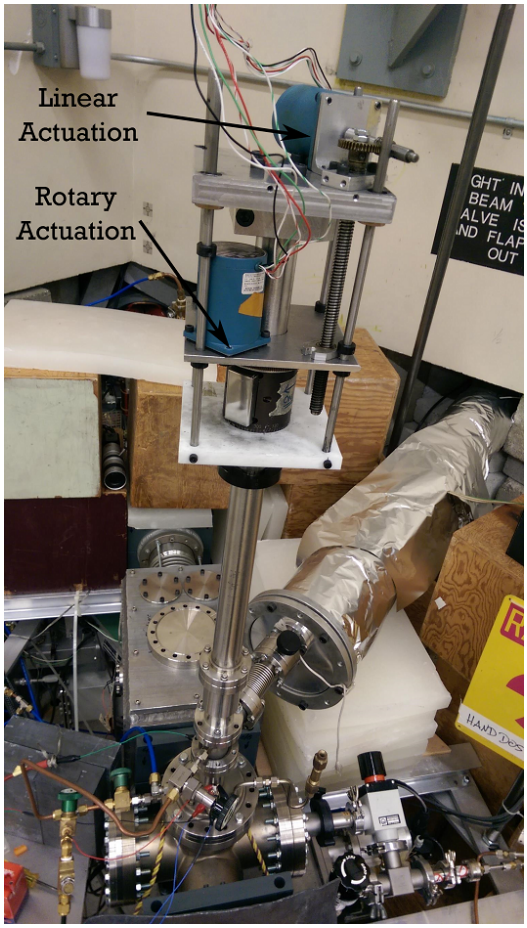

Figure 2.20: The remotely-controlled auto-stirring hardware which operates the internal stirring paddle of the lithium target.

to 15 μA, yielding sustained ^{6}He production rates exceeding 2×10^{10}/s delivered to a low-background environment well-suited for precision measurements [50]. To our knowledge, this is the highest-intensity source of ^{6}He presently available [51, 52, 53], and is comparable to high flux reactor experiments conducted during the 1960s using the ^{9}Be(n,α)^{6}He reaction [54, 55].

Chapter 3

The Half-life Measurement of ^{6}He

The high-intensity source of ^{6}He we've constructed allows for additional high-precision measurements to be performed en route to the angular correlation measurement. To this end, we have measured the half-life of ^{6}He to a relative precision of 3×10^{-4} which is 6 times more precise than that of the previously accepted value 806.7 ± 1.5 ms [56]. This value was obtained by averaging over several previous experiments (see Figure 3.1 and Table 3.1 for a compilation of past results). If we restrict ourselves to looking only at past measurements with uncertainties less than 1% we find a discrepant averaged value of 800.6 ± 2.0 ms. However, the spread of past reported half-life measurements is much larger than one would expect by comparing their respective uncertainty levels. For this reason it was suggested [57] that new, improved measurements be performed. This chapter details our experimental efforts and resulting half-life of $806.89 \pm 0.11_{\text{stat}}\,^{+0.23}_{-0.19\,\text{syst}}$ ms. Some portions of this chapter have been adapted from [35], on which I was a co-author.

3.1 Introduction

Precision measurements of electroweak processes in light nuclei can provide important tests of our understanding of electroweak interactions in the nuclear medium.

Table 3.1: Compilation of all previously obtained ^{6}He half-life values taken from [58, 59, 60, 61, 62, 57, 63].

Year	Half-life (ms)	Year	Half-life (ms)
1946	850 ± 50	1956	852 ± 16
1947	870 ± 60	1958	830 ± 20
1948	820 ± 60	1962	797 ± 3
1949	823 ± 13	1962	862 ± 17
1952	860 ± 30	1963	830 ± 20
1952	840 ± 30	1974	808.1 ± 2.0
1953	830 ± 30	1981	798.1 ± 1.0
1954	799 ± 3	1982	805.4 ± 2.0
1955	850 ± 30	2002	810 ± 8

Many interesting problems – ranging from solar fusion to neutrino interactions and muon and pion capture processes – depend on their correct modeling and calculation [64]. Recent progress in numerical techniques enables precise, *ab initio* calculations of wave functions for light nuclei starting with the nucleon-nucleon interaction and without assuming a frozen core of inactive particles [65, 66, 67]. The allowed weak nuclear decays driven by the axial current have historically played an important role in testing wave functions because the main operator has a simple spin and isospin structure and does not possess any radial component. Systematic comparisons using shell-model wave functions showed that in order to reproduce observations the value for the weak axial coupling constant, g_A, had to be "quenched." For the *sd*-shell nuclei this difference amounted to about 30% with respect to that measured in free neutron decay [68, 69]. In addition, when charge-exchange reactions were used to explore a large fraction of the Gamow-Teller strength sum rule, evidence also pointed

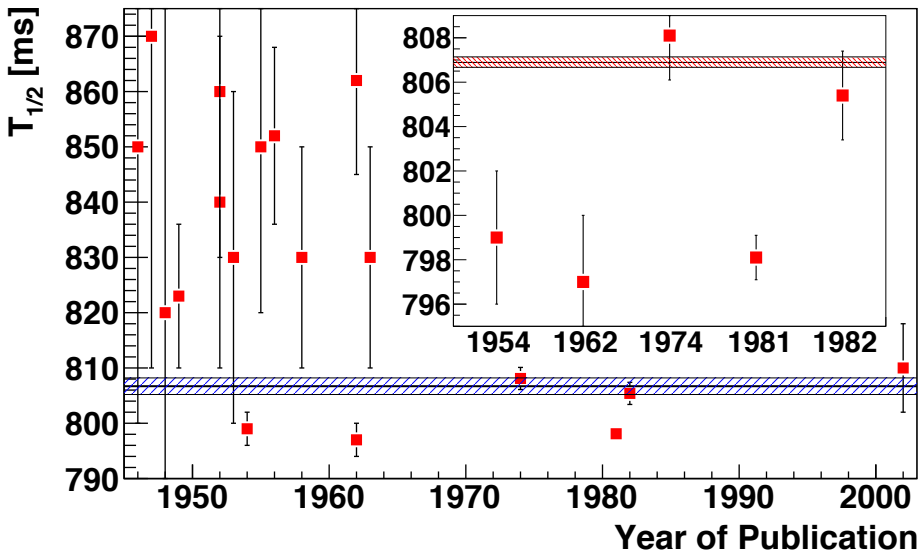

Figure 3.1: Compilation of reported ^{6}He half-life measurements found in past experiments [58, 59, 60, 61, 62, 57, 63]. The blue band shows the half-life adopted in Ref. [56] from the average of the two values found in Ref. [61, 57] and used in compilations ever since. The inset shows the five values with uncertainties below 1% [59, 60, 61, 62, 57] with the red band depicting the value for the ^{6}He half-life obtained in our experiment.

to "quenching of the Gamow-Teller strength" [70, 71]. However, the origin of the quenching is not completely clear. References [70, 72, 73] showed that, as shell-model calculations are allowed to introduce higher and higher excitations, the need to renormalize operators disappears. But it has also been pointed out that meson-exchange currents (mediating, for example, nucleon-delta excitations) could be responsible for at least some of the apparent quenching of strength [15, 74].

The decays of ^{3}H and of ^{6}He are special because these systems are light enough that the corresponding *ab initio* calculations can be performed with precision. In particular, references [67, 75] and later [76, 77] have shown that, using the case of ^{3}H to fix nucleon-delta excitations, the ft value for ^{6}He can be calculated to within a few percent. These two decays, then, can play an important role in testing the accuracy

of nuclear wave-function calculations [67, 75, 76] or, as suggested in reference [77], in fixing low-energy constants in effective-field-theory calculations [64].

3.2 Experimental setup

To perform the half-life measurement, we delivered via turbo-molecular pump our produced ^{6}He into a 35 mm diameter, 381 mm long stainless steel tube which served as our measuring volume. The measuring volume could be separated from the rest of the vacuum via an O-ring sealed spring valve which we could actuate remotely. At the detection end of the tube, a 254 μm thick copper foil separated the ^{6}He inside from atmosphere. On the outside of the foil we mounted two identical beta detectors, each consisting of a 2.5 mm thick plastic scintillator coupled to model R1450 Hamamatsu photomultiplier tubes (PMT) via light guides. These plastic scintillators were placed as close together as possible, separated only by the thickness of the PMT housings which amounted to a 3.5 cm separation.

For 8 seconds we bombarded our target (described in section 2.3) and opened a spring valve from the outlet of a turbo-molecular pump to our measuring volume (see Figure 2.15). At the same time we closed a spring valve which connects the exhaust of the turbo-molecular pump to its roughing pump. During this time ^{6}He was allowed to accumulate in the measuring volume until the decay rate measured by the PMTs reached a steady-state. For the following 16 seconds we deflected the deuteron beam away from the target and closed the valve connecting the turbo-molecular pump to the measuring volume. Immediately after this valve was closed, the partner valve leading to the roughing pump opened and the remaining ^{6}He exhaust was pumped away. During this period we performed a time series count of the number of decays measured and recorded the decay curve. This 8 seconds on, 16 seconds off period constituted one cycle. For 100 ms at the end of the counting cycle we opened up both valves so that both the exhaust of the turbo-molecular pump and the measuring

volume could be pumped away and prepared for the next cycle. In anticipation of possible systematic effects associated with ^{6}He diffusion into the stainless steel walls of our measuring chamber, we inserted at random times a 19 mm diameter, 283 mm long stainless steel rod into our measuring volume for half of our runs. With this rod in place, the ^{6}He would collide with a stainless steel surface 80% more often than without the rod, so we could make a comparison between each scenario and draw conclusions about the effect diffusion into the walls could play in our results.

Upon detection the PMT signals were sent to Ortec model 474 timing filter amplifiers which shaped the PMT signals before delivering them to LeCroy model 821 leading-edge discriminators whose thresholds were set above the electronic noise level. The discriminators provided logic signals which when combined in coincidence formed a logic pulse of 25 ns. This raw coincidence signal was sent simultaneously to a 24-bit LeCroy model 2551 scaler as well as split into 4 channels and sent to a LeCroy model 222 gate generator. The gate generator provided each channel with a different fixed, non-extendable dead time with nominal lengths of 2 μs, 4 μs, 6 μs, and 8 μs, respectively. We later measured the dead times to in fact be 1.9819(81) μs, 3.9990(81) μs, 6.0026(83) μs, and 7.9758(83) μs, respectively, which will be described in more detail in Section 3.5. We also sent to the scaler a 1 kHz and 100 kHz clock. The 1 kHz clock served as a 1 ms time stamp as well as a signal to our DAQ computer, which runs using the software package JAM [43], to read out the scalers. The 100 kHz clock was used principally for detecting errors in our readout which would manifest in a number of ways, some of which were correctable. JAM recorded the data as event files which we converted into ROOT [78] structures for later analysis.

3.3 Data processing

To process our data, we designed our ROOT structures such that there were nine branches: Two branches recorded the Ortec 811 ADC readings from our ΔE1 and

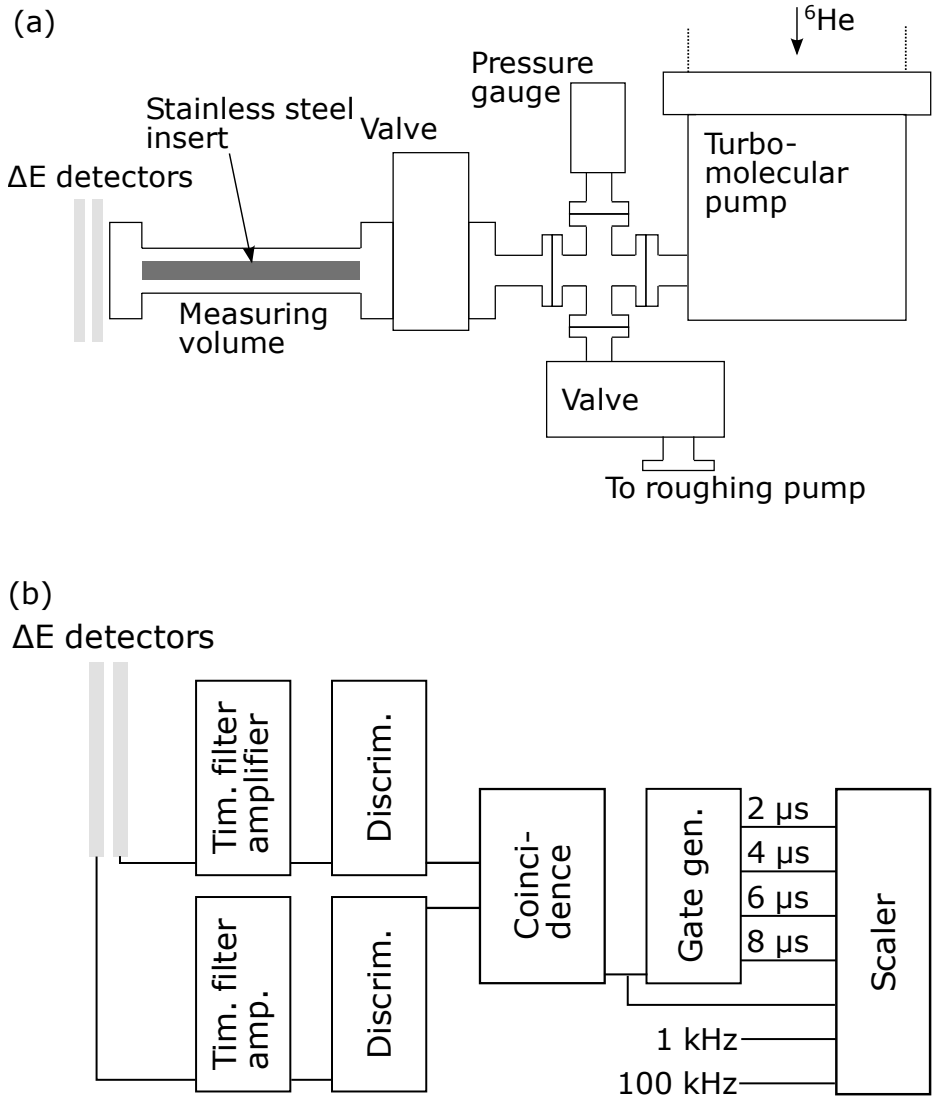

Figure 3.2: Setup of our ΔE-E detector for the ^{6}He rate measurements. Panel (a) shows the experimental setup with two thin scintillators placed in front of a measuring volume which can be closed off by a spring loaded valve. The stainless steel insert was used to determine possible systematic effects due to diffusion of ^{6}He into the walls of the measuring volume, while (b) shows the schematic of the electronics setup. Dimensions are not to scale.

ΔE2 detectors. Seven other branches contained records of scaler readings, composed

of two channels for the 1 kHz and 100 kHz clocks, one for the raw coincidence triggers, and four for each coincidence trigger with nominal dead times of 2 μs, 4 μs, 6 μs, and 8 μs. The 1 kHz clock also served as our time stamp, and so each bin is 1 ms long. These scaler channels always increase until they are reset per cycle, and since the scaler has 24 bits, it exceeds our total number of events in a 25 second cycle by an order of magnitude so it is not at risk of overflow errors.

We had noticed during this sorting process a number of error types. We classified these errors as one of two types: "timing" errors and "scaler" errors, the latter of which we referred to as spikes. Each class of errors had a number of failure modes, some of which were correctable, and some of which were either not correctable or so rare that discarding them was more efficient than trying to correct them.

3.3.1 Timing Errors

For timing errors, one of two things could occur. The first is that the 1 kHz clock channel, which also served as the signal for JAM to record the scalers, was not properly registered by our DAQ computer. We suspect this was due to background processes interfering with the priority of the JAM software. The result of this kind of error is shown in Figure 3.3. The errors are made obvious by looking at the 1 kHz clock records. Though the scaler incremented without issue the signal it simultaneously generates, which we call the Look-at-Me or LAM signal, was not read by the DAQ computer or stored in our event files. Therefore, inspection of the 1 kHz scaler series would appear to miss bins, e.g., would read as $..., 99, 100, 101, 103, 104...$, missing the 102 ms bin entirely and therefore not recording the scaler values for all the other channels. When we looked at the data, we first zeroed an array of 25000 bins, one for each millisecond. We then read the scaler series and filled the bins according to their numerical value, and not their position in the series. This new array became our new time series and the error discussed before would be seen as $..., 99, 100, 101, 0, 103, 104, ...$

We filled our scaler counts for each of the other channels in the same way which resulted in a consistent looking count with bins of zero value periodically dispersed in time. Most of the time (about 81%) these missed reads were not followed by an additional missed read. About 18% had two missed reads in a row. Any cycle that had more than 4 missed reads in a row is discarded. Those with fewer than 4 missed reads were corrected via averaging of the surrounding bins.

The next type of timing error occurred when the time series is out of order in certain places, reading for example $..., 99, 100, 104, 105, 101, 102, 103, ...$ Though we don't know how these events happened, they occurred quite rarely and cycles containing them were discarded instead of corrected.

3.3.2 Spikes

The next class of errors were named "spikes." This is because we computed the coincidence rate by taking the difference between scaler values from 1 ms to the next. If there were problems in the scaler counts such that they were lower or significantly higher than the previous millisecond, this derivative would result in a large positive or negative spike in the rate (see Figure 3.4), making spikes easy to identify. The kinds of spikes unrelated to the timing errors listed above manifested in an incorrect scaler reading due to a bit error in the scaler caused by the DAQ computer reading out the data while the scaler is updating. We further subdivided these spikes into three distinct types.

Type-1 spikes occurred when the ith undifferentiated scaler value decreased from the $(i-1)$th, but the $(i+1)$th value was larger than either of the other values (see Figure 3.5). Because these were related to the scaler updating, they were rate-dependent (see Figure 3.6). These errors were correctable by setting the defective bin value to zero to effectively reclassify these errors as missed read errors which were then corrected via averaging over adjacent values as before.

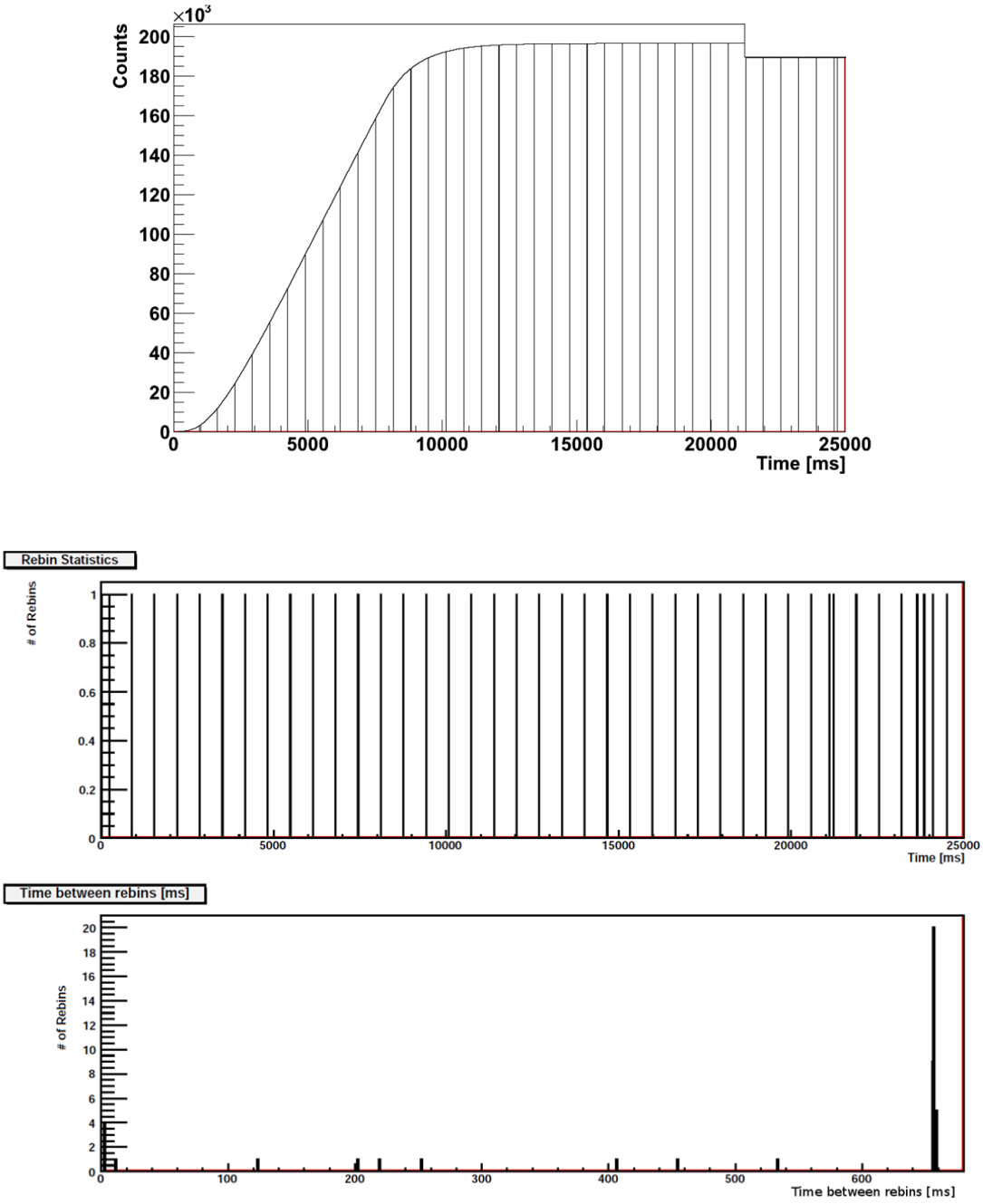

Figure 3.3: The top panel shows a sample timing error type 1: The "Look-at-Me" (LAM) signal generated by the 1 kHz clock was not read by the DAQ computer resulting in a loss of scaler counts for that particular 1 ms bin. The scalers were still incremementing properly, so the count was correct during the next LAM reading. Later we corrected these errors via averaging over the affected bins. The bottom panel shows the regularity and frequency of these kinds of missed reads. They occurred on average about ∼650 ms apart.

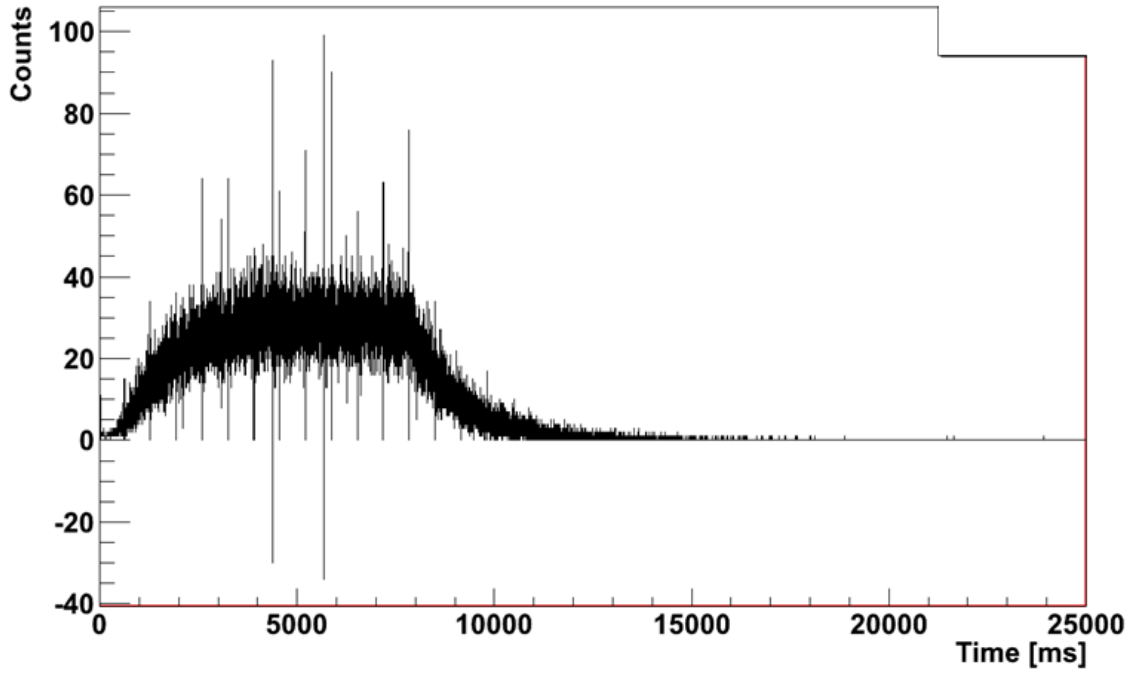

Figure 3.4: A sample rate cycle with spikes included. Large positive and negative spikes are caused by misreading the scalers by one bit resulting in a value off by 2^n across all channels. These bit flip errors can be seen most easily in the 100 kHz clock channel. Note that missed reading errors are also seen here as regular dips to zero. Those are "time" errors, not spikes.

Type-2 spikes occurred much like Type-1 spikes, only the $(i + 1)$th value did not restore itself to the correct scaler value and instead remained a decreased value (see Figure 3.7). There are actually two errors that occur in order here. First is a small 2^n dip in the scaler value followed immediately by a 2^{16} drop. From here the scaler continued to increment but the count was no longer correct. These events were somewhat rare and we discarded any cycle that contained these kinds of errors.

Type-3 spikes occurred when the scaler value, for example on the 100 kHz clock, was larger than it should be by a factor of 2 or 4. Immediately following this type of

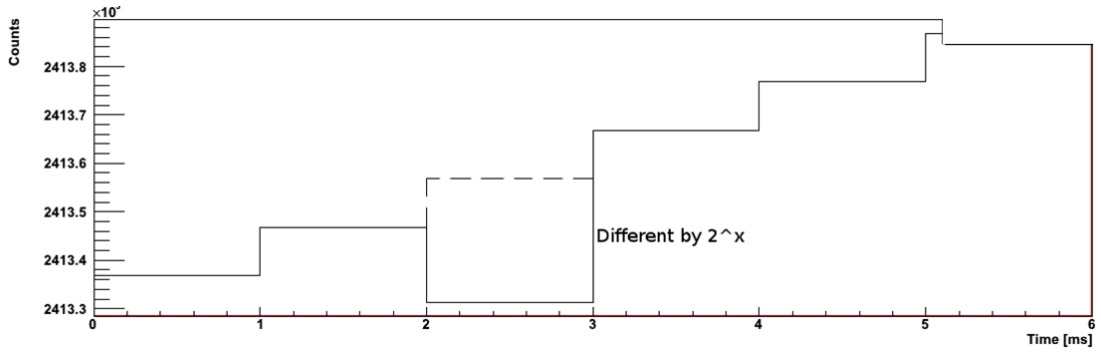

Figure 3.5: A sample of the 100 kHz clock scaler when a Type-1 spike occurs. The defective value is different from its correct value by some 2^n factor corresponding to a bit error. Type-1 spikes return the scaler to the correct value on the following read.

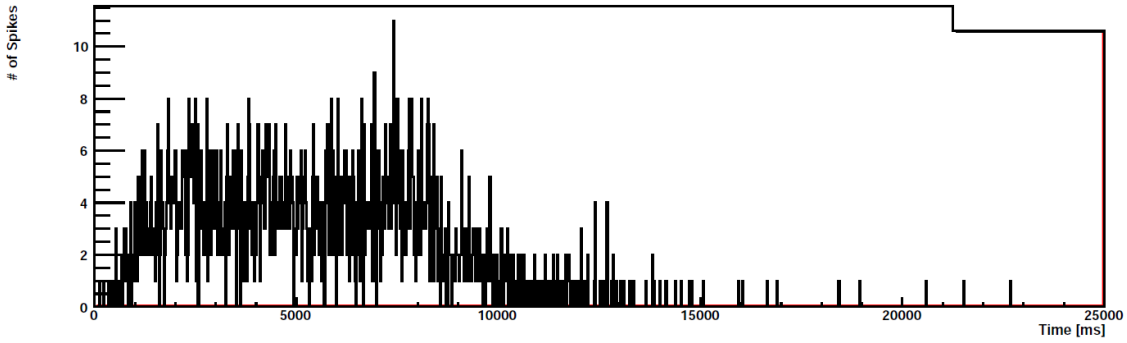

Figure 3.6: This histogram of spike occurrences was made with a subset of the data recorded on one scaler channel. The rate dependence of spikes is easily seen by its similar shape and time structure when compared with the rate cycle seen in Figure 3.4.

error were 1 to 3 missed read errors (see Figure 3.8). Essentially it was the reverse of the main timing error, where instead of a few zeroed bins followed by a correct scaler reading, the following 1 to 3 bins were read as having been counted in the previous bin. This was likely a delayed reading effect caused by a "hiccup" in the DAQ computer. Since these were similar to the missed read errors, they could be

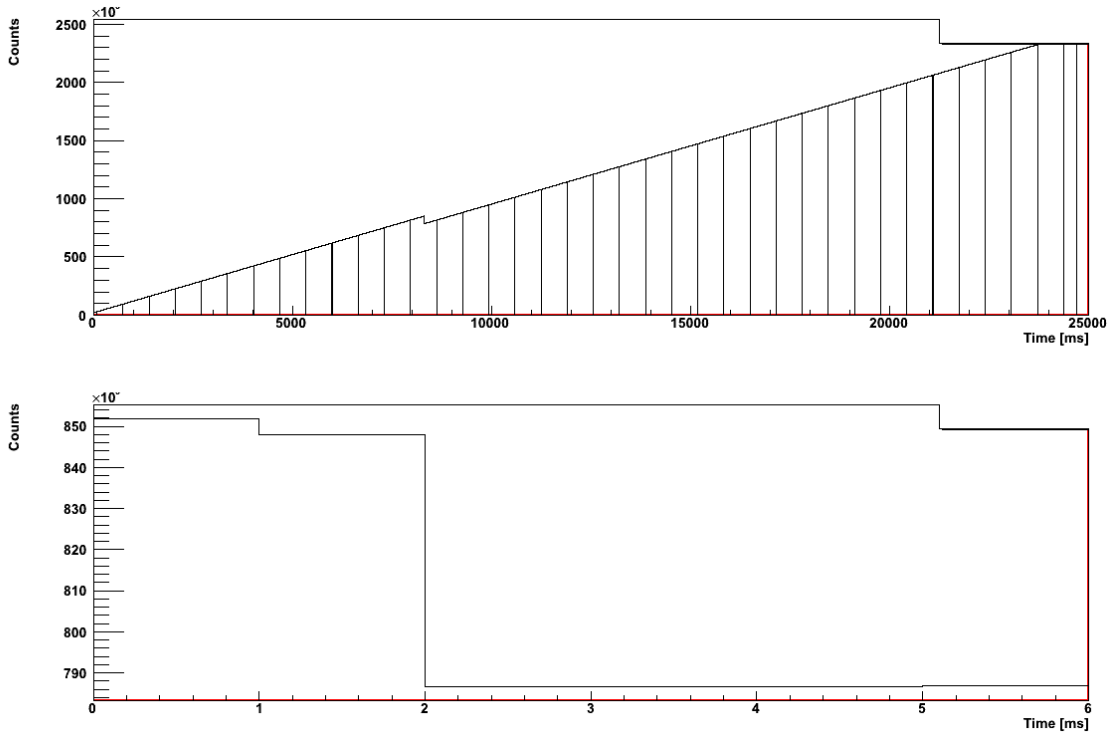

Figure 3.7: (top panel) A sample of the 100 kHz clock scaler when a Type-2 spike occurs at around 8500 ms. (bottom panel) A zoom in around this time. The defective value is different from its correct value by some 2^n factor corresponding to a bit error. Type-2 spikes do not return the scaler to the correct value on the following read. They are always accompanied by a slight decrease in the scaler value just preceding the large 2^{16} bit error.

corrected in a similar fashion. However, they were exceedingly rare, occurring only $\sim$10 times out of more than 1200 cycles.

The effect that these corrections have on our final result are minimal and will be discussed in section 3.6.

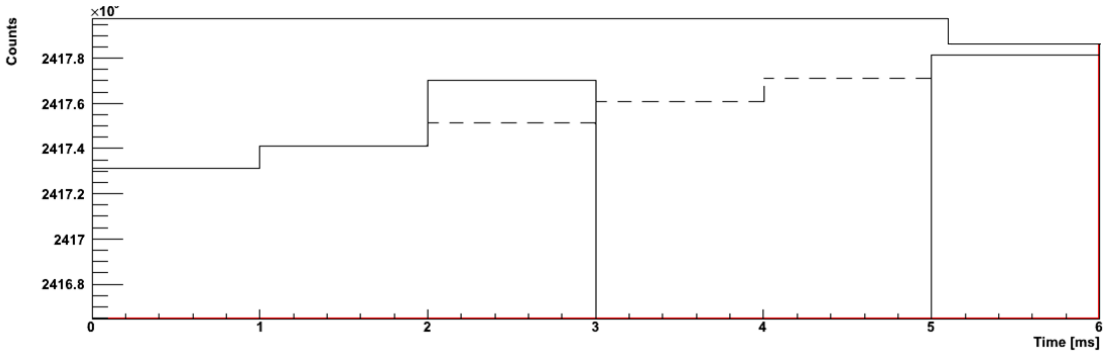

Figure 3.8: A sample of the 100 kHz clock scaler when a Type-3 spike occurs. Here an anomalous bin is larger than it should be and is followed by a number of missed reads such that the missed reads are all piled into the anomalous bin. These are correctable errors, but are rare.

3.4 Putting limits on ^{8}Li contamination

^{8}Li was a potential contaminant for this measurement because it is also made in large quantities as a by-product of the ^{7}Li$(d,p)^{8}$Li reaction process which can also take place when producing ^{6}He through the ^{7}Li$(d,^{3}$He$)^{6}$He reaction. ^{8}Li is a beta emitter with a half-life very close to our expected ^{6}He half-life ($T_{1/2} = 838.40(36)$ ms for ^{8}Li [79] vs. $T_{1/2} = 806.7 \pm 1.5$ ms [56] expected for ^{6}He). However, the beta endpoint is quite different (16.0 MeV for ^{8}Li vs. 3.5 MeV for ^{6}He), allowing for a way to identify production of significant amounts of ^{8}Li with a thick scintillator to measure the beta energy.

We did not expect to see much if any ^{8}Li near our detectors because the lithium would tend to stick to the bulk lithium or to the walls of our vacuum system after many collisions, whereas helium would not stick to the walls because it is a noble gas. Nevertheless we checked for signatures of ^{8}Li by running the beam at an energy below the 5.8 MeV production threshold for ^{6}He but above the 0.25 MeV threshold for ^{8}Li.

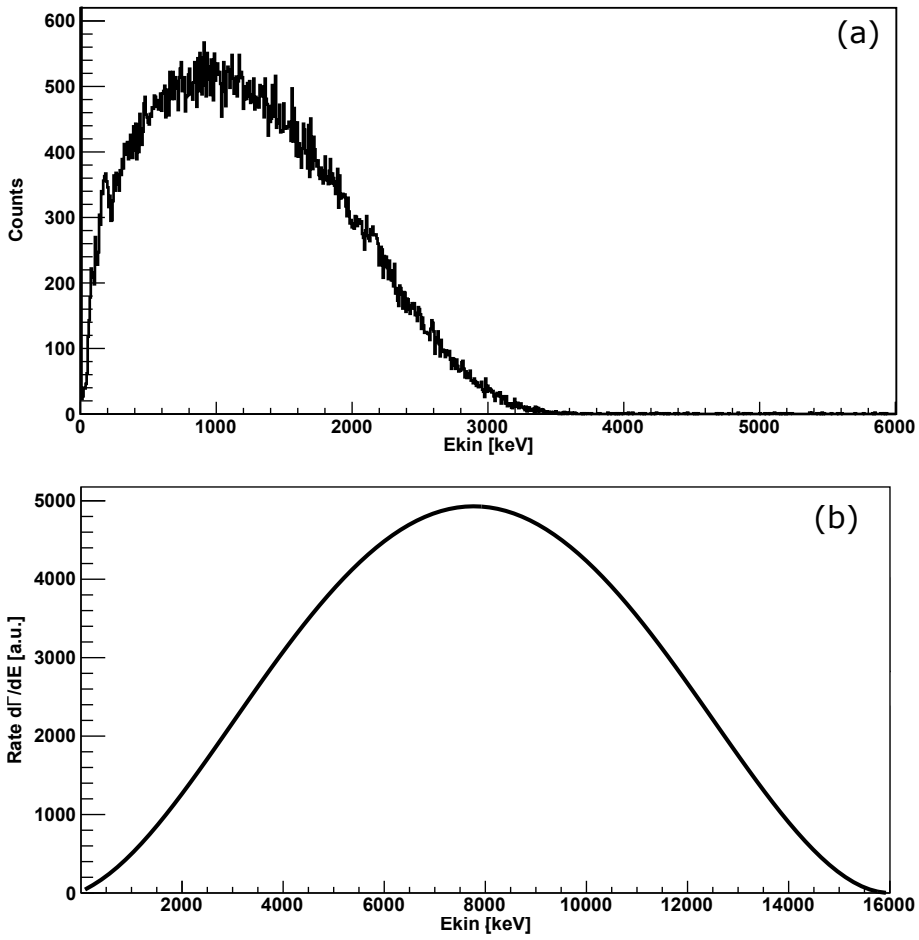

Figure 3.9: Comparison between our measured energy spectrum in panel (a) and analytic spectrum of ^{8}Li in panel (b). The absence of any significant counts above the ∼3.5 MeV β-decay endpoint of ^{6}He places strict limits on the presence of any contaminants near the detectors.

Here we used the two ΔE detectors as before but backed by a large, thick E detector to measure the total energy of the betas. We found that we still had production below the threshold for ^{6}He, but the energy distribution and observed half-life of 810 ± 5 ms were consistent with ^{6}He and not ^{8}Li. Though this is below the threshold for the primary ^{7}Li(d,^{3}He)^{6}He reaction, the lithium used contains a natural abundance of

$\sim$7.6% ^{6}Li, and neutrons generated by the ^{7}Li(d,n) reaction can produce ^{6}He via ^{6}Li$(n,p)^6$He, and our production rates at these energies were consistent with rough estimations of production via this process. See Figure 3.9 for a comparison of our measured energy spectrum vs. an analytic spectrum for ^{8}Li. To estimate the amount of ^{8}Li which may contribute to our measured decay rate, we integrated the energy spectrum above the ^{6}He endpoint after background subtraction to calculate a limit of 2×10^{-4} at 68% C.L. on the fraction of possible ^{8}Li production present in our final results. This contamination limit results in a systematic uncertainty of 0.007 ms in our final reported lifetime for ^{6}He.

3.5 Deadtime measurement

To calculate the true rate of decays given our hardware dead time, we needed to carefully measure how much dead time was actually present in each channel for later correction. Once measured, we corrected our histograms for dead time losses on a cycle-by-cycle basis by using the measured rate in each time bin R to calculate the actual decay rate R_{true} given a measured deadtime τ_d from the following equation[80]:

$$R_{true} = \frac{R}{(1 - R\tau_d)} \tag{3.1}$$

We measured the dead time for each scaler channel (nominally nonextendable 2 μs, 4 μs, 6 μs, and 8 μs dead times) using the source+pulser method described in [81]. A source of constant frequency, our pulser, runs at 10 kHz. A sample of ^{90}Sr provides a random source. By measuring the rates of each source separately as well as mixed into the same channel, the dead time τ_d can be calculated. We measured the rate of ^{90}Sr decays through each scaler channel for 15-20 minutes and counted the number of events while a 10 Hz clock recorded the elapsed time from which we could determine the exact rate measured for each channel. We repeated this measurement with the

pulser mixed in with the ^{90}Sr signals. From this we calculated the dead time:

$$\tau_d = \frac{1}{R_r}\left(1 - \sqrt{\frac{R_{pr} - R_r}{R_p}}\right) \tag{3.2}$$

Here, τ_d is the determined dead time, R_r is the measured random source rate, R_p is the rate of the pulser, and R_{pr} is the measured rate of the pulser signal mixed in with the random source. The derivation of this result is somewhat difficult to obtain and rests on a number of assumptions about the stochastic processes involved[81]; however, computing the results are straightforward. We made several such measurements following our runs to collect ^{6}He decay data. Averaging these results, which were consistent with each other, yielded the final values 1.9819(81) μs, 3.9990(81) μs, 6.0026(83) μs, and 7.9758(83)) μs.

3.6 Data analysis

During our beam taking run, we operated at several different beam intensities. This resulted in run data that contained different detection rates at the start of the 16 s beam-off period so we could study rate-dependent effects. These data were grouped in to five sets: < 40 kHz, $40 - 50$ kHz, $50 - 60$ kHz, $60 - 70$ kHz, and $70 - 80$ kHz. They were also separated further into groups which had the stainless steel rod inserted and with the rod out. Following this, all the data is rebinned to 10 ms from their initial 1 ms binning to avoid fitting errors caused by insufficient statistics. This also has the effect of diminishing any effects caused by our data correction methods, which at most happen over $3 - 4$ ms bins.

Figure 3.10 shows the full data set for runs with initial rates less than 40 kHz and with the rod out. Immediately after the beam is tuned away from the target following the 8 s bombardment period, there is a small step followed by a wiggling pattern in the decay spectrum that lasts for approximately 200 ms. This was caused by the spring valves near the back of the measuring volume quickly opening and closing as

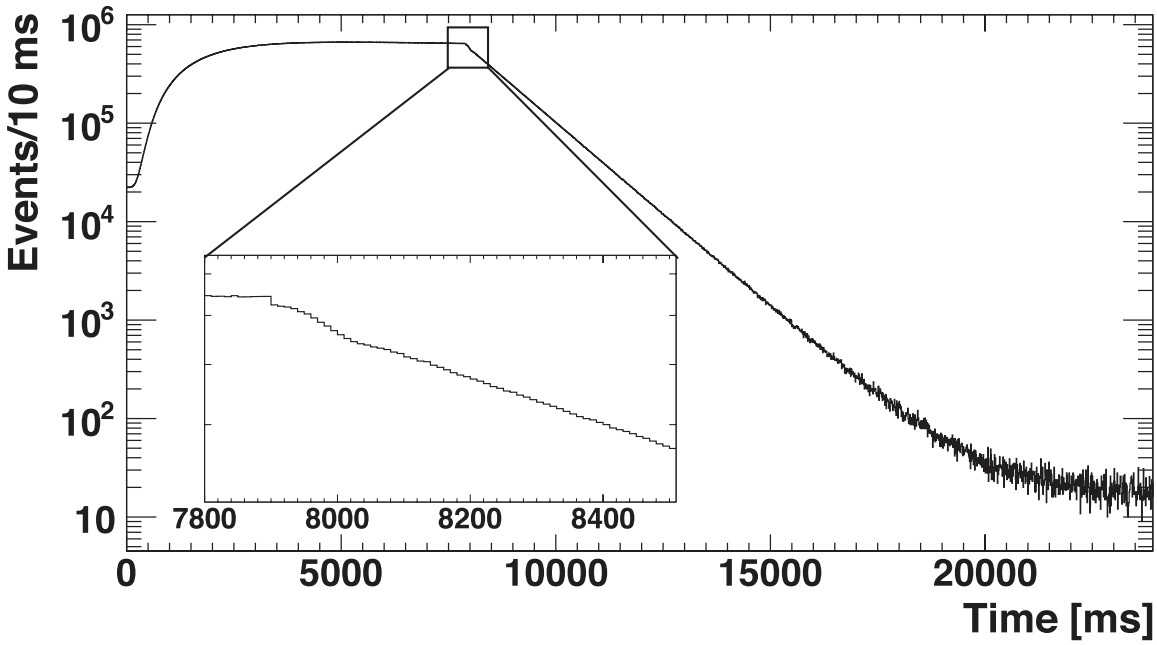

Figure 3.10: ^{6}He full cycle histogram for the data with initial rates < 40 kHz and the stainless steel insert out. The insert zooms into the transition point from beam-on to beam-off.

described in Section 3.2. Due to this effect, as well as the rate-dependent effect of our uncertainty in our dead time correction methods, we did not begin to fit our data until after the wiggling pattern had died out and the decay rate lowered to 32 kHz. For the data that began with a decay rate near 40 kHz, this amounted to starting the fit at 8260 ms, and at later times for higher rate cycles. The endpoint for the fit for all the data was fixed at 23900 ms, which is 100 ms before the beam-off period actually ended.

The Gaussian approximation fails for events with low bin statistics as occurs near the tail end of a half-life measurement cycle. Instead the Poisson distribution must be used. However, because we corrected on a cycle-by-cycle basis the effects of our measured dead time, our bin variances σ_i no longer followed a Poisson distribution,

Method	Exp. data [ms]	M.C. data [ms]
Modified χ^2	806.969 ± 0.114	807.019 ± 0.096
Regular χ^2	806.970 ± 0.114	807.025 ± 0.096
Max. likelihood	806.974 ± 0.113	807.023 ± 0.095

Table 3.2: Fitting results of the data in Figure 3.11 and the Monte Carlo data using different methods. The Monte Carlo simulation consisted 7.45×10^7 events distributed with a half-life of 807 ms and our measured background. Dead time corrections are applied in the same manner as our experimental data. The systematic shifts and uncertainties from Table 3.4 are not included.

but had instead a larger variance. For a Poisson distribution, the χ^2 as derived from the maximum likelihood method is given as follows:

$$\chi^2 = 2\sum_{i=1}^{N} y_{fit} - y_i + y_i \ln\frac{y_i}{y_{fit}} \tag{3.3}$$

Here y_i is the number of events in the ith bin after dead time correction has been applied, y_{fit} is the value of the fit function at that bin, and N is the number of bins in the fit. To account for the fact that the above equation does not depend on the increased variance of each bin from corrections, we followed the modified χ^2 method outlined in [82] by defining a weighting factor W_i which scales the variance for each bin from the Poisson variance y_i (equal to the bin count) to the true variance σ_i^2. We thus define this weighting factor:

$$W_i = \frac{y_i}{\sigma_i^2} \tag{3.4}$$

The χ^2 to be minimized then is the following:

$$\chi^2 = 2\sum_{i=1}^{N} W_i \left(y_{fit} - y_i + y_i \ln\frac{y_i}{y_{fit}} \right) \tag{3.5}$$

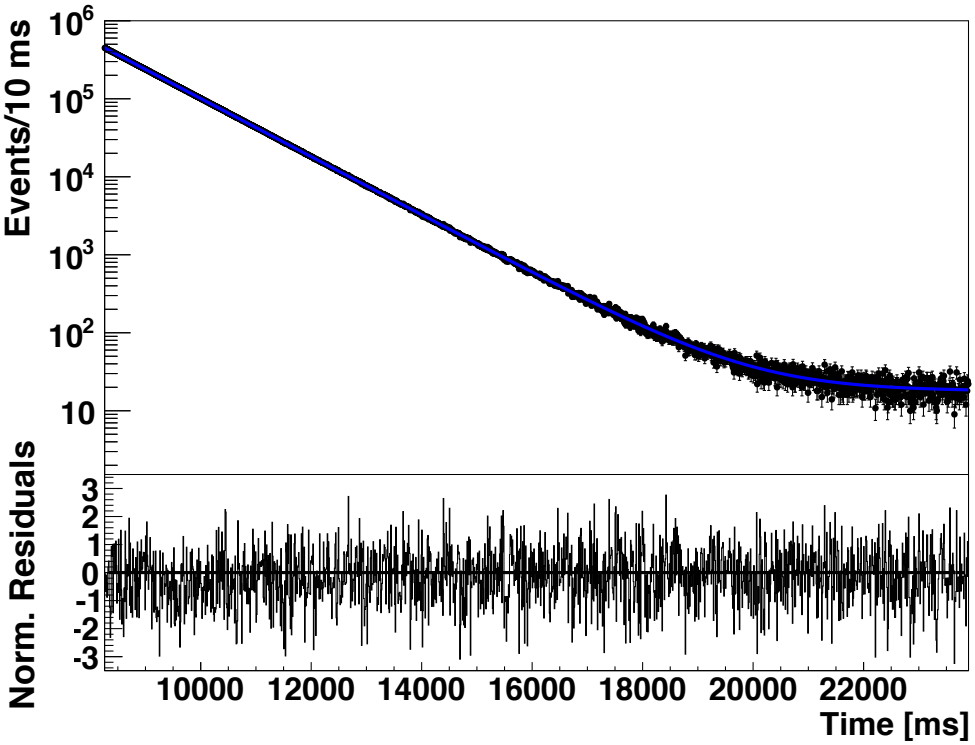

Figure 3.11: ^{6}He decay curve for the same data as in Figure 3.10 (2 μs deadtime, initial rates $<$ 40 kHz and the stainless steel insert out) with the corresponding residuals. The χ^2/dof of the fit is 1578.2/1562.

Using this modified χ^2 we fit the data such as is shown in Figure 3.10. Figure 3.11 shows the data in the fitting region along with corresponding residuals from the fitting function (blue line) $f(t) = N(\exp(-(t-t_0)/\tau)+b)$. Here, N is a normalization given by the fitting function along with the total number of counts, τ is the free fit parameter for the lifetime, and b is also a free fit parameter for a constant background. We also performed this fit using an unmodified χ^2 fit as well as a maximum likelihood fit to check for consistency. Additionally we fit with all three methods Monte Carlo simulations with 7.45×10^7 counts using a given 807 ms half-life and a measured background value. For all simulations we applied dead time corrections in the same manner as our experimental data, and found no bias. The results of these fits can be

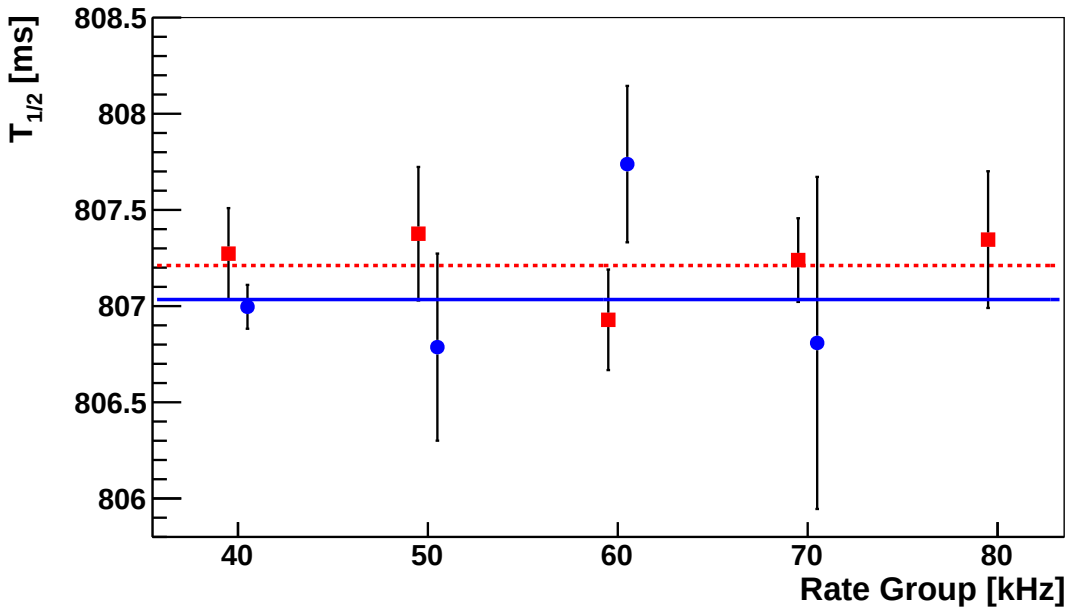

Figure 3.12: ^{6}He fit results for the different rate groups with the initial rate restrained to 32 kHz. Only statistical errors are given. The squares (circles) correspond to the stainless steel insert in (out) data. The dashed (solid) line shows the constant fit to the insert in (out) data with χ^2/dof of 1.6/4 (3.4/3). The results of the constant fits correspond to the averages given in Table 3.3.

found in Table 3.2.

We sorted these fits into two categories depending on whether the stainless steel insert was in or out. Then we looked at the results for each rate group after combining all the dead time channels together via weighted averaging, shown in Figure 3.12. We also averaged the results over all rate groups for each dead time channel, as shown in Table 3.3. Also shown in Table 3.3 are the averaged values over all rate groups and dead time channels for the stainless steel insert in and out cases, which we will use to determine the possible systematic effects of ^{6}He diffusion into the surfaces of the vacuum hardware which could act as an additional loss mechanism.

Insert	τ_d	Results [ms]	Average [ms]
out	$\sim$2 μs	807.01 ± 0.11	807.03 ± 0.11
	$\sim$4 μs	807.03 ± 0.11	
	$\sim$6 μs	807.08 ± 0.11	
	$\sim$8 μs	807.02 ± 0.11	
in	$\sim$2 μs	807.20 ± 0.12	807.21 ± 0.12
	$\sim$4 μs	807.20 ± 0.12	
	$\sim$6 μs	807.21 ± 0.12	
	$\sim$8 μs	807.23 ± 0.12	

Table 3.3: List of the different half-lives obtained with various deadtimes and for the cases of the stainless steel insert in and out. The systematic shifts and uncertainties from Table 3.4 are not included.

3.7 Systematic Uncertainties

In Table 3.4 we give our estimates of systematic shifts and uncertainties that are described in detail in the following paragraphs. In several cases we used a simulation to determine the magnitude of the systematic uncertainty. The simulation consisted of generating $\sim 10^{10}$ (statistical uncertainty of 0.01 ms on the half-life) random events distributed with a half-life of 807 ms and our measured background. We then applied to the time-ordered events the different systematic effects and fit the data to determine the deviation from the input half-life.

3.7.1 Dead-time

The effect of the dead-time correction is large. The correction shifts the half-life values by -9, -18, -27, and -35 ms for the four different dead-time channels, respectively.

Source	Shift [ms]	Uncertainty [ms]
Deadtime correction	-	0.037
^{6}He Diffusion	0	$^{+0.12/+0.22}_{-0}$
Gain shift	-0.19	0.19
^{8}Li contamination	0	$^{+0}_{-0.007}$
Background	0.046	0.004
Data correction	0	0.01
Deadtime drift	0	0.009
Afterpulsing	0	0.003
Pile-up	0	0.00005
Clock accuracy	0.006	0.011
Total	-0.14	$^{+0.23}_{-0.19}$ / $^{+0.29}_{-0.19}$

Table 3.4: List of systematic shifts and uncertainties. We added the errors in quadrature to obtain the total error. Where a second value is given it corresponds to the measurements with the stainless steel insert in.

Insert	τ_d	Results [ms]	Diff. [ms]	σ_{corr} [ms]
Out	$\sim$2 μs	806.999 ± 0.169		
	$\sim$4 μs	806.992 ± 0.170	-0.007	0.017
	$\sim$6 μs	807.000 ± 0.171	0.001	0.025
	$\sim$8 μs	806.963 ± 0.172	-0.036	0.030

Table 3.5: List of the different ^{6}He half-lives obtained with the correlated data in four dead time channels for the case of the stainless steel insert out. The differences and corresponding errors are given with respect to the 2 μs channel.

However, the agreement between the four values after the deadtime correction lends confidence to its validity. The results for the different deadtime channels are highly correlated and their differences should only be influenced by the corresponding loss in statistics, the uncertainty of which is given by $\sigma_{corr} = \sqrt{|\sigma_1^2 - \sigma_2^2|}$. Since our data for different dead-time channels are not completely correlated due to the data preselection, we modified the data preselection procedure to result in the exact same data set for all the dead-time channels. The results for this particular data set are shown in Table 3.5, together with the differences between the 2 μs channel and the other channels and their corresponding error as calculated according to the description above. The differences are consistent with the loss of statistics in the different dead-time channels.

The uncertainty on the measured dead times of $\sim$8 ns translates directly into a systematic uncertainty on the half-life. Figure 3.13 shows the dependence of the fitted half-life values on changes in the dead time as determined from data. The linear slope of -0.00485 ms/ns results in a systematic uncertainty of 0.04 ms. Although a small and constant spread in the fixed dead times does not introduce any systematic uncertainty, a drift in the dead times obviously does. We tracked the length of the

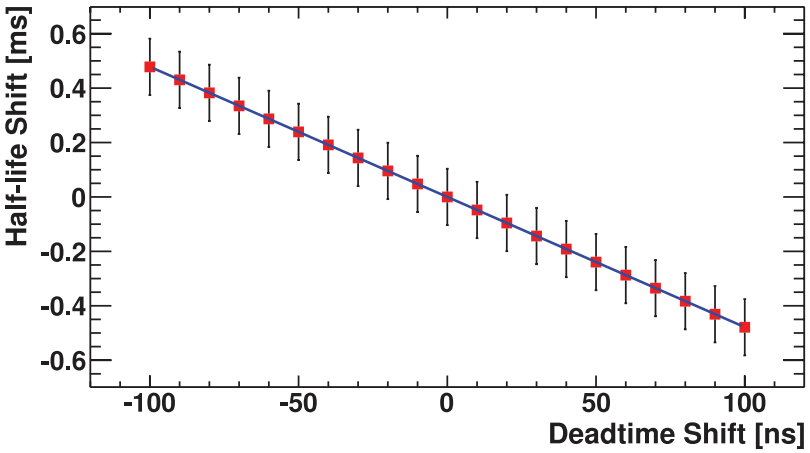

Figure 3.13: Shifts in the fitted ^{6}He half-life values as a function of changes in the dead time used in the dead time correction. The data correspond to the averages of the different dead time channels. The slope amounts to -0.00485 ms/ns.

2 μs gate during 7 days on a digital oscilloscope. Although we observed variations of $\pm$2 ns on a daily basis there was no long-term drift detectable. We attribute a systematic uncertainty of 0.009 ms in the half-life to these observed drifts.

3.7.2 Helium diffusion to the outside

Using a helium leak detector we studied the diffusion of helium through the walls of the measuring volume and the Viton O-ring of the valve at its end. While we did not observe any diffusion through the walls, we did observe the diffusion of helium atoms through the valve O-ring. Figure 3.14 shows the resulting helium gas flow into the leak detector with one side of the closed valve connected to its inlet and the other side filled to 1 atm of helium. In our analysis we follow Refs. [83, 84, 85]. We found acceptable agreement between our data and the predicted gas flow $C(t)$ as given in Eq. (46) of Ref. [83],

$$C(t) = C_0 \left[1 + 2 \sum_{n=1}^{\infty} (-1)^n \exp\left(-(n\pi)^2 \frac{Dt}{d^2} \right) \right] \tag{3.6}$$

for a diffusivity $D = 10^{-5}$ cm^2/s and a steady-state flow $C_0 = 5.7 \times 10^{-8}$ mbar l/s. The thickness d of the O-ring in the valve was measured to be 2.2 mm. There is an uncertainty of about a factor of 2 in the extracted diffusivity due to the thickness and about 20% on the steady-state flow due to the sensitivity of the leak detector. From these two measurements we extract a permeability $K = 10^{-10}$ (cm^3 at STP) mm s^{-1} mbar^{-1} cm^{-2} using an exposed area of $A = 1.2$ cm^2 and a solid solubility $b = 10^{-6}$ (cm^3 at STP) mbar^{-1} cm^{-3} for helium in the Viton O-ring of our valve. Both of these values are in acceptable agreement with values found in the literature. We neglect any mass scaling of the measured flow by $\sqrt{m_{^4\mathrm{He}}/m_{^6\mathrm{He}}}$ and an exponentially decreased diffusivity because of the higher mass. During our cycle length of $T = 16$ s the ^{6}He atoms diffuse a distance $l \sim 2\sqrt{DT}$ into the O-ring, resulting in an absorbed gas volume $V_{gas} = 2\sqrt{DT}Abp_{^6\mathrm{He}}$ at the ^{6}He partial pressure $p_{^6\mathrm{He}}$. The average loss rate over the full cycle thus amounts to

$$\frac{1}{T}\frac{N_{\mathrm{loss}}}{N_0} = \frac{1}{T} p_0 b \frac{2\sqrt{DT}A}{V_0} = 5 \times 10^{-9}\mathrm{s}^{-1} \tag{3.7}$$

with $p_0 = 1000$ mbar, the total number of ^{6}He atoms N_0, and the volume of our measuring volume $V_0 = 367$ cm^3. This represents a negligible shift at our precision.

3.7.3 Helium diffusion into the walls

Although we were not able to observe any diffusion through the walls of the measuring volume, we assume that some diffusion does occur, leading to an additional loss channel. The mean free path $\lambda = 4V/A$ inside our measuring volume V and surface area A leads to a wall-collision frequency $f_c = v/\lambda$ given the velocity v of the atoms. Any time constant $1/\tau_{\mathrm{diff}}$ associated with this loss channel scales linearly with the wall-collision frequency $f_c = v/\lambda$ and leads to a measured lifetime $1/\tau = 1/\tau_{^6\mathrm{He}} +$

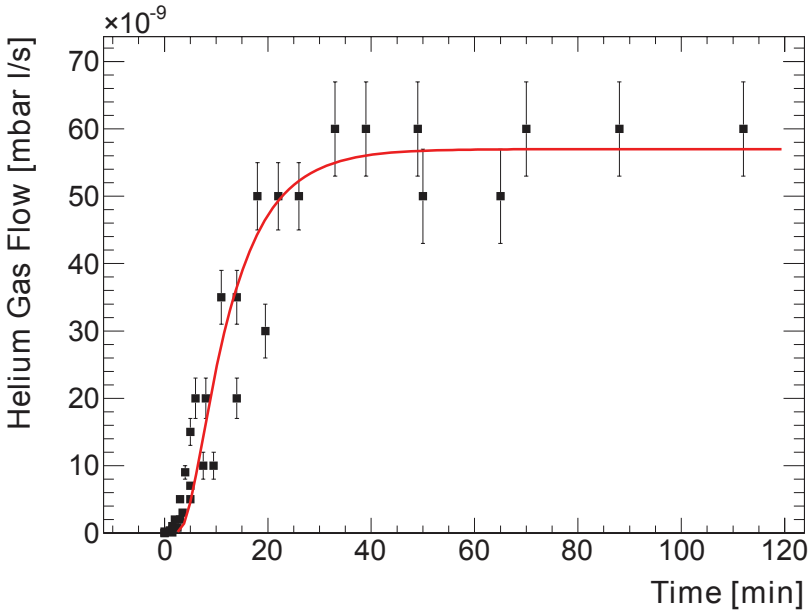

Figure 3.14: Measured helium leak rates through the Viton O-ring of the valve sealing our measurement volume. The plot compiles three separate measurements. The line shows the prediction for the gas flow according to Eq. (46) of Ref. [83] for a diffusivity $D = 10^{-5}$ cm^2/s and a steady-state flow $C_0 = 5.7 \times 10^{-8}$ mbar l/s.

$1/\tau_{\text{diff}}$. From the absence of any significant difference between the two results listed in Table 3.3 we conclude that $\tau_{\text{diff}} \gg \tau_{^6\text{He}}$ and the difference between the two results is $\Delta(1/\tau) = 1/\tau_{\text{in}} - 1/\tau_{\text{out}} = (-2.8 \pm 2.5) \times 10^{-7}$ ms^{-1} $= 0.8/\tau_{\text{diff}}$ where the factor 0.8 is due to the 80% increased wall-collision frequency with the insert in place. We set the Gaussian probability density function to zero in the nonphysical region [37] and calculate an upper limit on $1/\tau_{\text{diff}}$ at a 68% confidence limit (C.L.) of 2×10^{-7} ms^{-1}. This translates into a systematic uncertainty for the insert in and out data of $^{+0.22}_{-0}$ and $^{+0.12}_{-0}$ ms, respectively.

3.7.4 Gain shift

Examining our highest rate data, we identified traces of a small, rate-dependent shift, which is not fully accounted for by our dead-time correction. Though pileup effects could potentially be the cause of such a shift, based on the arguments given below its effect is too small to contribute. Therefore, because the values are shifted toward higher half-life values, we attribute it to a negative decrease in gain with increased rate in the photomultiplier tubes. For a potential reduction in gain of 10% a fraction of 10^{-3} of the counts falls below threshold as determined from the pulse-height measurements performed at the beginning of the data taking. This would lead to a systematic shift of the half-life of 0.16 ms as obtained from our simulations and gives the approximate order of magnitude of such potential gain shifts. To investigate the size of the rate-dependent shift from our data constrained to 32 kHz itself, we added a parameter k to our fitting function to model the effect of a linear rate dependence by substituting in our fitting function $R(t) \rightarrow R(t)[1 - kR(t)]$. The resulting shift in the half-life due to including the parameter k amounts to -0.19 ± 0.19 ms, showing no significant rate-dependent effect after corrections. We did not observe any difference in this shift between the two data sets with the stainless steel insert in or out. As a consistency check, we also examined our data by plotting the fit results as a function of start time shown in Figure 3.15. Because the start time of the fit is different in each of the rate groups the values are given as a function of "delay time" corresponding to the delay of the start time in each rate group. The two solid lines on that plot correspond to the $\pm 1\sigma$ contours given by the loss in statistics for this correlated data set. The data around the rather large drop at about 3 s was studied in more detail in search of a potential artifact but we concluded there is no anomaly.

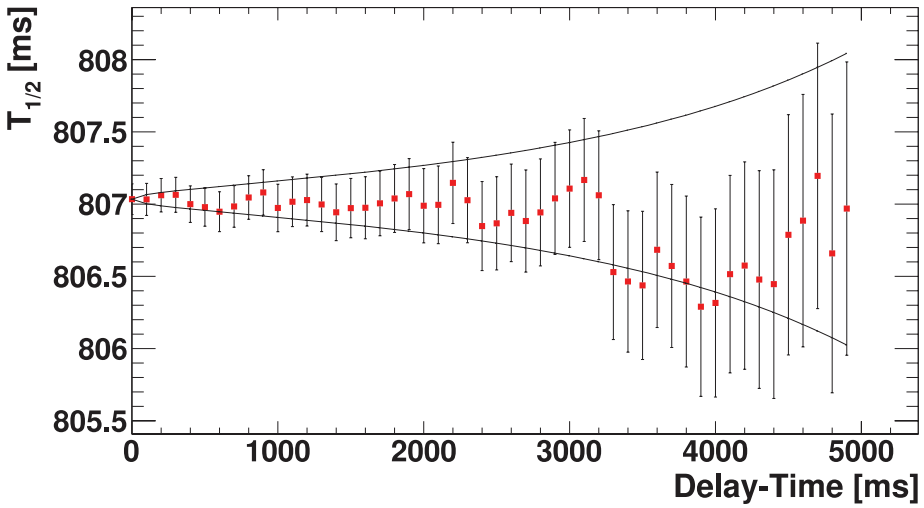

Figure 3.15: ^{6}He half-life values as a function of delay in the starting point of the fits. The two solid lines correspond to the $\pm 1\sigma$ contours for the allowed variation (relative to the first data point) that one expects from the loss in statistics for this correlated data set.

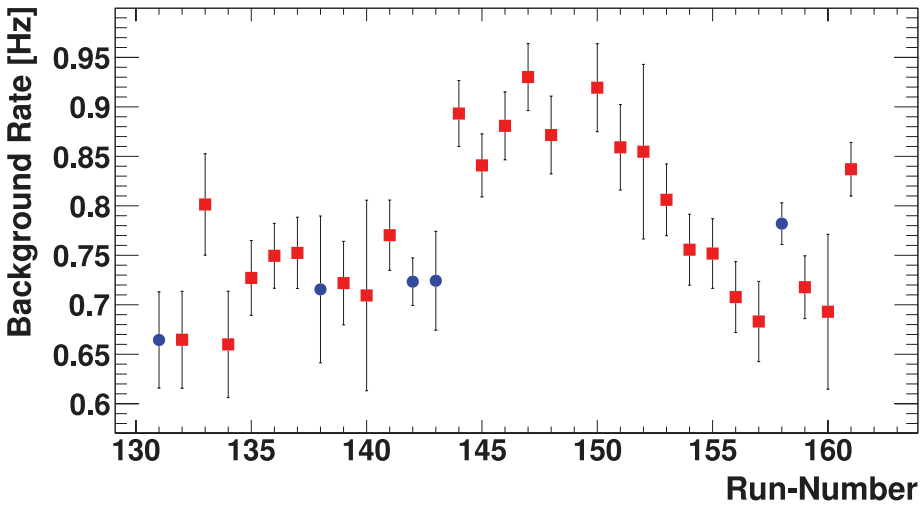

Figure 3.16: Measured background rates during dedicated background runs (blue circles) and fitted background rates in half-life data taking runs (red squares).

3.7.5 Background

Throughout the data taking we performed several background runs in which we kept the valve in front of the measuring volume closed but otherwise operated the experiment just like for the other runs. Our background runs are distributed across all of the lifetime data and largely average out the changes in background levels or deuteron beam current. While we initially saw a significant contribution stemming from ^{6}He β particles penetrating through the thin-walled stainless steel bellows of our roughing pump, we were able to greatly reduce that background by shielding the bellows with lead. The data taken before this change were not included in the analysis. The measured background rate in background runs and the fitted background rate in half-life data taking runs are shown in Figure 3.16. The average background rate of the data taking runs was 0.8 ± 0.1 Hz, which is consistent with the average of the rates of the background runs. Combining all the background run data after shielding the bellows, we still observed a small decay structure with a half-life of 507(27) ms and an amplitude of 6.3(3) times the value of the constant background in the background runs. Although this is most probably still coming from ^{6}He that is being pumped away, it could also be the result of some beam-related activation. Regardless of its origin, we studied this time-dependent background by including it in the fitting function

$$R(t) = N(\exp[-(t-t_0)/\tau] + b(1 + A\exp[-(t-t_0)/\tau_b])) \tag{3.8}$$

where A is the ratio of the amplitude of the extra decay structure and the background and τ_b is the lifetime of the extra decay structure. We assumed that A was the same in the half-life data taking runs as that in the background runs. By varying A and τ_b in the range measured in the background runs, we concluded that the extra decay structure results in a systematic shift of 0.046 ms with an uncertainty of 0.004 ms.

3.7.6 Data-correction

We studied our data-correction procedure outlined in Section 3.6 in detail using the simulation with the occurrences of the different defects determined from the data. We did not observe any significant shift within the statistical uncertainty of the simulation. We also performed our fits on the data without any data corrections, resulting in a consistent value. We thus attribute a systematic uncertainty of 0.01 ms (the statistical uncertainty of our simulation) to our data-correction procedure.

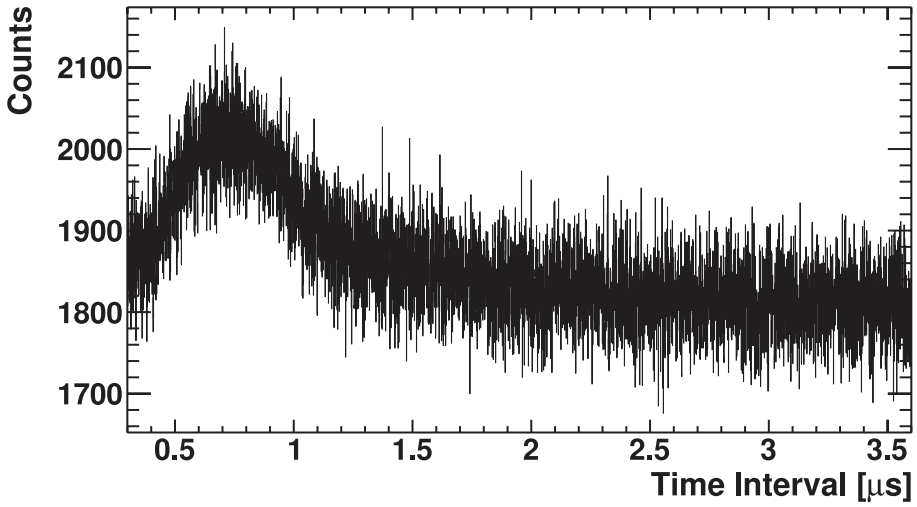

Figure 3.17: Histogram of the time between two events as measured with a time-to-amplitude converter in the range 0-4 μs. We see a clear indication of spurious afterpulses at 0.75 μs.

3.7.7 Spurious Afterpulsing

In a dedicated effort we measured the time distribution between two consecutive coincidence events using a time-to-amplitude converter (TAC) to search for spurious afterpulses owing to electronic or instrumental effects. We found an excess of events

Table 3.6: Obtained ^{6}He half-life values in our afterpulse simulation. The differences and corresponding uncertainties are with respect to the 8 μs channel.

Channel	Fitted half-life [ms]	Diff. [ms]	σ_{corr} [ms]
$\sim$2 μs	806.99984 ± 0.00957	0.0078	0.0020
$\sim$4 μs	806.99348 ± 0.00964	0.0014	0.0016
$\sim$6 μs	806.99331 ± 0.00971	0.0012	0.0011
$\sim$8 μs	806.99209 ± 0.00977		

in the 4 μs full range setting leading to a 0.7 μs-wide peak at 0.75 μs sitting on top of an otherwise perfectly exponential behavior [80] shown in Figure 3.17. The probability of occurrence of those excess events is 3×10^{-4}. Although those excess events are suppressed by the dead times, we performed a simulation with such an excess centered at 3.5 μs to study its potential influence. Table 3.6 lists the results of that simulation with the differences and associated uncertainty calculated as in the discussion on dead time above. There is a small effect visible in the 2 μs channel. As a conservative estimate of the systematic uncertainty, we use the statistical uncertainty of the simulation of 0.01 ms. The afterpulse height is about four times the noise amplitude in Figure 3.17, so the systematic uncertainty for a frequency of occurrence at the detection limit in the spectrum is 0.003 ms.

3.7.8 Other Systematic Considerations

We measured the precision of our 1 kHz clock by comparing the summed number of ticks over 16 days with respect to the time provided via an internet time server of NIST[1] [86]. The accumulated difference amounts to -11 ± 1 s over a period of 1.37×10^6 s, which corresponds to a shift of -8.03 ± 0.73 ppm. Owing to potential

[1]National Institute of Standards and Technology

changes in temperature, we assign an additional 13 ppm to the frequency uncertainty. Therefore, we estimated the systematic shift and uncertainty to be 0.006 ± 0.011 ms.

Pile-up effects do not play a significant role in our measurement because of our long dead times and low threshold. One way that pile-up would influence our result is if two coinciding pulses below threshold result in a pulse above threshold. As given in Section 3.2, the threshold cuts away $\sim$1% of the electron spectrum in each scintillator. The probability of two pulses of length $\tau_p \approx 100$ ns coinciding at a given rate R is given by $R\tau_p$. The probability that those two pulses are below threshold is $P_{\text{pile}} = 10^{-4}$. The correction that would need to be applied to the data thus takes the form $R_0 = R(1 - P_{\text{pile}} R\tau_p)$ in order to obtain the true rate R_0 given the measured rate R. Combined with the dead-time correction, the final correction (neglecting higher-order infinitesimals) looks like $R_0 \approx R/[1 - R(\tau_d - P_{\text{pile}}\tau_p)]$. Therefore, this pile-up effect behaves like a ~ 0.01 ns correction to the dead time, which leads to a negligible shift in our half-life value of 5×10^{-5} ms.

Another effect of pile-up would stem from the coincidence of two pulses directly at the end of the long dead-time gate, which would thus not free the trigger at the appropriate time and would extend the dead time. However, this requires the coincidence of three pulses, the probability of which is given by $(R\tau_p)^2$ corresponding to $\sim 10^{-5}$ at our highest rates. At the highest rates this leads to an extension of the dead time by a negligible 0.001 ns. Owing to both effects being negligible we do not list them in Table 3.4.

3.8 Results

Because the result of our measurements with the stainless steel insert is dominated by the systematic uncertainty owing to a potential diffusion of the ^{6}He atoms into the surface we do not average the two values given in Table 3.3. We report the data from

our measurements without the insert as our final result, yielding a ^{6}He half-life of

$$T_{1/2} = 806.89 \pm 0.11_{\text{stat}}\ ^{+0.23}_{-0.19}\ _{\text{syst}}\ \text{ms} \tag{3.9}$$

where the first error is statistical and the second systematic. From this, we proceed to determine the ft value for the β decay of ^{6}He and extract the corresponding Gamow-Teller matrix element. We calculated the Q value of the decay to be 3.505208(53) MeV/c^2 using the recent ^{6}He mass determination obtained in a Penning trap [87] and the value for ^{6}Li [88]. This corresponds to a 4σ shift compared to previously reported values [89]. The relation between the ft value and the Gamow-Teller matrix element M_{GT} is

$$f^\star t(1+\delta'_R)(1+\delta_{\text{NS}}-\delta_C) = \frac{K}{G_V^2(1+\Delta_R^V)\text{g}_A^2|M_{\text{GT}}|^2} \tag{3.10}$$

where $K = 2\pi^3\ \hbar^7\ c^6\ \ln 2/(m_e c^2)^5$, G_V is the vector coupling constant for semileptonic weak interactions, Δ_R^V is the transition-independent part of the radiative correction, δ_{NS} and δ'_R are transition-dependent parts of the radiative correction, and δ_C is the isospin symmetry-breaking correction, following the definitions and notation of Ref. [15]. We set the parameters δ_{NS} and δ_C to zero - or equivalently absorb them into the definition of M_{GT} - and calculated the radiative correction δ'_R to be 1.0365(13)%. We adopted the value for the parameters $K/[G_V^2(1+\Delta_R^V)] = 6143.62 \pm 1.66$ s from the world average of superallowed $0^+ \to 0^+$ nuclear β decays [15]. The statistical rate function is given by $f^\star = \int F(Z,E)pE(E-E_0)^2 f_1(E)dE = f(1+\delta_s)$, where f is the value of the integral in the absence of the shape-correction function $f_1(E)$ and δ_s is the correction to it when including $f_1(E)$. Here $F(Z,E)$ is the Fermi function, p and E the electron momentum and energy, and E_0 the end-point energy. We obtain $f = 995.224(68)$ yielding an ft value of $803.04^{+0.26}_{-0.23}$ s, where we added the statistical and systematic errors in quadrature. To take into account the shape correction, we performed shell-model calculations using the Cohen-Kurath interaction [90] and with the Warburton-Brown interaction, denoted PWBT in Ref. [91], adjusted to reproduce

either the experimental Gamow-Teller matrix element or the weak magnetism term, which in Holstein's notation [92] is $b = 68.4(7)$, determined from the width of the $0^+ \rightarrow 1^+$ transition in ^{6}Li [93]. Both adjustments result in almost identical terms for the statistical rate function and we obtain $f^\star = 997.12(58)$. From this we calculate the experimental value for the Gamow-Teller matrix element in ^{6}He β decay as $|M_{\rm GT}| = 2.7491(10)/|{\rm g}_A|$. Using ${\rm g}_A = -1.2701(25)$ [37] determined from the decay of the free neutron, we get $|M_{\rm GT}| = 2.1645(43)$.

3.9 Conclusions and Summary

We measured the ^{6}He half-life to be $806.89 \pm 0.11_{\rm stat}\ ^{+0.23}_{-0.19\ \rm syst}$ ms, thereby improving the precision over the currently reported value [56] by a factor of 6. Our result is in good agreement with two of the most recent five values [61, 57] with precisions of less than 1% but deviates from the three others by up to 8.6σ [60, 62, 59]. Because the possibility of diffusion out of the target was not directly addressed in these experiments we speculate that this may be the cause of the discrepancy, as diffusion would lead to shorter measured lifetimes, and that is what was observed. Calculating the statistical rate function we determined the ft value to be $803.04^{+0.26}_{-0.23}$ s. The extracted Gamow-Teller matrix element of $|M_{\rm GT}| = 2.1645(43)$ agrees within the error estimates of *ab initio* calculations using the weak axial coupling constant ${\rm g}_A$ measured in free neutron decay. Our precise determination allows for improved comparisons between theory and experiment and may allow using ^{6}He in addition to ^{3}H to fix low-energy constants in the effective-field-theory description of the electroweak processes.

Chapter 4

The Trap and Laser System for the $a_{\beta\nu}$ Experiment

Precision β-decay correlation experiments such as ours benefit greatly from using trapped radioactive atoms, such as in ion or laser traps. Scattering from nearby materials is minimized and thus the decay emissions can travel nearly unperturbed to their final detectors. Magneto-optical traps (MOTs) are isotopically selective and residual gases are pumped away freely to reduce contaminant backgrounds. Through the use of PMTs, photodetectors, and charge-coupled device (CCD) cameras the atomic cloud can be directly imaged for size, shape, and position monitoring via fluorescence detection to control for systematic effects. Additionally, the <1 mm trap size and <300 μK trap temperature reduce systematic uncertainties in the initial position and momentum of the decay products. MOTs in particular are very robust against fluctuations in alignment. For these reasons, MOTs are ideally suited as tools for studying the $a_{\beta\nu}$ angular correlations in $\beta-$decay. The MOT is the most frequently used neutral atom trap and the principles behind its operation have been described in great detail elsewhere [94][95], so I will not discuss it in this chapter. Instead I will discuss the details specific to our double-MOT setup and how we operate the traps with our 1083 nm trapping and 706 nm probing laser light.

4.1 Producing metastable ^{6}He atoms

The atomic structure of ^{6}He and ^{4}He are very similar, with only small isotopic shifts for each level ($\sim$ 35 GHz for the 2^3S_1-2^3P_2 trapping transition). Unlike other atomic species frequently used in MOTs, such as rubidium or cesium, cycling transitions from the ground state in helium such as the 1^1S_0-1^1P_1 transition would require a continuous wave vacuum ultraviolet (VUV) laser which is not commercially available. Instead we use the fact that the 1^1S_0-2^3S_1 transition is doubly forbidden; the selection rules for an E1 dipole transition require a change of angular momentum of $\hbar$ which is not present for an S-S transition, and the spin configuration of the electron must flip to account for the $2S_i + 1 = 1$ to $2S_f + 1 = 3$ change. Atoms which have been populated in the 2^3S_1 state are therefore metastable and will linger for a sufficient length of time for our purposes (7870 seconds [96]) before decaying to the ground state via an M1 dipole transition, unless quenched due to wall collisions or background gases. We therefore use the closed 2^3S_1-2^3P_2 transition at 1083 nm (see Figure 4.1), for which both laser diodes and high power (multi Watt) fiber amplifiers are commercially available.

While other groups have shown more efficient methods (10^{-4} vs. 10^{-5}) of populating the metastable state of ^{4}He using a DC discharge [97], the short lifetime of ^{6}He is incompatible with the conductance limitations of the DC discharge. Instead we use the method of a low pressure ($\sim$few mTorr), large conductance radio frequency (RF) discharge [98] to ionize gas passing through a ceramic tube. The free electrons are sloshed around by the RF field and collide with neutral helium, exciting the atoms to various atomic states. Most of these excited states will relax back to the ground state, but $\sim 10^{-5}$ will end up in the metastable state under good conditions. Carrier gases which are more easily ionized, such as krypton and xenon, are mixed in with the helium to provide additional electrons for collisions. There is a delicate balance that must be maintained with regards to the carrier gas pressures: too little gas diminishes the electron-helium collisional frequency, while too much gas increases the chance of

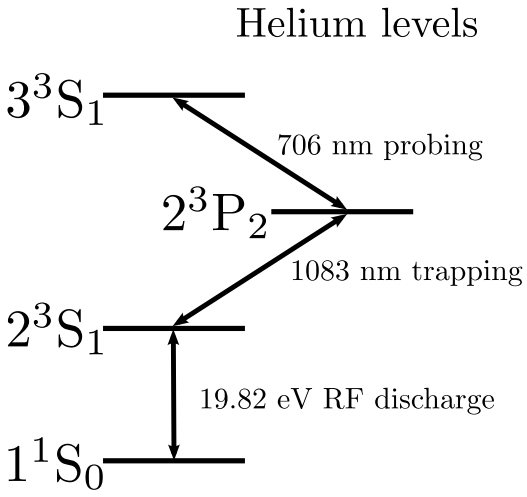

Figure 4.1: Shown are the relevant atomic levels for helium after excitation from the ground state.

collisions with a metastable helium atom which will quench the atom back down to the ground state. Leak valves are carefully tuned to maximize the metastable fraction as measured by fluorescence detection downstream. In the discharge tube, typical total pressures of ∼3 mTorr are used, with a ∼10:1 ratio of Xe to ^{4}He. The produced ^{6}He is mixed into this stream just before entering the discharge chamber. The exact gas mixture is not constant, in general, and is tuned daily. The RF resonator consists of a quarter-wave coil inside a resonating copper can (see Figure 4.2). RF power is sent to the coil at $\sim 30 - 50$ W at the 214.5 MHz[1] third harmonic of the RF resonator, yielding a 50% improvement in the metastable fraction over operating at the fundamental frequency. Just before the RF resonator is a liquid nitrogen (LN_2) reservoir that is gravity fed from an external dewar. The cold reservoir is in thermal contact with the ceramic tube and serves to slow down the initially thermalized helium from speeds of ≈ 1200 m/s to ≈ 500 m/s before entering the Zeeman slower and enhances

[1]In general, the resonant frequency and its harmonics depends on the properties of the RF coils which have been swapped out from time to time.

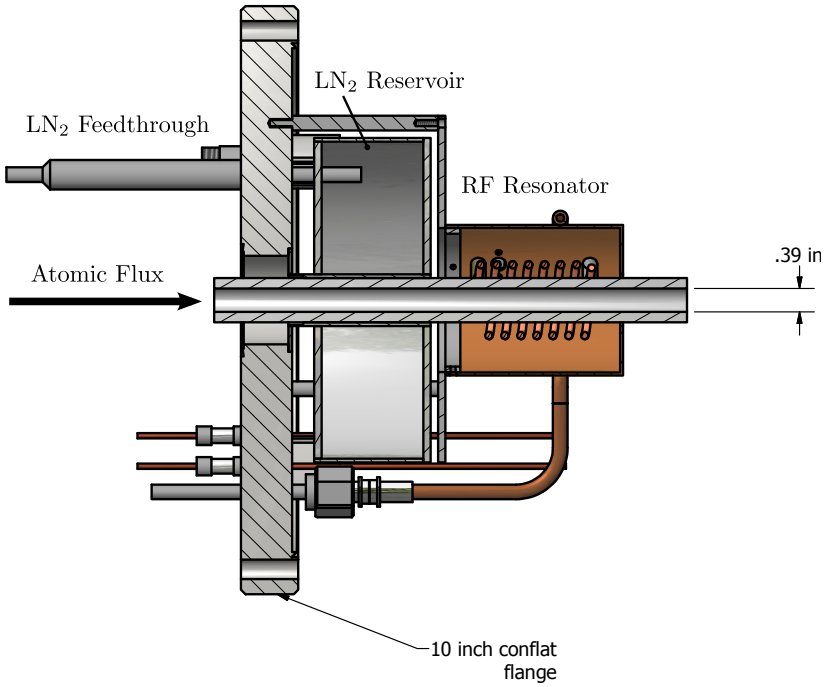

Figure 4.2: Schematic of the RF discharge assembly used in the experiment.

the capture efficiency of the MOT by a factor of 3-4.

4.2 Transverse cooling

Because the vast majority of the atoms coming out of the discharge tube are in the ground state and would wind up downstream in the MOT chamber, limiting our trap lifetime due to collisions and potentially creating excessive background decays, an aperture is placed just before the Zeeman slower to reduce the solid angle seen by the emerging atoms. The atoms emerge from the ceramic tube with a large emittance angle. Those atoms which emerge outside of the solid angle subtended by the aperture are pumped away by two or more turbo-molecular pumps (150 L/s - 250 L/s) and are either exhausted or recirculated. To enhance transmission for the metastable atoms, and to increase the density of atoms which fall within the solid angle of capture

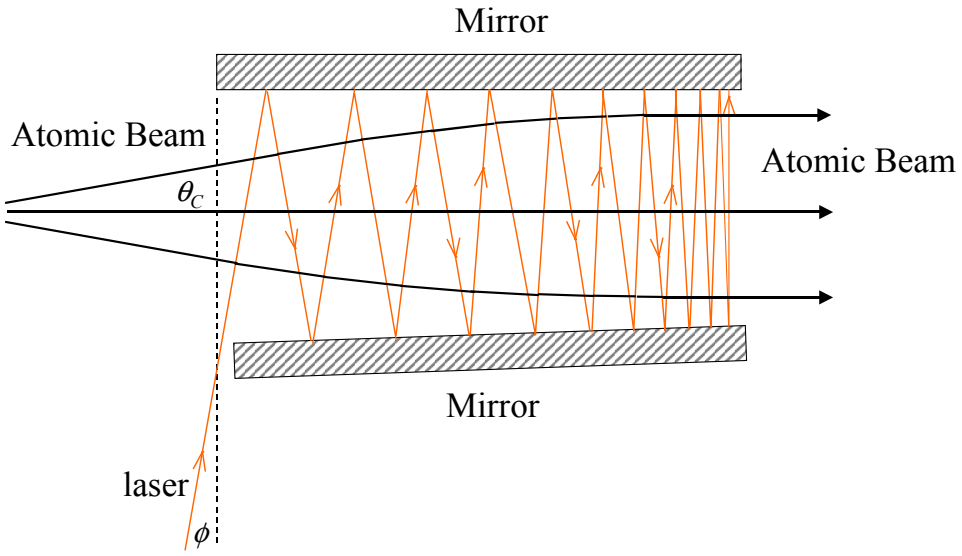

Figure 4.3: Schematic drawing of one pair of transverse cooling mirrors along with the zigzag pattern of laser light. The mirrors are aligned such that the incident laser light is constantly perpendicular to the atomic beam. Reproduced from Libang Wang's thesis [99].

of the MOT, we use two orthogonal pairs of 20 cm long mirrors with a reflective dielectric coating for 1083 nm light and laser light on resonance to within ± 1 MHz to provide a two dimensional optical molasses for collimating the metastable atoms. Figure 4.3 shows a schematic drawing in two dimensions of how these mirrors are aligned relative to the atomic beam and transverse cooling light. One mirror from each pair is mounted inside the transverse cooling chamber which are connected to rotatable feedthroughs for fine angular adjustments. On the outside, the respective partners are angled in such a way as to make multiple light passes along the length of the mirror. If properly aligned, transverse cooling can enhance the MOT capture efficiency by a factor between 80 and 100.

4.3 Recirculation

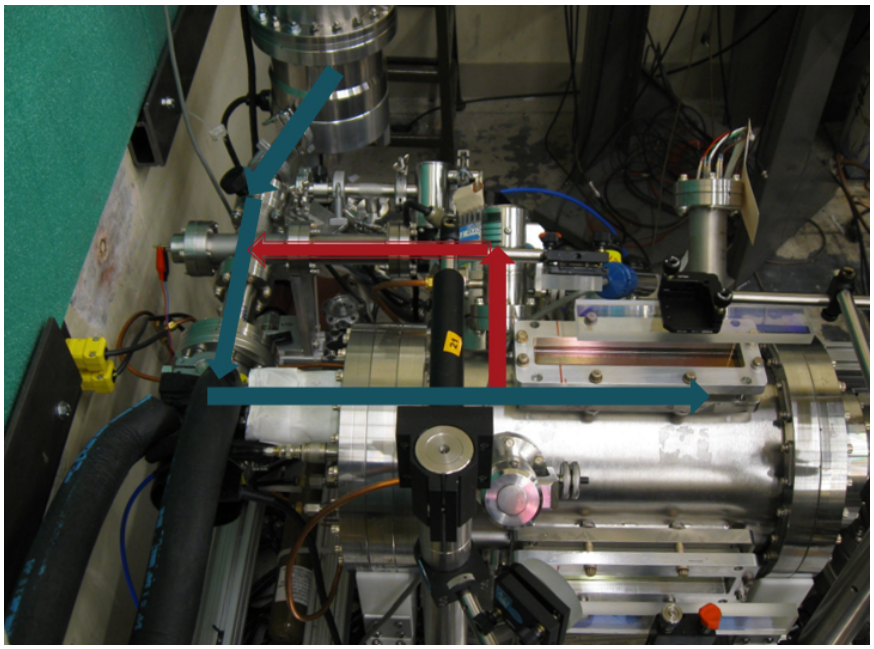

Figure 4.4: The blue arrows indicate the flow of ^{6}He from the exhaust of the first TMP to the discharge source and onto the Zeeman slower. The red arrows indicate flow of ground state ^{6}He as they are pumped by the second TMP back around to the discharge source.

We occasionally use, and after improvements will permanently use, a recirculation scheme to recover the atoms which have not been excited to the metastable state rather than letting them be pumped away as exhaust. Because ^{6}He has a half-life of ∼807 ms (see Chapter 3) the ^{6}He can be repumped back to the inlet of the RF discharge source for additional attempts at populating the metastable state before decaying. Conductance considerations implied that this would enhance the total fraction of ^{6}He atoms which eventually become trapped by a factor of 4.5. However, operating under these conditions has thus far made the plasma conditions in the RF discharge somewhat unstable. All the gases, including xenon and krypton, are

recirculated along with the helium. The xenon tends to freeze out on the cold surfaces of the LN_2 reservoir (see Figure 4.2) when it recirculates and this can change the discharge conditions over time. A redesign of the discharge source with the ability to regulate the temperature of the reservoir is presently underway and is expected to alleviate this problem.

4.4 Zeeman Slower

The capture velocity of our trap is ∼10 m/s, compared with the most probable[2] speed for ^{6}He exiting the LN_2-cooled discharge tube of ∼500 m/s. It is clear that without first slowing down the atoms, our MOT would only capture a small fraction of the velocity distribution, about 5×10^{-6}. To slow down the atoms we use the Zeeman slowing technique [100] wherein laser light opposes the direction of the atomic beam to decelerate the atoms before capture. We use a 1.8 m Zeeman slower from previous efforts to measure the charge radii of ^{6}He and ^{8}He [36][101].

The Zeeman slowing technique relies on the principle of resonant light scattering. Only near resonant photons in the frame of the atom will be scattered. However, after only a few absorption and emission cycles the Doppler shift due to the now reduced atomic velocity is such that the atom is no longer in resonance with the laser light and effective slowing rapidly diminishes. To compensate for this effect, the magnetic field of the slower is designed such that the Zeeman shift in the atomic level accounts for the changing Doppler shift along the axis of the beam line. This requires a difference in the magnetic moments of the initial and final atomic states. For the case of ^{6}He we use circularly polarized 1083 nm trapping light to optically pump the atoms to cycle between the $2^3S_{1,m_J=1} - 2^3P_{2,m_J=2}$ states (see Figure 4.5).

---

[2]For a Maxwell-Boltzmann distribution, $v_p = \sqrt{\frac{2k_BT}{m_{He}}}$

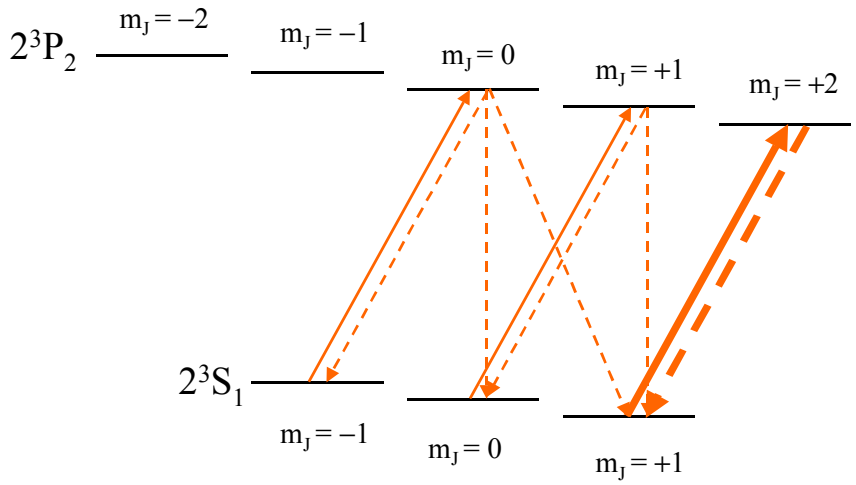

Figure 4.5: Optical pumping and cycling used for slowing the atoms before MOT capture. Splitting in the atomic sublevels is caused by the Zeeman effect from the solenoid magnetic field. Reproduced from Libang Wang's thesis [99].

4.5 2D Focusing

As the atoms travel along the Zeeman slower, they are cooled axially, but heated radially due to the random direction of spontaneous emission. This causes the atoms to begin to diverge from collimation as they are slowed. The atomic beam can be focused transversely using the same principles that make a MOT operate [94][95], but in two dimensions instead of three. Red-detuned, circularly polarized light forms an optical molasses in the transverse direction of the atomic beam's motion while a quadrupole magnetic field defines an axis aligned with the atomic beam axis. The laser beams selectively scatter from atoms which are furthest from this axis, forcing the atoms inward and focusing the atomic beam at the center of the atomic trap downstream. Placing the 2D focusing region in the middle of the Zeeman slower provides a factor of two enhancement in the final trapping efficiency by increasing the overlap of the atoms with the final trapping laser beams. Figure 4.6 shows our 2D

focusing setup with the direction of the laser beams overlaid.

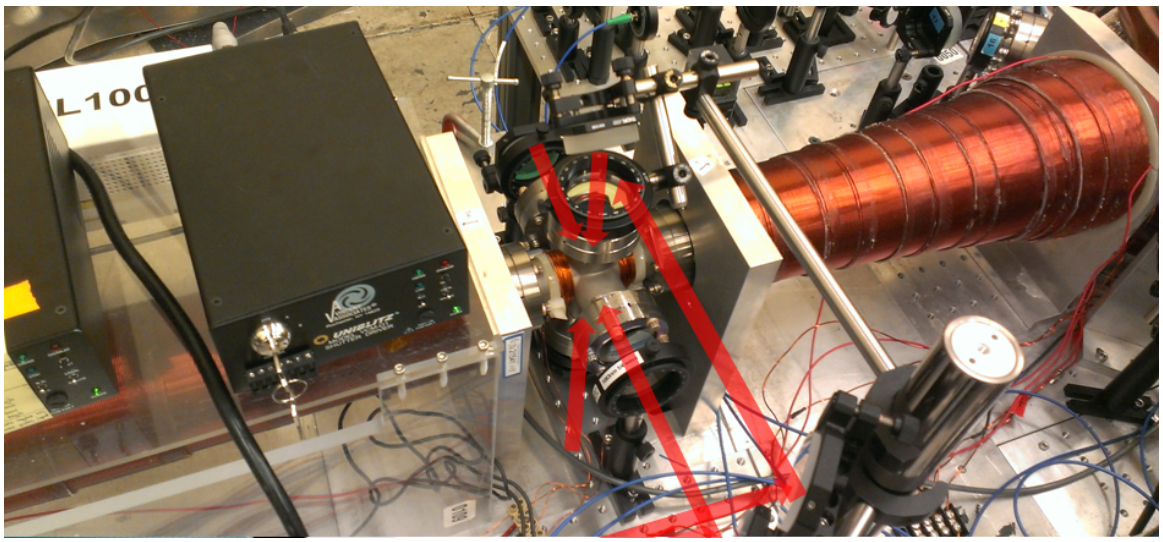

Figure 4.6: 2D focusing stage in between two sections of the Zeeman slower. By selecting circular polarizations appropriate for the direction of the magnetic field in both dimensions, the atoms which pass through this stage will be focused inward and the final trapping efficiency can be enhanced by a factor of $1.5 - 2$.

4.6 Using a Double-MOT

Because we are interested in maximizing statistics while minimizing radioactive backgrounds due to untrapped atoms, we make use of a double-MOT setup, capturing in the first MOT chamber (MOT1) and transferring to the second MOT chamber (MOT2) for final beta decay detection.

Figure 4.7 shows a vertical cross-section of our two traps. The atomic beam is directed into the page and overlaps with MOT1 where 1083 nm lasers cool and trap the atoms. A pulsed push beam is used to transfer atoms over to MOT2 for final trapping and detection. A transverse cooling stage separates the two MOT chambers

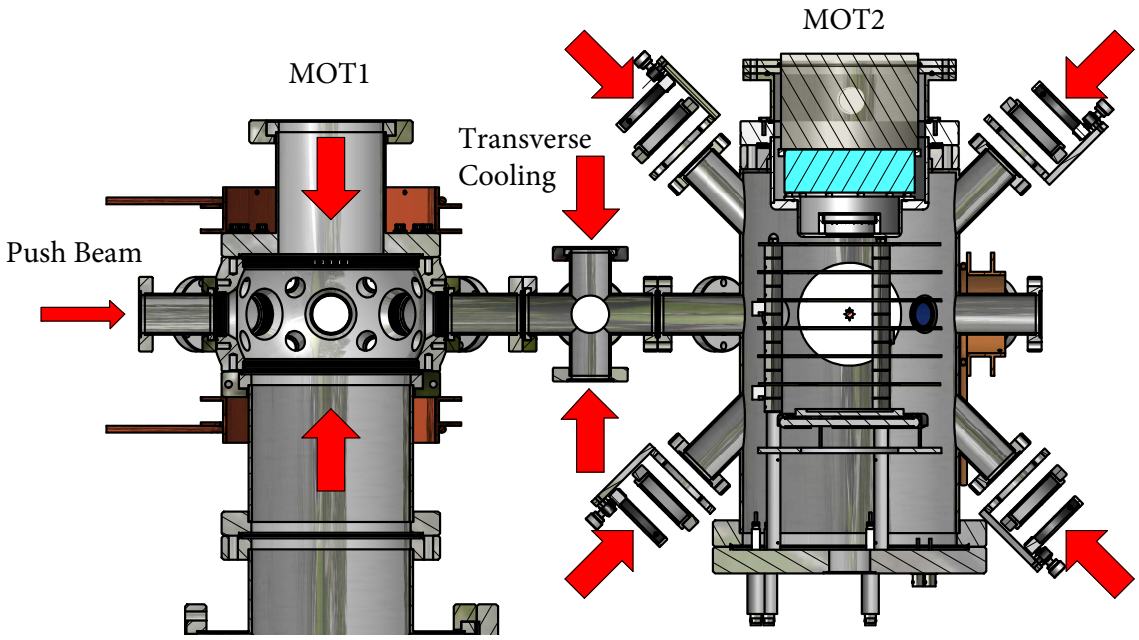

Figure 4.7: Cross-section view of our double-MOT setup.

and serves to cool the expanding atoms during the transfer flight to maximize the capture efficiency of MOT2.

4.6.1 MOT1

Our first trap is optimized for loading rate and efficient transfer into the second trap. To do this, we operate MOT1 in two modes: Capture Mode and Cooling Mode. While the atoms are being loaded into the trap, the lasers are more significantly red-detuned to capture a wider class of incoming velocities. The laser also operates at a large intensity in Capture Mode to compensate for the fact that the larger detuning makes for a shallower trap depth. Once the atoms have been loaded into the trap, the laser conditions change to Cooling Mode. Here the laser frequency is brought much closer to resonance while the laser power is simultaneously reduced to prevent excessive heating. Because the lasers in Cooling Mode are tuned closer

Laser Conditions	Capture Mode	Cooling Mode
1083 nm MOT1 Intensity	50 I_s	2 I_s
1083 nm MOT1 Detuning	-13 MHz	$-2-3$ MHz
1083 nm MOT2 Intensity	50 I_s	2 I_s
1083 nm MOT2 Detuning	-12.5 MHz	$-2-3$ MHz
Zeeman Slower Intensity		$10-20$ I_s
Zeeman Slower Detuning		-370 MHz
Transverse Cooling Intensity		$200-300$ I_s
Transverse Cooling Detuning		0 MHz
2D Focusing Intensity		2 I_s
2D Focusing Detuning		-4.5 MHz

Table 4.1: List of laser settings used for loading and cooling MOT1. Intensities are listed in terms of the saturation intensity per beam of the transition, $I_s = \pi hc\Gamma/3\lambda^3 \approx 0.16$ mW/cm^3.

to resonance, the scattering rate at the same intensity would increase by a factor of $\sim$5 when compared to the detuning in Capture Mode. The intensity is brought down such that the overall scattering rate decreases by about half, cooling the atoms from several hundred microKelvin with a spatial extent of a few millimeters down to approximately 100 μK with a spatial extent of approximately 500 μm. A complete list of experimental values used for each mode is given in Table 4.1.

4.6.2 Transferring atoms to MOT2

Not all of the helium atoms that find their way into the MOT1 chamber will be metastable atoms. Since the fraction of metastable atoms is only 1×10^{-5} at best, and since untrapped atoms can continue to bounce off the walls towards the MOT

chamber, the vast majority of the atoms in the chamber will be ground state helium. A 250 L/s turbo-molecular pump mounted to the bottom of the MOT1 chamber will pump these untrapped atoms away, but some of these atoms will decay before this happens, presenting a false signature for our detectors. To combat this, we use a second MOT chamber and transfer only the trapped atoms from MOT1 to MOT2. A 10 mm diameter, 100 mm long aperture tube separates the two chambers, providing a large impedance for untrapped atoms to diffuse from the MOT1 chamber to the MOT2 chamber. In addition, a fast shutter is mounted in the MOT1 chamber at the entrance to the aperture tube and is opened only when atoms are actively being transferred between traps to further minimize untrapped atoms from moving into the MOT2 chamber.

To transfer the atoms from MOT1 to MOT2, we make use of a pulsed 1083 nm push beam aligned with the centers of both traps. Timing is critical here. We first change the conditions in MOT1 from the Capture Mode to the Cooling Mode to condense and cool the atoms for $\sim$3 ms to minimize the ballistic expansion of the atoms during the flight from MOT1 to MOT2. Then we turn off all trapping/cooling light in MOT1 and immediately pulse the push beam for $\sim$400 μs to kick the atoms over to the second trap, which takes about 15 ms. At approximately the same time we open up the shutter in front of the aperture tube for $\sim$20 ms to allow the atoms to pass through without obstruction. In preparation for the incoming atoms, the trapping light in MOT2 is switched from Cooling/Data Taking Mode, where the previous bunch of atoms has been held, to Capture Mode. Once all the atoms from MOT1 have been captured, MOT2 switches back into Cooling/Data Taking Mode for beta decay detection. Transfer efficiencies up to 30% have been achieved by optimizing the timing and power for each set of lasers. The order and duration of timing can be seen in Figure 4.8.

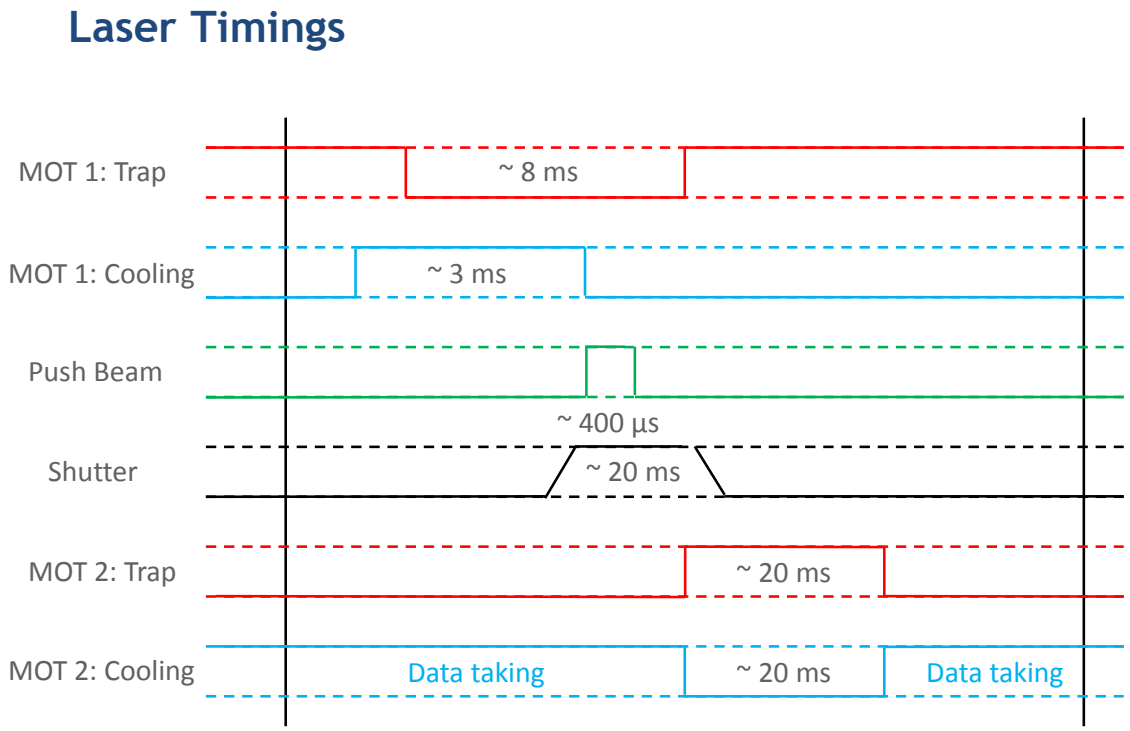

Figure 4.8: Laser timing and duration is critical when maximizing the transfer efficiency from MOT1 to MOT2. Efficiencies up to 30% have been achieved with careful tuning. Timings not shown to scale.

4.7 Measuring the trapping efficiency

To calculate the trapping efficiency for MOT1, we must look at the loading rate of the trap compared with the overall gas consumption rate. To measure the loading rate, we must consider how the number of atoms in the trap changes with time. We fit the trap number during loading to a $N(1 - e^{-t/\tau})$ function to find the time constant, τ. The loading rate is then $L = N/\tau$, where N is the atom number.

We measure the atom number by measuring the fluorescence of the trap due to the 1083 nm trapping lasers or alternatively from a 706 nm probing laser (see Section 4.9).

The atoms scatter photons from these lasers into a photodetector which outputs a current proportional to the scattering rate of the atoms. This current is amplified and finally converted into a voltage signal for final reading. The scattering rate of the atom depends on the laser intensity and detuning from the excitation resonance frequency, as well as the natural linewidth of the transition, which is 1.6 MHz for the $2^3S_1 - 2^3P_2$ transition in helium, and can be calculated with the following equation [94]:

$$\Gamma_{scat} = \frac{\Gamma}{2} \frac{s}{1 + s + (2\delta/\Gamma)^2} \tag{4.1}$$

Here, Γ is the natural linewidth of the transition in units of angular frequency ($2\pi \times 1/s$), δ is the laser frequency detuning from the resonance, also in units of angular frequency, and s is a unitless intensity parameter given as the ratio of the laser intensity to the saturation intensity of the transition, I/I_s where $I_s = \pi hc\Gamma/3\lambda^3 \approx 0.16$ mW/cm^3 [94].

The final atom number N is then the voltage output of the amplifier divided by the product of the scattering rate, the energy per photon, the solid angle of the detector, the quantum efficiency and responsivity (in A/W) of the detector, and finally the gain from the current-to-voltage amplifier.

$$N_{atoms} = V_{amp} / \left[\Gamma_{scat} \times \frac{hc}{\lambda} \times \frac{\Omega}{4\pi} \times \epsilon \times Resp(A/W) \times Sens(V/nA) \right] \tag{4.2}$$

Here, Ω is the solid angle subtended by the internally mounted lens which collimates the photons onto the photodetector, ϵ is the quantum efficiency of the detector, $Resp$ is the responsivity of the detector, and $Sens$ is the sensitivity of the amplifier.

The ratio of the loading rate to our consumption rate is our trapping efficiency. The consumption rate is given directly by our ^{6}He production rate on the order of 10^{10} ^{6}He/s as described in Section 2.8. For loading rates in MOT1 between 2×10^2 ^{6}He/s and 1×10^3 ^{6}He/s, our capture efficiency is between 2×10^{-8} and 1×10^{-7}.

4.8 Measuring the lifetime of the trap

There are two primary loss factors in the trap. One is through collisions with background gases including hydrogen and others which can kick the helium atoms out of the shallow trap. Another is 2-body Penning ionization whereby two metastable helium atoms interact such that the energetic excited state is quenched, ionizing one or more of the atoms and losing both from the trap. It is clear that the first loss mechanism is a one-body process where the loss rate is dependent upon the number of atoms in the trap, whereas the 2-body process depends on the square of the number of atoms in the trap since two atoms must be present for the Penning ionization to occur. Therefore, 2-body Penning ionization is something that occurs only for rather large densities which are not present in trapping the relatively few ^{6}He atoms in our case. The only gain factor is due to atom loading. Then we can write generally the following:

$$\frac{dN}{dt} = L - N/\tau_1 - N^2/\tau_2 \tag{4.3}$$

Here, L is the loading rate, $1/\tau_1$ is a coefficient corresponding to background collisions, and $1/\tau_2$ is a coefficient corresponding to 2-body Penning ionization. If we ignore Penning ionization in the case of small atom numbers, then it is clear that measuring the lifetime of the trap yields τ_1. This can be achieved by turning off the Zeeman slowing light to stop loading the trap, or by using an actuated shutter in the beam line to interrupt the atomic beam. This loss rate is proportional to the collision rate with background gases and therefore to the background pressure. The lifetime of the trap is thus inversely proportional to the background pressure in the low-density regime where two-body Penning ionization is negligible. Because the helium atoms store $\sim$20 eV in the metastable state, the energy released during a collision can ionize the background gas. In the MOT2 chamber, we have a 1.55 kV/cm electric field for collecting our recoil lithium ions (see Section 5.4), as well as a microchannel

plate (MCP) which can detect ions (see Section 5.3). When ionized, the background gases are immediately accelerated towards the MCP and detected, and this detection rate is proportional to the collision rate and therefore the lifetime of the trap. For background pressures of 8.5×10^{-9} Torr in the second MOT chamber, we measured a trap lifetime of about 965 ms by fitting the ion detection rate on the MCP as a function of time to an exponential (see Figure 4.9).

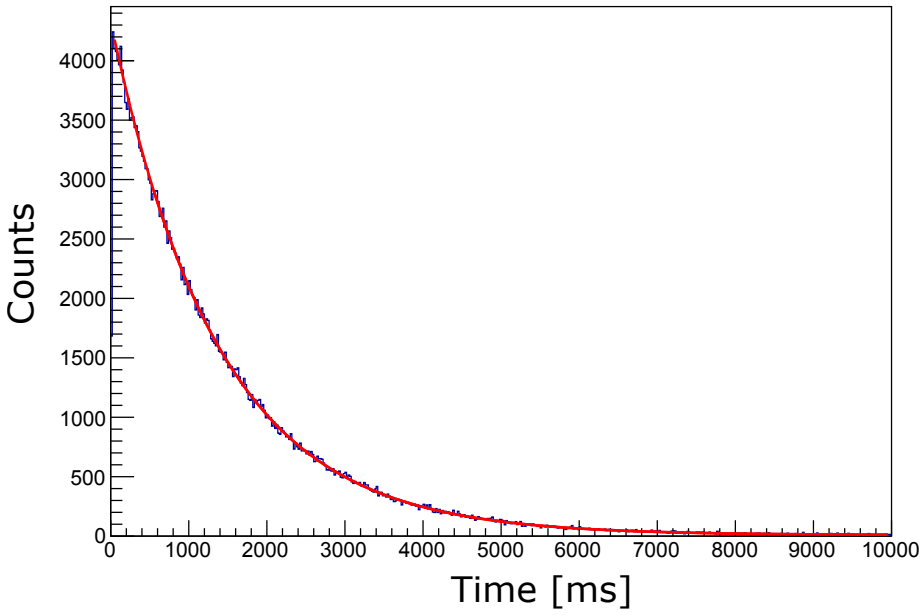

Figure 4.9: The number of detected ions on the MCP is recorded as a function of the time after the MOT2 trap is loaded.

4.9 706 nm probing

In addition to the 1083 nm transition used for trapping the helium atoms, we make use of the $2^3P_2 - 3^3S_1$ 706 nm transition (see Figure 4.1) for sensitively imaging and monitoring the atom cloud. The primary reason for this is that the sensitivity of CCD cameras and PMTs is much higher for 706 nm light than for the near infrared 1083 nm

light. A CCD camera is approximately 100 times less sensitive for 1083 nm light, whereas our PMT (Hamamatsu model H7421-50) is not sensitive at all at 1083 nm. We make use of an internal and external lens to enhance the solid angle when imaging the atom cloud onto the CCD or PMT. Additionally, long and short pass filters block out all light outside the range of 700 to 750 nm, which serves to block most of the background light from the room and all of the 1083 nm trapping light.

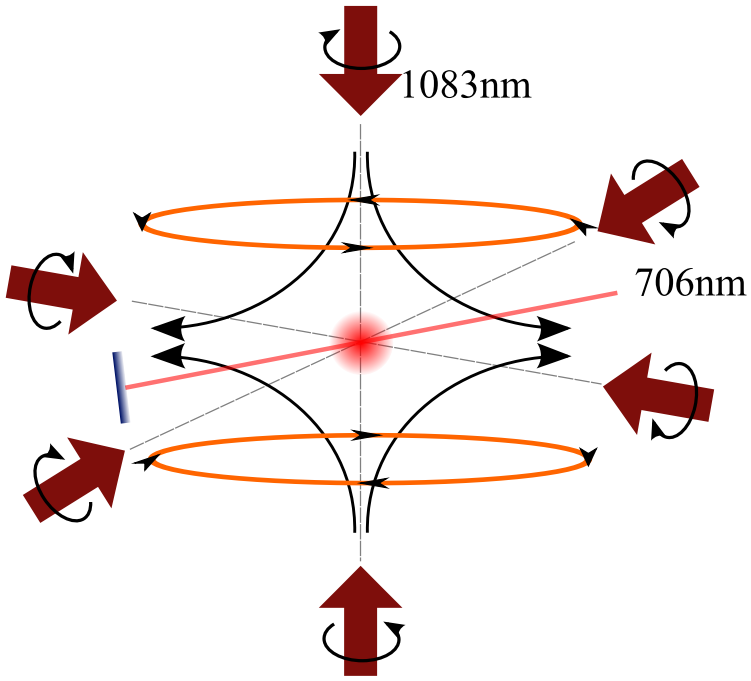

Figure 4.10: The 706 nm beam illuminates just the cloud of atoms and scatters photons into the camera or PMT which are much more sensitive at 706 nm than at 1083 nm.

4.10 Frequency control systems for the 1083 nm and 706 nm lasers

4.10.1 1083 nm lasers

Trapping the helium atoms requires that the 1083 nm trapping lasers remain locked at the resonant frequency of the atomic transition. Each stage of the slowing, transverse cooling, and trapping process demands its own frequency and power level to account for Doppler shifts. Splitting our laser beams between the various stages also requires substantial power. We use the method of a saturation absorption spectroscopy (SAS) [102] described in this section to lock a primary laser to the $2^3S_1 - 2^3P_2$ transition in a reference cell filled with ^{4}He gas. A secondary laser is beat locked to the first laser to account for the $\sim$35 GHz isotope shift between ^{4}He and ^{6}He. We then use a fiber amplifier to amplify the secondary laser to produce up to 10 W of laser power which is distributed to each of the trapping stages.

Our primary laser, DL1, is a Toptica Model DL-100 tunable laser which outputs up to 40 mW of 1083 nm laser light. Our secondary laser, DL2, is a home-made diode laser using a Toptica Model LD-1083-0075 laser diode which can output up to 40 mW of laser power. We use a 10 W fiber amplifier (Keopsys CYFA PB series) and couple one of the two diode lasers into the amplifier via a fiber switch so we can quickly switch between trapping ^{4}He and ^{6}He.

We lock our DL1 laser diode to the saturated absorption transmission peak of a probe beam through a reference cell of ^{4}He as read by the transmitted intensity on a photodetector. If laser light were to be scanned near resonance and passed through the reference cell and the relative absorption were monitored as a function of frequency, the absorption curve would be smeared due to Doppler broadening. To overcome this issue and lock the laser to the true resonance peak, we shine low-intensity probe light

through a reference cell and shine relatively high-intensity pump light (∼9 times more intensity) at the same frequency through the other side of the reference cell such that it is counter-propagating with the probe beam (see Figure 4.11). If the atoms inside the cell have a non-zero velocity along the axis of the overlapping laser beams, the resulting Doppler shift will cause the atom to absorb light preferentially from one laser or the other. However, the zero-velocity group will see both laser beams if the laser light is on resonance. The pump laser beam has sufficient intensity to saturate the transition and maximally populate the excited 2^3P_2 state. The probe beam, which is at the same frequency and can therefore talk to the atoms of the same velocity class, then causes stimulated emission. Since in the case of stimulated emission both photons are emitted in the same direction as from where the incident photon came, the absorption monitor will see a peak in the transmitted light at this frequency. This peak is much more narrow than the Doppler-broadened absorption curve.

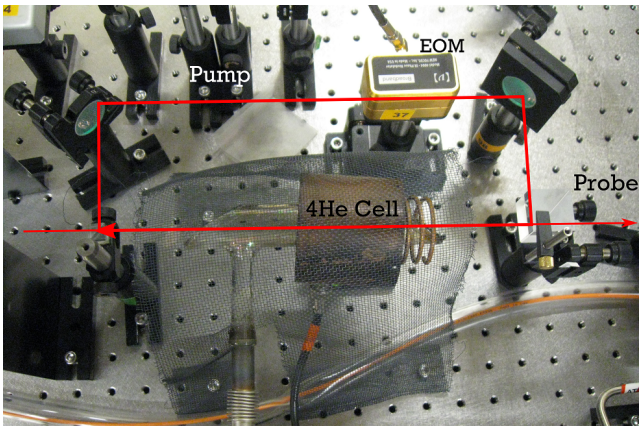

Figure 4.11: Setup for saturation spectroscopy of helium. Pictured is the EOM used for phase/frequency modulation of the pump beam, as well as the cell containing ^{4}He surrounded by an RF coil which causes the plasma discharge inside the cell to populate the 2^3S_1 state.

Frequency modulation of one of the lasers is directly converted into an amplitude

modulation in the transmitted light, as more or less light is absorbed depending on the instantaneous frequency of the laser light. Phase-sensitive detection performed at the same modulation frequency using an RF mixer then produces an error signal which serves as an input to a proportional/integral (PI) feedback unit to control the laser diode current (proportional/fast-feedback) or the diffraction grating position controlled by the voltage input on a ceramic piezoelectric actuator (integral/slow-feedback).

We use the technique of FM-modulation transfer spectroscopy described in Ref. [103]. Instead of modulating the probe beam we modulate the pump beam at $\sim$8 MHz using an electro-optical modulator (EOM) which uses the Pockels effect [104] to modulate the phase of light passing through it to produce frequency-shifted sidebands. If we had modulated the probe beam directly, the Doppler-broadened absorption curve would also be modulated and thus would be present in the error signal. By modulating the pump beam instead, the only amplitude modulation that takes place is that corresponding to the probe and pump beams interacting with the same atoms, so the resulting error signal is flat except near the resonant frequency (see Figure 4.12).

We lock our DL2 diode laser in reference to our DL1 laser using a beat lock [105]. Part of the laser light provided by DL2 is split off to pass through an EOM modulated at 16.760 GHz. This phase modulation produces frequency sidebands spaced relative to the carrier by the modulation frequency. We use the second-order negative sideband of the EOM which is therefore shifted -33.520 GHz relative to the output of DL2. This is roughly 1 GHz higher in frequency than DL1, and maintaining this frequency difference via the beat lock allows DL2 to be locked relative to DL1 such that when DL1 is locked to the $2^3S_1 - 2^3P_2$ transition for ^{4}He, DL2 is locked to the same transition for ^{6}He. These frequencies are well known to within 50 kHz from isotope shift measurements between ^{4}He and ^{6}He [36]. See Figure 4.13 for a simplified schematic drawing of the locking mechanisms for DL1 and DL2.

The fiber amplifier operates in constant-output mode, so the power level of the

amplifier is irrespective of the input power within the range of $0-3$ dBm, which allows us to switch the input frequencies via a fiber switch between the locked outputs of DL1 and DL2. The high-power (4-10 W) output beam of the fiber amplifier is then split into multiple beams which are then frequency shifted by acousto-optical modulators (AOMs or Bragg cells) for the various cooling, slowing, and trapping stages.

Acousto-optical modulators function by sending sound waves via a piezoelectric transducer through a transparent crystal. Light which passes through the crystal can experience Bragg diffraction caused by the resulting traveling wave of higher and lower refractive indices caused by the sound wave. Multiple scattering orders may be present, with the 0th order undisturbed, and the 1st diffraction order altered in both direction and frequency according to the wavenumber of the sound wave. About 75% of the incoming light can diffract to the 1st order if properly aligned.

Figure 4.14 shows a simplified schematic of how the fiber output beam is distributed and shifted by each AOM. Single pass AOMs are used for tuning the frequencies of the push beam, transverse cooling, Zeeman slowing, and 2D-focusing beams. Double-pass AOMs are used to control the frequencies of the MOT1 and MOT2 beams to allow these frequencies to be switched without having to realign the laser beam with its fiber coupler, as an AOM shifts both the direction and frequency of a laser beam which passes through it as a function of its input RF frequency.

Immediately prior to the reference cell for DL1 we also use a double-pass frequency shift via AOM to increase the light frequency going into the reference cell with respect to the output of DL1 by 90 MHz. This is a matter of practical convenience because our AOMs are unable to shift the frequency of the light in the range of $\sim 2-20$ MHz. By first shifting the frequency of DL1 by -90 MHz relative to resonance, we can use the various other AOMs to shift the frequency back up or further down to their respective targets and remain within the operating range of the AOMs.

4.10.2 706 nm laser

The 706 nm laser light is produced by a Toptica Model DL-100 tunable laser with an output power of ∼10 mW, which is sufficient for the purposes of probing and therefore requires no fiber amplification. Like the 1083 nm lasers, however, we must lock this laser to the resonant frequency of our atoms, now for the $2^3P_2 - 3^3S_1$ transition. We are fortunate in that the isotope shift between ^{4}He and ^{6}He for this transition is relatively small (606 MHz) and can be achieved by using a doubly-passed AOM operating at ∼300 MHz instead of by beat locking or some other method.

To lock the 706 nm laser, we use a similar method as discussed for DL1 by using a reference cell of ^{4}He with an RF driven discharge. However, the discharge in the reference cell does not populate the 2^3P_2 state sufficiently, and the cell is thus mostly transparent to 706 nm light. To populate this state more we must introduce some 1083 nm light. We want to lock our laser to the zero-velocity class atoms to be on resonance with our trapped cloud, as before. We benefit from the fact that we already have 1083 nm light from DL1 locked to the zero-velocity class atoms. This means that by overlapping locked 1083 nm light with 706 nm light, the 706 nm light will only be absorbed strongly when it is on resonance. Unlike our lock for DL1 we do not need a counter-propagating 706 nm pump beam as the zero-velocity locked 1083 nm light serves a similar function. We still must modulate the laser light for lock-in detection. This is done via diode current modulation at ∼20 kHz. Figure 4.15 shows a simplified version of the lock scheme used for our 706 nm laser. Since we frequently switch which isotope we are trapping we switch between using an AOM or not when illuminating ^{6}He or ^{4}He with 706 nm light, respectively.

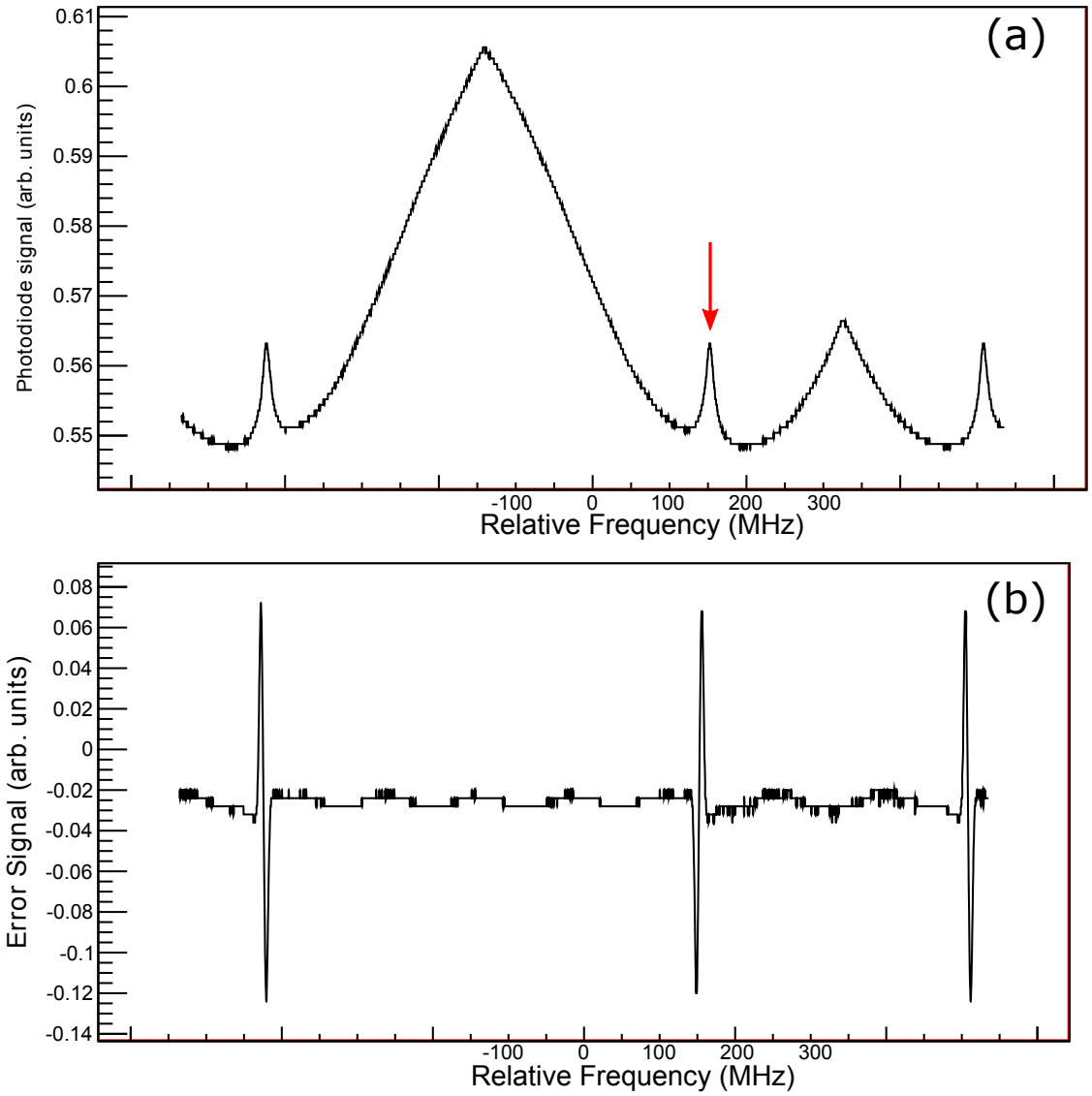

Figure 4.12: (a) (Binned) Saturation absorption photodiode signal from a ^{4}He cell. The peak in the Doppler-broadened absorption spectrum (shown with an arrow) corresponds to the $2^3S_1 - 2^3P_2$ transition. (b) Error signal produced by the RF frequency mixer. Artifacts in the plot are due to binning and are not present in the signal directly. Only the relative frequency range of the sweep is shown, as the sweeping signal is a triangle-wave and therefore only scans over a set frequency range before scanning back.

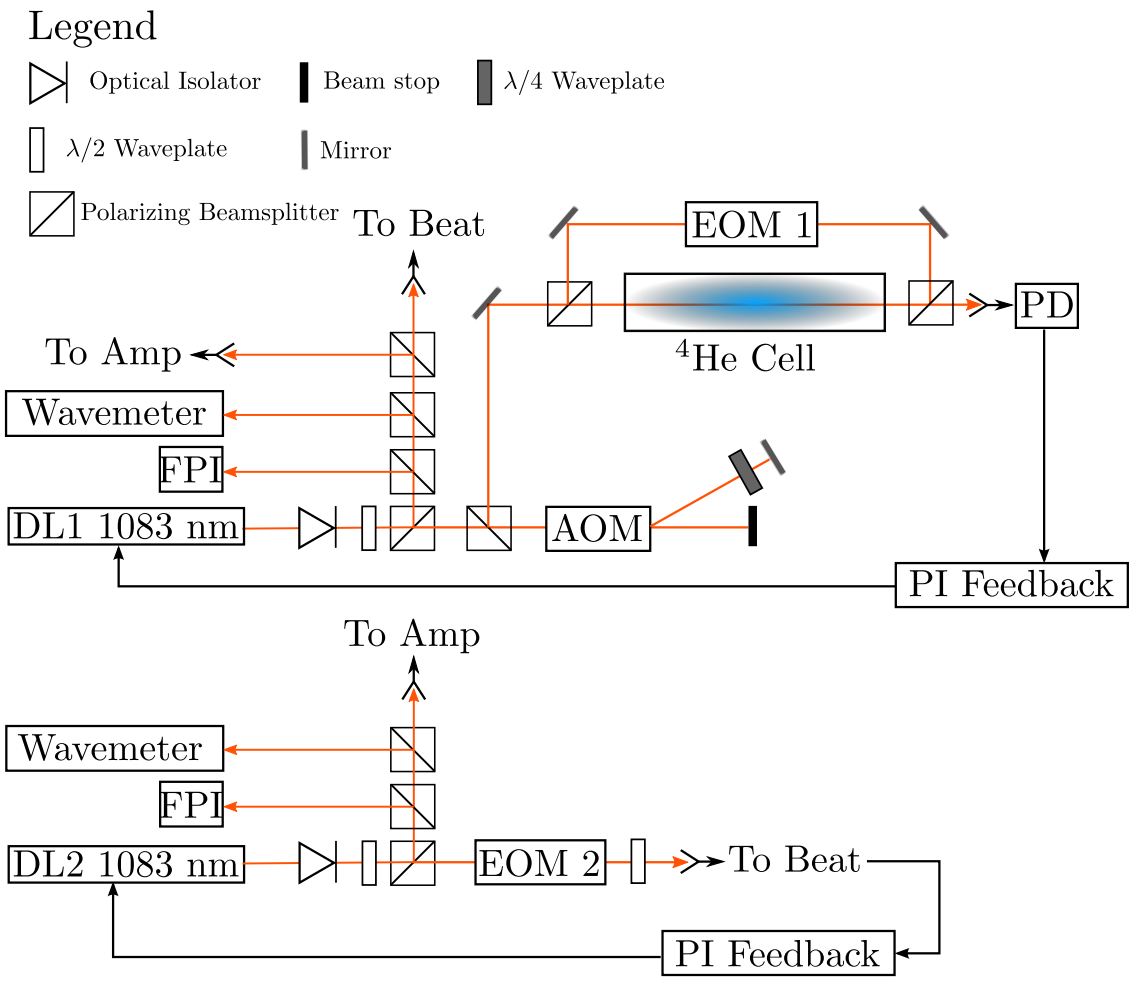

Figure 4.13: The lock scheme for the 1083 nm laser system. FPI: Fabry-Perot interferometer, PD: photodetector, AOM: acousto-optical modulator, EOM: electro-optical modulators. The polarizing beamsplitters generally have an accompanying $\lambda/2$ waveplate to control the relative power passing through each path of the beamsplitter.

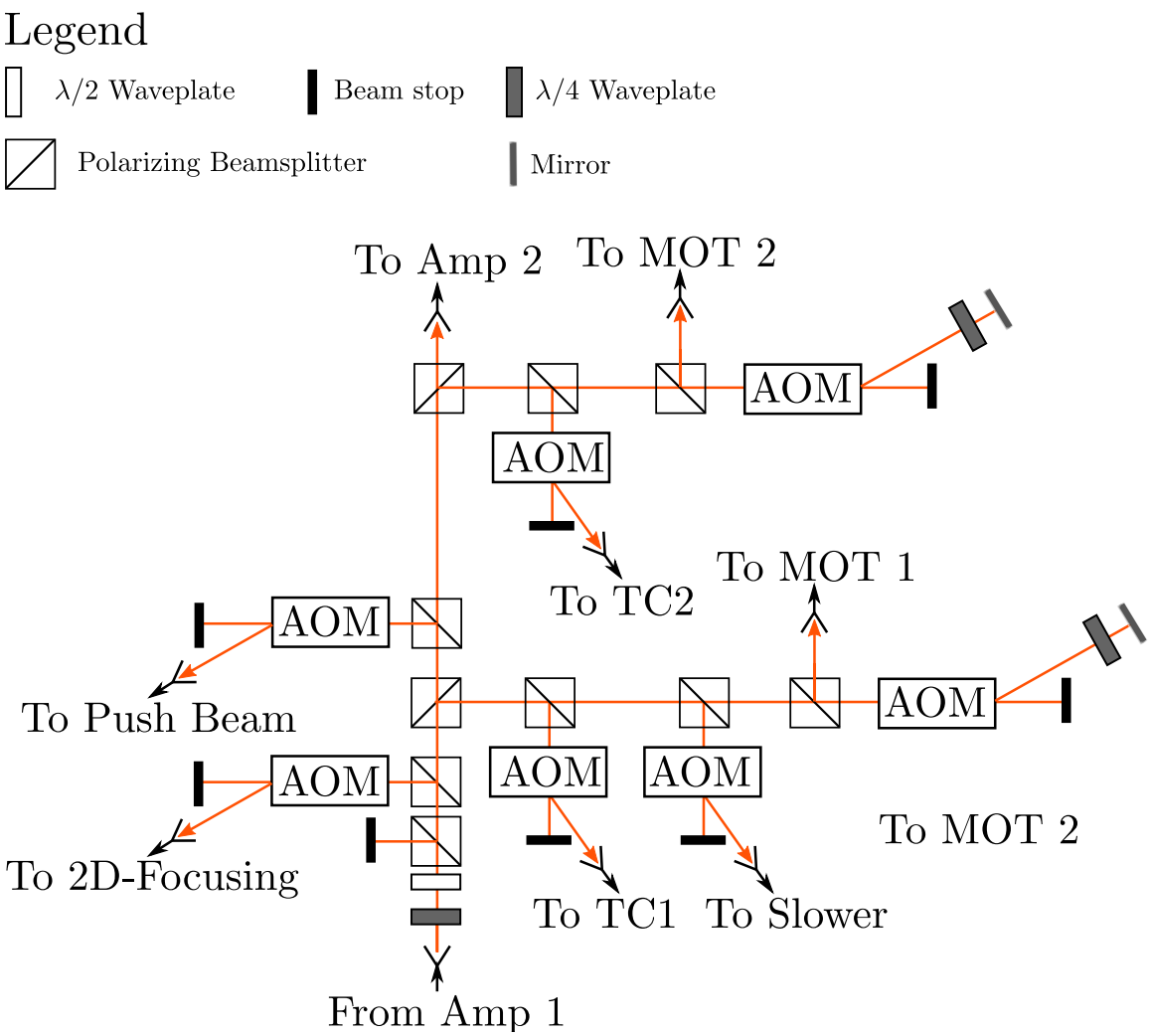

Figure 4.14: The high power scheme for the 1083 nm laser system. A 10 W Keopsys fiber amplifier provides enough power to be distributed to each path used for the experiment. TC1 refers to the first transverse cooling stage. Amp 2 refers to a secondary fiber amplifier used to provide additional light.

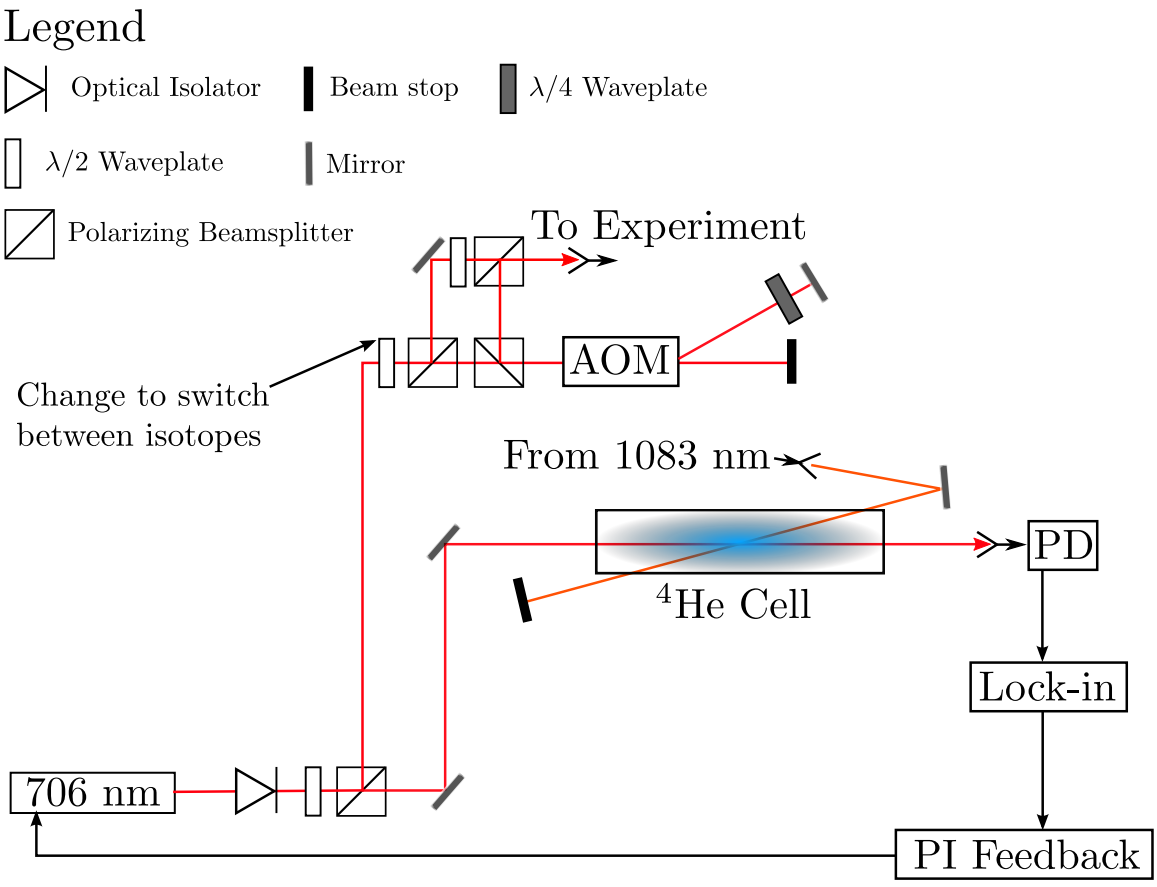

Figure 4.15: The lock scheme for the 706 nm laser system. By changing a $\lambda/2$ waveplate, the double-pass AOM can be by-passed to fluoresce atoms when trapping ^{4}He or used to account for the isotope shift when trapping ^{6}He.

Chapter 5

Detection Systems for the $a_{\beta\nu}$ Experiment

The heart of the experiment is the detection apparatus used to measure the electron and recoiling ^{6}Li ion emitted in the decay of ^{6}He. In Chapter 4 I discussed our methods for transferring the ^{6}He atoms from one MOT to a second MOT. This final MOT chamber doubles as our detection chamber. It contains four crucial elements: a multi-wire proportional chamber in coincidence with a plastic scintillator/PMT, together functioning as a β-telescope, an electrode array for generating a nearly uniform electric field in the flight region of the ^{6}Li ion, and a microchannel plate which functions as a position-sensitive ion detector. In this chapter I will detail each of these components, as well as our data acquisition system.

5.1 Detection Chamber

The body of the detection chamber (see Figure 5.1) is a stainless steel vessel approximately 14.5 inches in length and 8 inches in diameter. The chamber contains in total 14 ports. Four of the 2.75 inch CF ports are used for two pairs of trapping lasers which are mounted at 45-degree angles in the vertical plane instead of the more

usual horizontal mounting to accommodate the vertically-mounted β telescope and ion detector. The third pair of trapping lasers enter from the 6 inch CF ports which in Figure 5.1 point into and out of the page. These ports are larger than for the other trapping laser pairs to accommodate additional crosses to which our turbo-molecular pump, ion gauge, getter pump, and residual gas analyzer (RGA) attach. Two of the remaining 2.75 inch CF ports in the horizontal plane are used for optical monitoring of the atomic cloud as well as for a magnetically-coupled transport tube which allows for the introduction of various radioactive sources into the center of the chamber to test our detectors. Finally, one 2.75 inch port is connected via a 6-way cross to the first MOT chamber and allows the transfer of the ^{6}He cloud from the first trap to the second. The other ports are unused at this time.

Not shown in Figure 5.1 are the MOT coils which are mounted around the 6-inch flanges on either side of the chamber and are separated by about 8.5 inches. These water-cooled coils are approximately 6 inches in diameter and have 78 windings of copper wire. At our operating current of 15 A DC, these coils produce a magnetic field gradient of $\sim$10 G/cm along the coil axis and $\sim$5 G/cm perpendicular to the axis. We achieve our high vacuum of $\leq 1\times10^{-9}$ Torr, which is as low as our ion gauge controller can read, with a 250 L/s turbomolecular pump backed by another 50 L/s pump. In addition, we use a 400 L/s non-evaporable getter pump to reduce the H_2 partial pressure. This yields trapping lifetimes in the detection chamber of $\sim$3 s as measured with traps of ^{4}He.

5.2 The β telescope

For our beta detector we use a combination of a multi-wire proportional chamber (MWPC) as a ΔE detector with a plastic scintillator optically coupled via lightguide to a Hamamatsu R1250 photomultiplier tube (PMT) as our main energy deposition detector. We use a re-entrant design to place the detectors as close to the center of

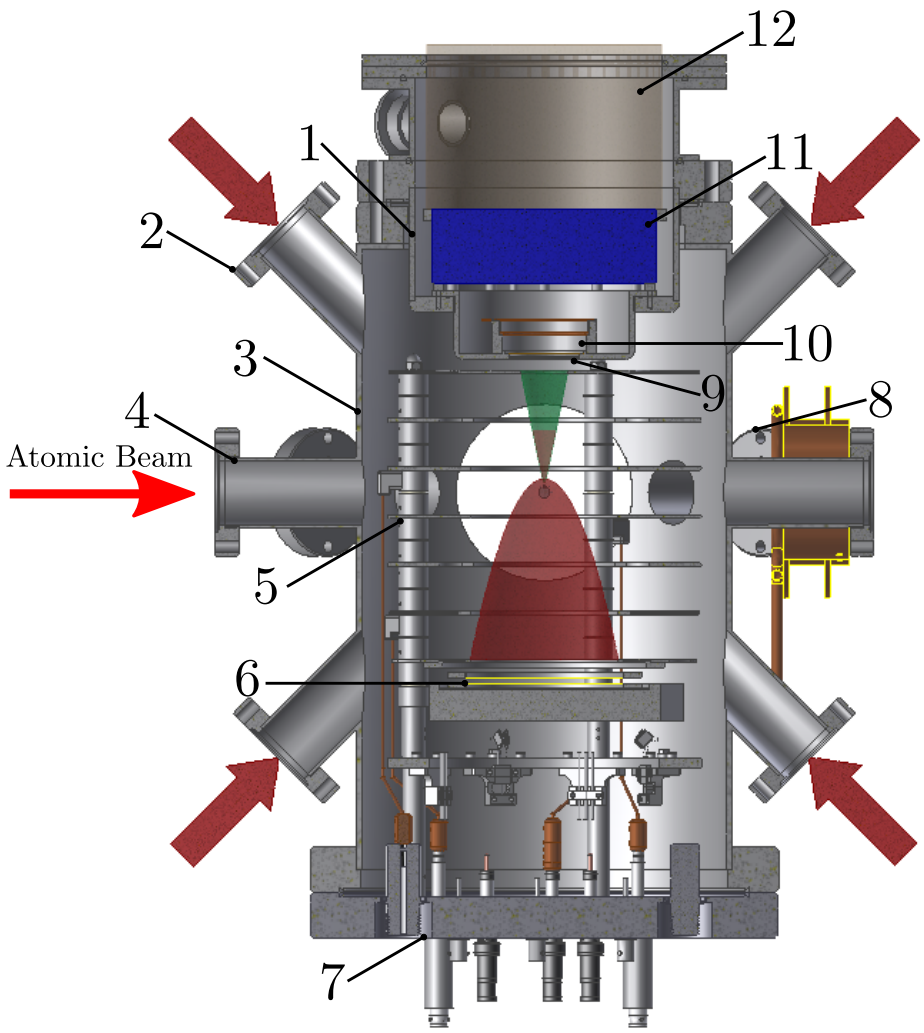

Figure 5.1: Cross-section of the second MOT/detection chamber: **1** re-entrant β telescope housing, **2** trapping laser ports, **3** main chamber, **4** ^{6}He tranfer port, **5** electrode assembly, **6** microchannel plate (MCP) recoil ion detector, **7** 10 inch custom feedthrough flange for HV and MCP connections, **8** trap monitoring ports, **9** 127 μm Be foil, **10** multi-wire proportional chamber (MWPC), **11** plastic scintillator, **12** lightguide.

the main vessel as possible to maximize our collection solid angle, and are limited ultimately by the diagonal trapping laser beams. Figure 5.2 shows a cross-section

view of the β telescope.

5.2.1 Scintillator and Photomultiplier Tube

Our plastic scintillator, made of EJ-200 polyvinyltoluene [106], measures 4.7 inches in diameter and is 1.5 inches thick. Atop the scintillator is a PMMA acrylic lightguide which is 5 inches in diameter and 13.5 inches in length. The scintillator is optically glued to the lightguide and suspended above the ΔE detector. The lightguide, which is wider than the scintillator, in turn rests on a shelf surrounding the scintillator, with a rubber O-ring present to prevent damage to the plastic. The lightguide as well as the scintillator are wrapped with 3 layers of Teflon to enhance diffuse reflections and minimize scintillation light loss. The lightguide is then wrapped with an additional layer of black electrical tape to prevent external light from leaking in. All sealing surfaces are also wrapped with a few layers of electrical tape for the same reason. The reason for the length of the lightguide is to distance the PMT from the magnetic fields generated by the MOT coils, which would otherwise distort the PMT signal. To further shield interference from the magnetic fields, a sheet of μ-metal is wrapped around the lightguide/PMT assembly.

The principal purpose of the β telescope is to start the clock for measuring the time of flight of the recoiling ^{6}Li ions while defining the direction of the emitted β particle. For this reason it is more important that the timing resolution is good ($\sim$450 ps) than is the energy resolution of the detector ($\sim$15% full-width half maximum at 1 MeV), which is better in silicon detectors, for example. The information about the deposited β energy is still useful for analysis cuts, however, so it is important that the low-Z plastic material minimizes the losses and related false energy readings caused by the backscattering of incident β particles. For this reason, we avoid silicon detectors when measuring the β energy.

Our gain stabilization procedure is passive such that the energies recorded by the

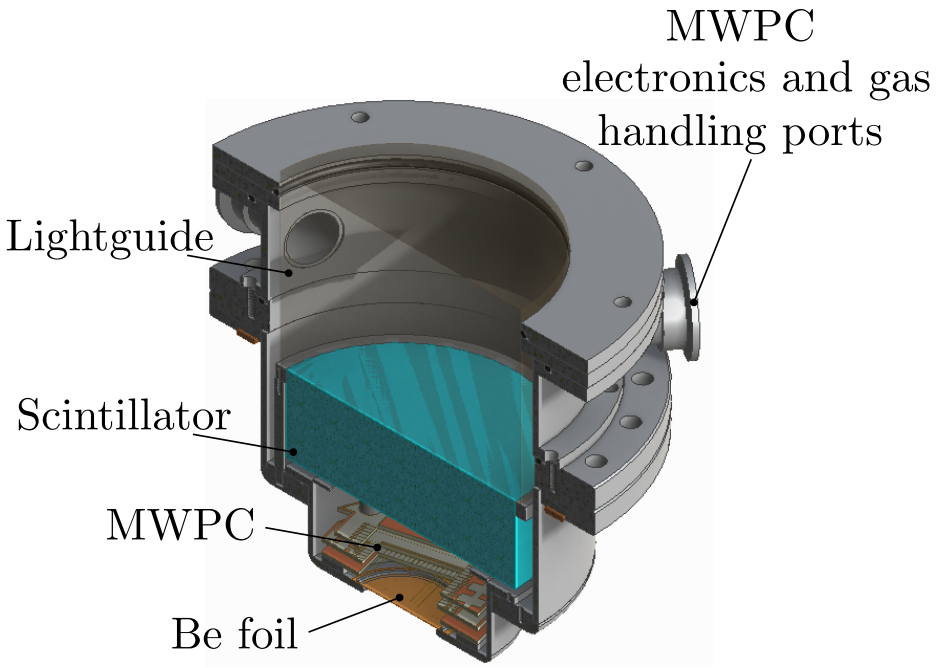

Figure 5.2: Cross-section of the β telescope. Surrounding the lightguide is a custom flange used for controlling the flow of the 90% Ar, 10% CO_2 proportional gas as well as providing feedthroughs for the high-voltage and signal cables used for the MWPC. A 127 μm beryllium foil separates the one atmosphere pressure of proportional gas from the ultra-high vacuum of the trap.

scintillator/PMT are altered offline during analysis according to a reference signal. Prior to any data run a radioactive source of ^{90}Sr is placed near the β detector and its $\sim$2.8 MeV endpoint identified. By identifying the known endpoint of the ^{90}Sr source, the gain of the β detector can be known and the ADC channels scaled appropriately. More recently we have switched to a ^{207}Bi source which features several monoenergetic conversion electron lines at 482 keV, 976 keV, 1682 keV, and additional weaker lines. By simulating events with these energies entering the beta detector, taking into account the $\sim$40 keV loss through the Be window, we can compare the resulting spectrum to a measured spectrum with a source and thereby determine the

linearity of our PMT. At the same time, a blue LED shines light into the lightguide. The intensity of the blue LED light pulses are chosen to be well above the endpoint of our target ^{6}He source ($Q = 3.5$ MeV) and is usually chosen to be around 5 MeV. Some of the blue LED light is split off and shines onto a silicon photodiode, and this splitting fraction remains constant. The controller for the blue LED in general is not sufficiently stable so the number of photons emitted per second is not a constant, but by taking the ratio of the gains of the stable silicon photodiode and the PMT, we can cancel out the drift of the LED controller and therefore monitor the PMT for any gain drift.

5.2.2 Using a Multi-Wire Proportional Chamber for ΔE

We use as our ΔE detector a multi-wire proportional chamber designed and built by group member R. Hong [107]. This chamber serves two purposes: one is to act in coincidence with the scintillator/PMT to reduce the rate of background events, and the other is to provide the initial β direction used in the kinematic reconstruction of the $\beta - \nu$ emittance angle. Inside the chamber are three planes separated by 0.25 inches each with gold-plated tungsten wires soldered to the plane and regularly spaced 2 mm apart (see Figure 5.3). Two of these wire planes serve as cathodes, and sandwiched in between them is a plane of anode wires. The anode wires are elevated to +2800 V with a high-voltage supply while the cathode wires are held at ground. When an energetic, charged particle passes through a gas mixture of 90% argon and 10% CO_2, it produces ions in proportion to the deposited energy. For our gas, the average energy needed to create an electron-ion pair is about 26 eV. Some of these positively-charged ions are produced near the anode wires and are repelled by the high positive voltage, while the electrons are attracted to the anode wires. As the ions gain energy they in turn ionize more gas, creating an ionization avalanche. While a few dozen ions are produced for each 1 keV of energy loss from the β, some 10^5

electron-ion pairs occur from this multiplication process. As the ions continue to be pushed away from the anode wires they come closer to the cathode wires, inducing a negative charge which is also read.

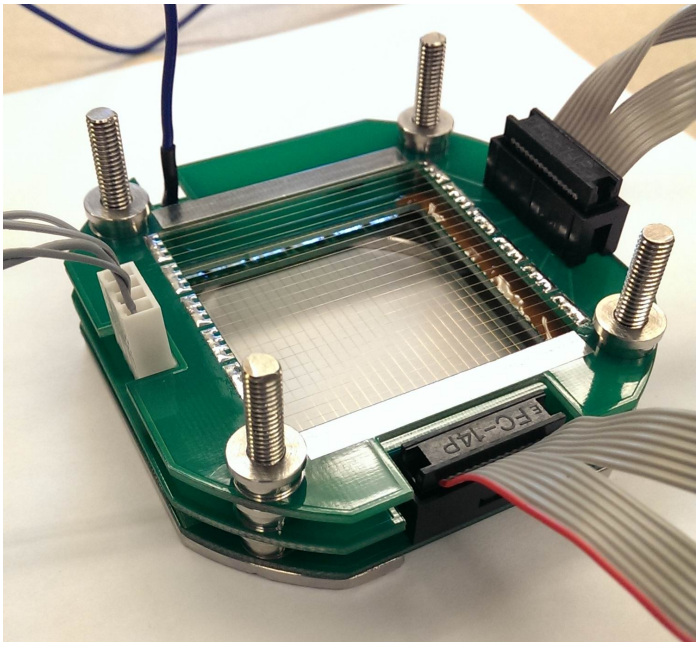

Figure 5.3: The multi-wire proportional chamber as seen from above. The top cathode runs parallel to the anode in the middle plane. The diameter of the cathode wires is 50 μm, while 10 μm diameter wires are used for the anodes to increase the local electric field and produce a larger avalanche. Not shown here is the supporting frame used to attach the MWPC to the rest of the β detector chamber.

Position reconstruction can be done either by reading each wire individually, or by charge division and weighted charge-position averaging. We choose the latter to reduce the number of read out channels required, so out of 24 wires on each plane we form groups of 4 wires soldered together to make 6 wire groups. Capacitive charge division is used for the anode reconstruction, and weighted charge-position averaging is used for the cathode reconstruction. To reconstruct a position in two dimensions, the lowest cathode wires are run perpendicular to the anode wires. The top cathode

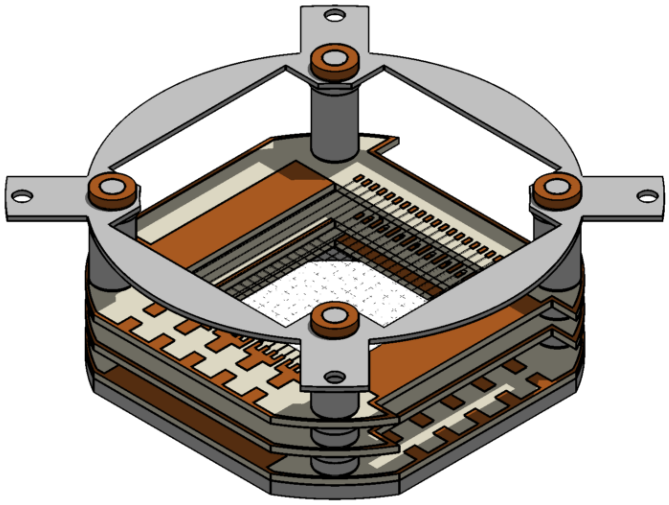

Figure 5.4: A render of the complete MWPC assembly. The supporting frame allows the MWPC to be suspended above the beryllium foil and below the scintillator.

wires are run parallel to the anode wires. In this way, the lower cathode can determine the X-coordinate of the avalanche, while the anode and top cathode can determine the Y-coordinate. The top cathode is redundant for the position reconstruction, but useful for studying the properties of the chamber. The position resolution achieved with this detector is approximately 1 mm within an active area of 48 mm$\times$40 mm. The details of the position and energy calibrations will be presented in a forthcoming paper [107].

A custom flange (shown in Figure 5.2) has four KF-25 ports to provide access for electronics and proportional gas. Two of these ports contain feedthroughs for collecting the anode and cathode signals, respectively, and two are used as gas inlet and outlet ports. One of the gas ports is shared with a SHV feedthrough for elevating the anode wires. We operate the MWPC at 1 atmosphere of proportional gas, so to separate this volume from the trapping vacuum we use a 1.5 inch diameter, 127 μm thick beryllium foil which is fusion bonded to the re-entrant β telescope chamber. These dimensions were chosen so as to withstand the pressure differential without

failure while minimizing straggling of the β as it passes through the foil.

We choose to use an MWPC over a double-sided silicon strip detector principally due to its simultaneous high-efficiency detection of β particles ($\sim$90% at 1 MeV) and near complete insensitivity to gamma rays. False coincidences due to gamma rays would yield an erroneously measured time of flight for the ^{6}Li ions. Both bremsstrahlung gammas caused by β scattering in the detection chamber and gamma rays produced by our nearby accelerator can be vetoed when the MWPC is used in coincidence with the scintillator/PMT while not sacrificing β detection efficiency.

5.3 Microchannel Plate

Our ^{6}Li ion recoil detector consists of a stack of two microchannel plates (MCPs) assembled in a chevron configuration. The 1.5 mm thick MCPs feature 25 μm pores (length/diameter ratio 60:1) with a 20 degree bias angle from vertical. It has at least a 75 mm active detection diameter, and is capable of handling up to a 1 MHz detection rate. The open area ratio (OAR), or the ratio of the open channel area to the total area of the MCP, is in our case 70%. The MCPs are sandwiched in between two ceramic rings to isolate the MCPs from the rest of the assembly. The ceramic rings each have a copper ring attached to them which can be biased to provide the electric field needed for electron multiplication inside the MCP channels. The chevron configuration of the MCP provides two stages of electron multiplication resulting in a gain factor of about 10^7 or more for applied voltage differences of $\sim$2500 Volts.

Figure 5.5 shows a schematic drawing of the main MCP assembly (assembly model DLD80 by RoentDek [108]). After multiplication, the electrons are further accelerated onto the delay line anodes. Separating the back of the MCP from the anodes is a holder plate which is biased to make the electric field in the region of electron flight more uniform. The electrons from the MCP are deposited onto the delay line anodes and are in turn collected at each end of the anode wires. The difference in the time

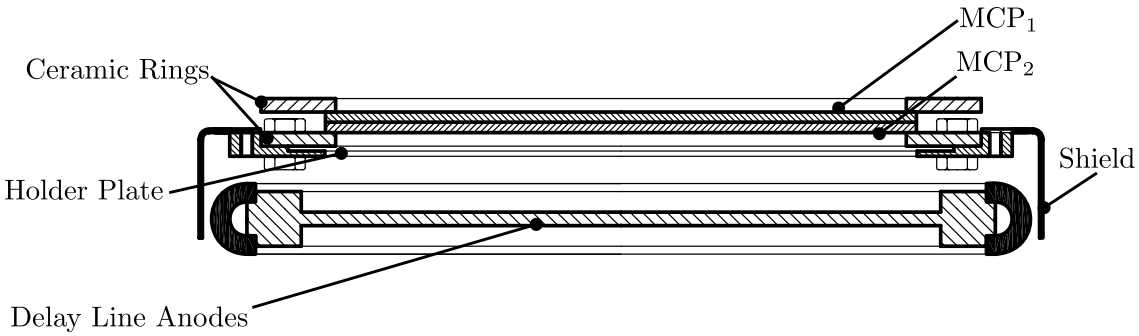

Figure 5.5: Schematic drawing of our MCP assembly.

between when the charge is collected at each end is proportional to the position of the initial deposited charge, given the known distance of the anode wire. Two wires are wrapped in orthogonal directions to given two-dimensional spatial information. Figure 5.6 shows a picture of the delay line anodes with the MCP stack removed. Each anode wire is actually a pair of wires. One half of the pair is the collection wire, called the signal anode, and the other wire is the reference anode. The signal anode is biased to a higher potential than the reference anode so that electrons are preferentially attracted to it (see Table 5.2 for a list of voltage settings). The reference anode is used to compare and therefore subtract the shared electronic noise in the wire pair. We use a delay line anode for position reconstruction in two dimensions for several reasons. It has a high rate tolerance ($\sim$ 1 MHz) due to its fast read-out, it has a high position resolution ($<$ 0.1 mm), and it is less susceptible to noise when compared with resistive anodes.

We are still developing methods for position calibrations with our MCP. Presently we have a mask (90% visibility) situated directly atop the MCP with a well-defined rectilinear grid structure, measured by a microscope to within 1 μm, which we can compare with our MCP data (see Figure 5.7). Figure 5.8 shows background data taken with an α-source (^{241}Am) sitting at the center of the detection chamber and gives a clear picture of the shadows caused by the mask. The radius of the mask is

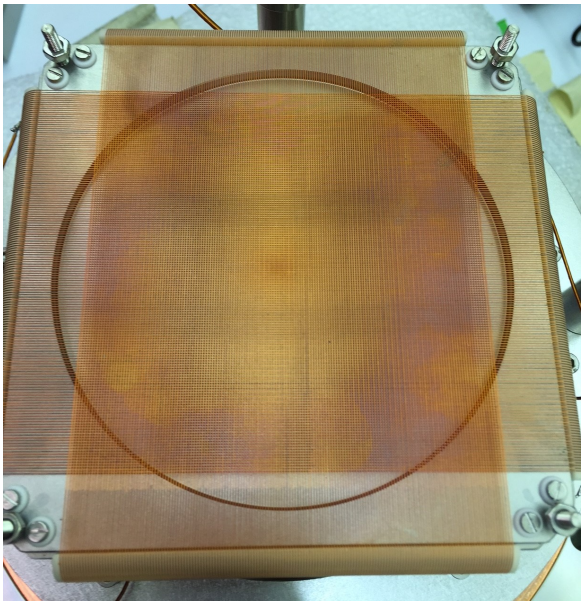

Figure 5.6: Picture of delay line anode with densely wound wires in X and Y.

smaller than the active area of the MCP, giving a well-defined maximum radius which we can also use to check against the data. The mask is also well-centered with respect to the detection chamber and can therefore be used for both relative and absolute position measurements. In the future we will correct our data by calibrating the MCP using the positions of the crossing points of the shadows to account for the distortions caused by fringe electric fields. These distortions are greatest near the edges of the MCP.

5.3.1 Systematic Studies with the MCP

In addition to its usefulness as a recoil ion detector, the MCP is also used as a diagnostic tool to study some systematics of our experiment. The position stability of our trapped atoms may be measured by looking at Penning ions formed by collisions of the trapped metastable atoms with background gases. These Penning ions are imaged onto the MCP and serve as a proxy for the position, size, and shape of the

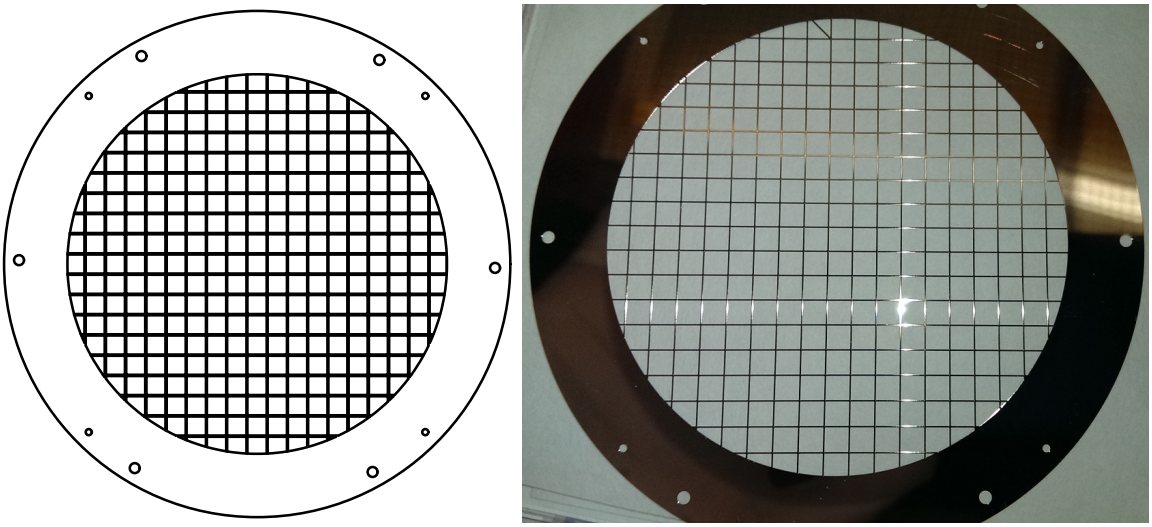

Figure 5.7: (left panel) Schematic drawing of the mask used for calibrations of the MCP. (right panel) Photo of the actual MCP mask. A diagonal line at the top serves as a registration mark for orientation.

trapped atoms. By momentarily releasing the atoms and observing the change in the size of the Penning ion cloud as seen by the MCP due to the ballistic expansion of the trapped atoms, we gain information about the kinetic energy distribution of the trap, and therefore its temperature. Figure 5.9 shows a trap just before release, as well as some time after release. We fit the $X - Y$ profile of the trap as a function of time to extract the temperature.

5.3.2 Photoionization from a N_2 laser

The MCP is also useful as an independent probing detector for the electric field (see Section 5.4). Stable ^{4}He atoms may be trapped in the detection chamber and photoionized by a 337 nm nitrogen laser. These low-energy ions are then accelerated by the electric field onto the MCP where they are well-localized. This time of flight (TOF) information provides a measure of the average electric field along the detection

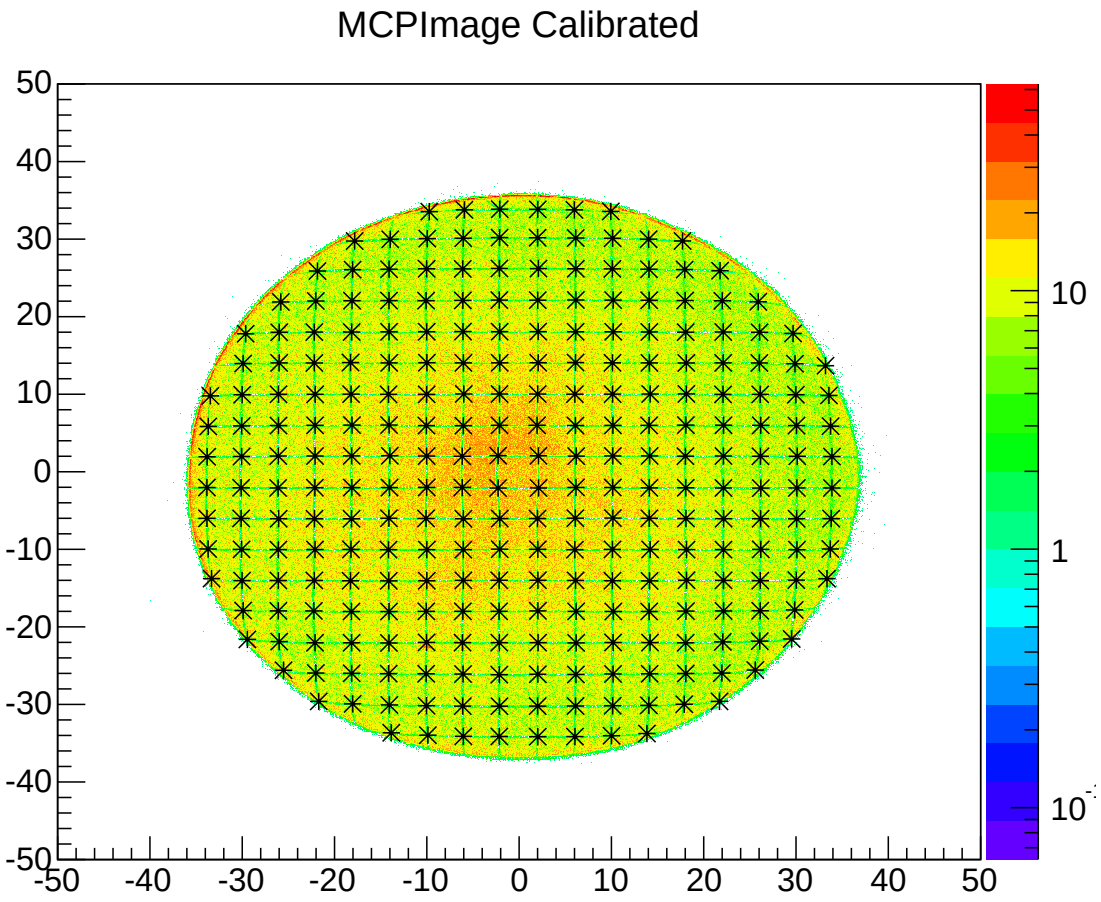

Figure 5.8: The MCP after calibration showing good efficiency uniformity. An α-source placed at the center of the detection chamber showered activity onto the MCP. Dark lines can be seen where the mask blocked the MCP from seeing the α particles. The crossing points of the MCP image are identified algorithmically (stars) and corrected using a polynomial fit to the corresponding locations on the precisely-measured mask.

axis which we can compare to our high voltage probe measurements. We can also probe the uniformity of the field in the $X - Y$ plane by moving the trapped atoms around in the MOT in a limited region (1 cm radius). In this case, the TOF clock is started by a UV photodiode which detects some of the scattered nitrogen laser light.

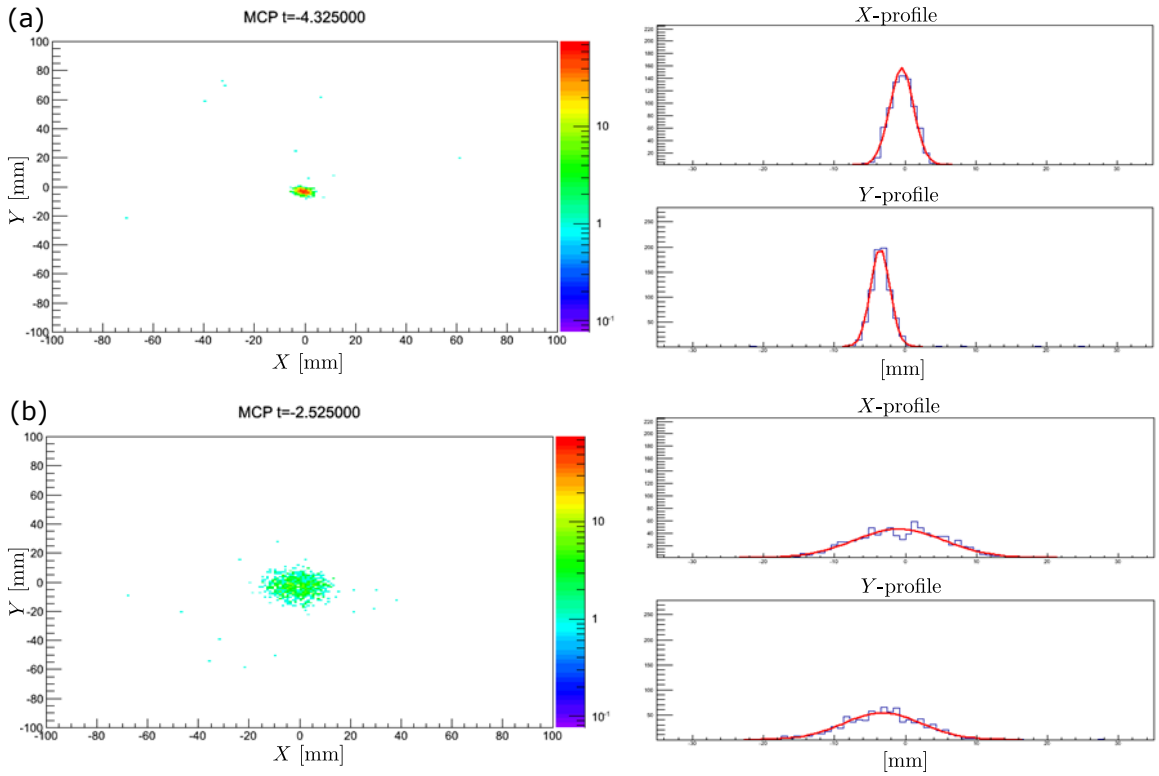

Figure 5.9: Panel (a): MCP image of Penning ions due to trapped ^{4}He atoms. Panel (b): The ^{4}He atoms are released from the trap and allowed to ballistically expand. The resulting Penning ions are created over a wider area. The expansion rate, which is related to the trap width as a function of time, can be extracted to yield the trap temperature. Shown on the right side of each panel is the projection of the MCP data onto the X and Y axes. A fit to a Gaussian profile is used to determine the width of the trap at each time.

The clock is stopped by the signal from the MCP. The MCP itself is slightly sensitive to UV photons, and so light scattered from the chamber walls can also be used to measure the TOF. Figure 5.10 shows a TOF plot of photoionized ^{4}He atoms along with the detected UV photons.

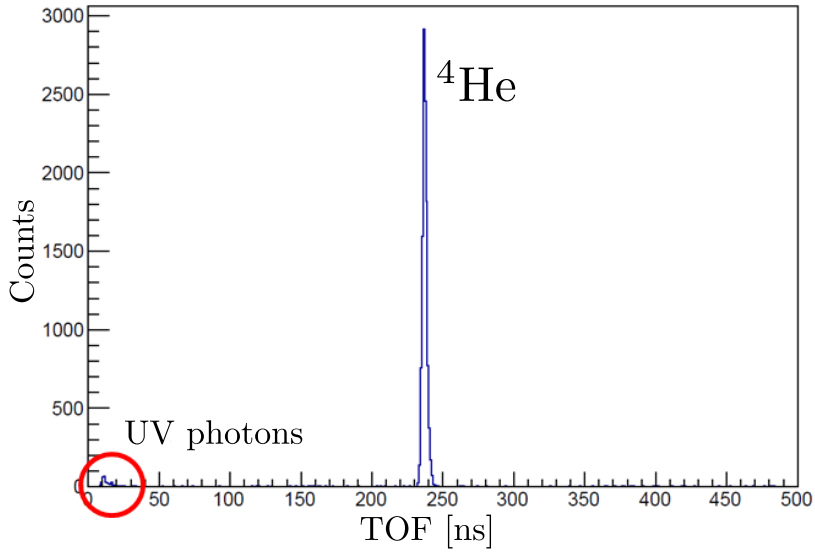

Figure 5.10: TOF spectrum of photoions. UV photons (red circle) are detected by the MCP (or externally by a photodiode) and serve as a timing reference for the TOF of the photoions.

5.4 Electrode Array

The center of the trap, where the decays primarily occur, is approximately 95 mm above the 8 cm diameter microchannel plate (MCP). This amounts to a solid angle of about 4% and with the result that the incident angle of the ions near the edge of the MCP would be 22 degrees. Additionally, following the decay of ^{6}He the recoil ^{6}Li ion has an endpoint energy of approximately 1.4 keV. The efficiency of microchannel plates depends upon both energy and incidence angle. Figure 5.11 shows this angular dependence of detecting an electron beam for a typical Hamamatsu MCP [109], indicating a significant efficiency dependence as the incident electron angle moves away from the optimal value of 13 degrees. Table 5.1 lists the MCP detection efficiencies for different energies and particle types, showing a substantial gain in efficiency for ions in the tens of keV energy range over the ∼1 keV energy range. To reduce systematic

effects associated with these dependencies, and to increase our overall solid angle and detection efficiency, we use an array of electrode rings to generate a ∼1.55 kV/cm electric field which guides ∼95% of the ions within the 8 cm diameter of the microchannel plate.

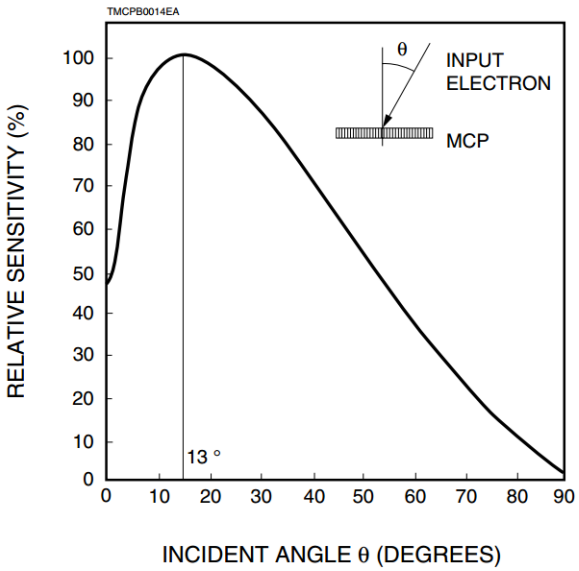

Figure 5.11: Relative MCP detection efficiency of 1 keV electrons for various incident angles. The optimal angle depends on the angle of the channels of the MCP. The angular dependence on the detection efficiency is similar for ions. Accelerating the ions makes the angular distribution at the face of the MCP more uniformly vertical, reducing the systematic effects due to this angular dependence. Figure reproduced from [109].

The decay of ^{6}He principally produces two charge states of ^{6}Li: $^6Li^+$ and $^6Li^{++}$. Nearly 90% of all decays yield singly-charged $^6Li^+$. The doubly-charged lithium ion is caused by a mis-match of the wavefunctions of the initial helium and final lithium atomic states, and amounts to approximately 10% of all ions [110]. An insignificant fraction of about 0.04% wind up in the fully-ionized $^6Li^{3+}$ state. The electric field partially separates the time of flight spectra of the ion charge states, but not entirely.

The electrode array consists of six annular rings made of 2 mm thick stainless steel

Types of Radiation	Energy or Wavelength	Detection Efficiency (%)
Electron	0.2 keV to 2 keV	50 to 85
	2 keV to 50 keV	10 to 60
Ion (H^+, He^+, Ar^+)	0.5 keV to 2 keV	5 to 58
	2 keV to 50 keV	60 to 85
	50 keV to 200 keV	4 to 60
UV	300 Å to 1100 Å	5 to 15
	1100 Å to 1500 Å	1 to 5
High Energy Particle (ρ, π)	1 GeV to 10 GeV	to 95

Table 5.1: MCP detection efficiencies for various incident particles and energies taken from [109]. Electrostatic acceleration increases the kinetic energy of the primary $^6Li^+$ charge state by an additional 24 keV, which maximizes the detection efficiency of the MCP.

which is suitable for our ultra-high vacuum environment. A cross-section view of the electrode assembly and high-voltage flange can be seen in Figure 5.12. We chose to use stainless steel over lower Z conductors such as aluminum to avoid patch charges which can form on the oxide layer of aluminum and distort the electric field. Stainless steel is also easy to machine, so it serves as a good starting point. Each electrode is separated from its neighbors by 24 mm with Macor [111] ceramic spacers. Surrounding the ceramic spacers are stainless steel sleeves in contact with the electrodes to which the high-voltage is supplied. These conductive sleeves screen the ceramic spacers from the rest of the trap volume and prevent patch charges on the spacers from distorting the electric field in the center of the chamber.

Four of the six electrodes have partial cutouts to allow for the MOT laser beams to pass through. These cutouts perturb the uniformity of the electric field and the voltages of the electrodes must be adjusted to compensate. We use the finite-element

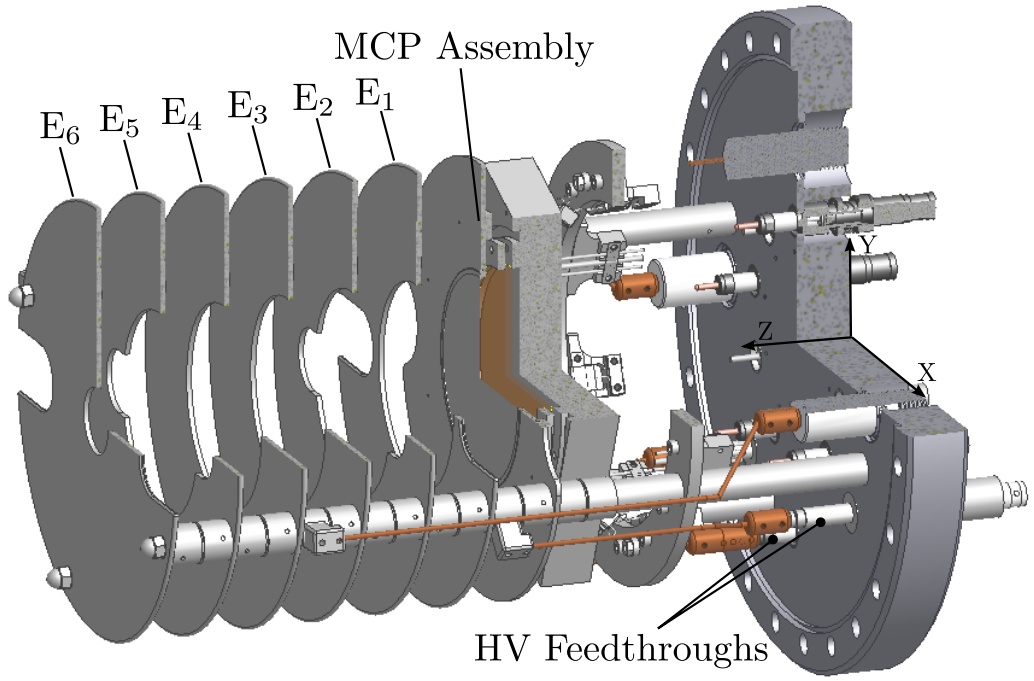

Figure 5.12: Three-quarter view of the electrode assembly. E_6 is the electrode at the top of the stack. This electrode also serves as a β-collimating electrode to restrict the number of detected events which scatter off the MCP or chamber walls. Cutouts are made throughout the electrodes to allow for trapping lasers to pass through. See Table 5.2 for a list of settings for each component under high voltage.

analysis "AC/DC" module of the COMSOL Multiphysics Modeling Software [112] to construct a realistic field map for each electrode. This software was chosen because it allows us to import the same CAD geometries we used when commissioning construction of the electrode array and assembly to ensure accuracy. We then use the "least-squares fit to a polynomial" method found in Chapter 7 of Reference [113] to simultaneously solve for the voltages required on each electrode to generate the desired uniform electric field of 1.55 kV/cm in the ion flight region.

The electric field is computed for points on a dynamic mesh whose mesh spacing is determined by the input geometry. A mesh spacing parameter is chosen such

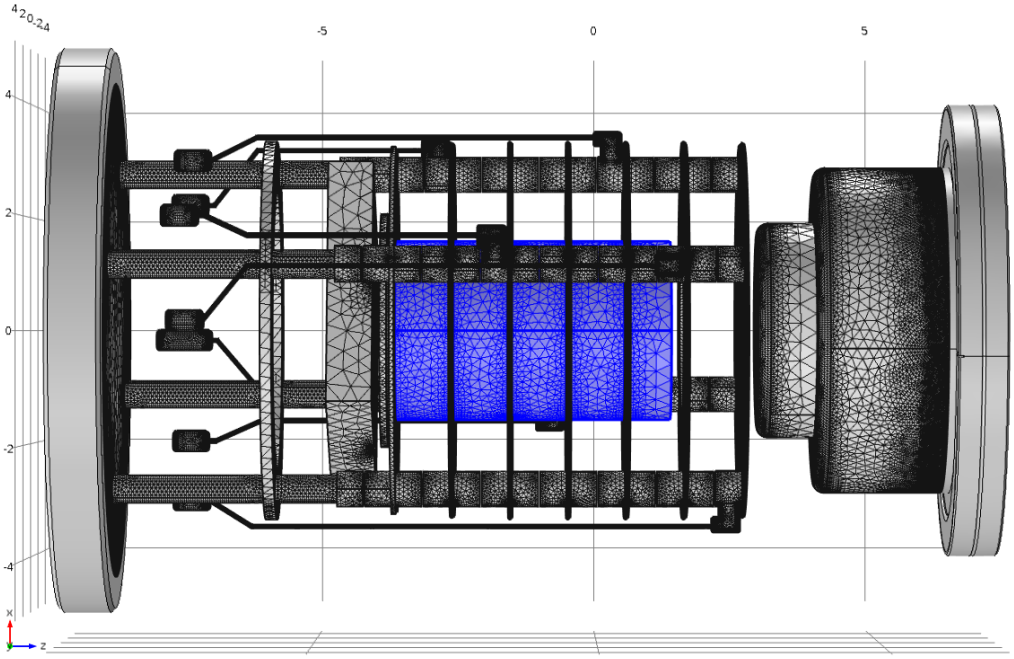

Figure 5.13: Shown are the mesh boundaries which are defined by the input CAD data of the electrode assembly. The surrounding vessel is not shown but is present for the calculations. The blue cylinder defines the region of ion flight and is constrained to have the highest mesh density for increased field calculation accuracy.

that increasing the number of points on the mesh did not significantly change the electric field in the region of interest. A region closest to the flight paths of the ions is chosen with the highest mesh density. Figure 5.13 shows only the boundaries of the three-dimensional mesh generated by COMSOL, including the boundaries of the CAD geometries as well as the boundary of the flight region. COMSOL then outputs electric field values at various points along a uniformly-spaced grid. The spacing of the grid is 1 mm in each dimension, with 87 points along each transverse direction (X/Y), and 201 points along the detection axis (Z). We then use trilinear-interpolation to calculate the electric field for points in between grid nodes when simulating ion trajectories. Table 5.2 compiles the potentials for each elevated component resulting

Source	U(V)	Source	U(V)	Source	U(V)
Electrode 6	22640.19	Electrode 3	10464.78	MCP Front	−1450.00
Electrode 5	18461.87	Electrode 2	6487.61	MCP Back	1092.00
Electrode 4	14568.53	Electrode 1	2388.41	Holder Plate	1276.00
				Reference Anode	1519.00
				Signal Anode	3522.00

Table 5.2: List of voltage settings optimized for a uniform 1.55 keV/cm electric field within the region of ion flight.

from these calculations. Figure 5.14 displays the uniformity of the field along the $Z-$axis for various transverse displacements in the direction of the electrode cutouts (the $X-$axis).

5.5 Data Acquisition

The Data Acquisition system used for this experiment consists of several digitizing modules which are collectively named the Fast Acquisition System for nuclEar Research (FASTER) [114], developed by the Laboratoire de Physique Corpusculaire (LPC-Caen). The FASTER system is a triggerless DAQ which samples data for digitization at a fixed rate such that all the data are timestamped. We use six CARAS 12-bit FPGA[1] daughter cards which can function as QDC-TDC or ADC-TDC[2] modules. Each card has 3 FPGAs and 4 BNC inputs. Two of the FPGAs function as the signal shapers and digitizers independently from each other, and accept 2 inputs each. The third FPGA communicates with the crate to send the signals to the DAQ

[1]Field-Programmable Gate Array

[2]Charge-to-Digital or Analog-to-Digital Converter

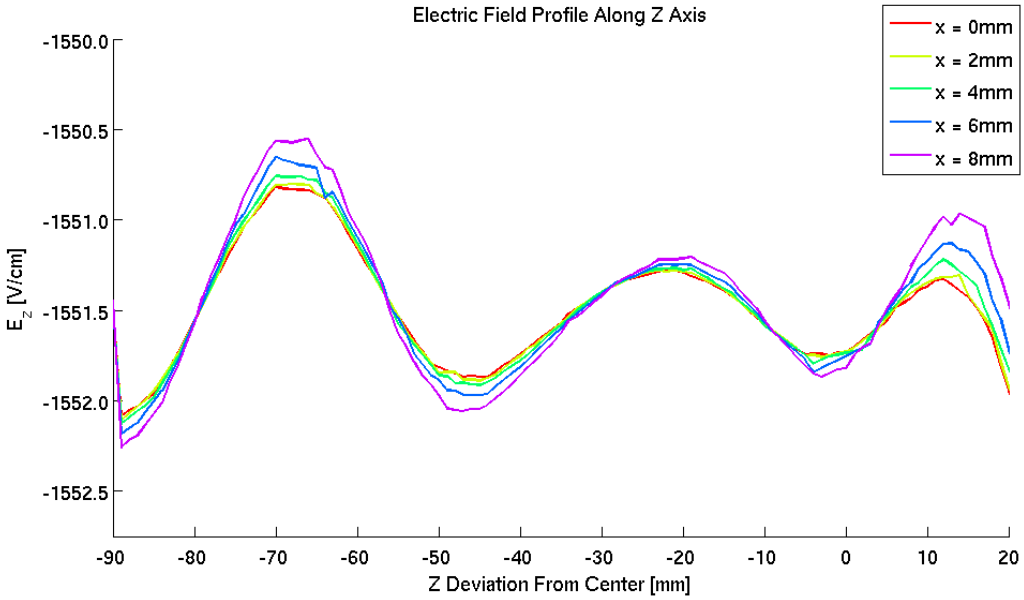

Figure 5.14: Electric field profile along the $Z-$direction after optimization. The colored curves display the Z$-$component of the electric field along the $Z-$direction for various transverse displacements aligned with the electrode cutouts. $Z = 0$ corresponds to the center of the electrode array and coincides with the MOT position. The oscillations in the electric field are correlated with the position of the electrodes, with the largest non-uniformities appearing at Z positions corresponding to the electrodes.

computer, which runs the FASTER software on the Ubuntu operating system. One of the six cards is chosen as the master card whose 500 MHz clock is shared with the other cards for synchronization.

The QDC modules use a CFD[3] to determine the timing of the signal, and can therefore determine the time very accurately (up to 200 ps). The ADCs only give the clock timing and thus are limited to 2 ns for a 500 MHz clock. We therefore choose to use the QDC channels for signals for which we need very good timing information, and ADCs for channels which are not so stringent. The most time-critical components

[3]Constant Fraction Discriminator

of measuring the TOF and final position of the recoil ion for our experiment are the signals of the PMT anode for starting our TOF clock due to the β, the MCP back for stopping the clock due to the recoil ^{6}Li ion, and the delay line anodes for determining the final position of the ion. Collectively, this requires 6 QDC channels, as one channel is used for each end of the X and Y delay line anode wires. Another QDC channel is dedicated to a photodiode to measure scattered UV photons from the N_2 laser used for photoionization and to therefore start a TOF clock for systematic studies (see Subsection 5.3.2).

Our remaining signals are read by 16 ADC channels. Of these channels, 12 are used for reading the pre-shaped and amplified signals from the two 6-wire cathode planes of the MWPC β-detector. Two more channels are used for the anode plane of the MWPC. An additional ADC channels is used for the LED PMT calibration signal to monitor for fluctuations in the number of photons produced by the LED pulser (see Subsection 5.2.1). The last ADC channel is used for a cycling signal which pulses every 12 seconds and serves as the start signal for each data cycle. Each cycle consists of a 3:1 data:background ratio, with the push beam pulsing new ^{6}He atoms from MOT1 to MOT2 at a rate of 4 Hz.

Chapter 6

Preliminary Results on $a_{\beta\nu}$ and Future Prospects

Extracting the angular correlation parameter can be done in a number of different ways. One way is to explicitly measure the recoil ion and beta momenta to kinematically reconstruct the antineutrino momentum and find the relative angle between the beta and the antineutrino on an event by event basis. This requires measuring 6 parameters (one for each component of the momenta of each particle) very precisely. An alternative is to use the time of flight spectrum of the recoil ion in coincidence with a defined beta emission distribution. This yields a simpler analysis and we have chosen to take this route as a beginning step. We in fact use a blend of both approaches, whereby we measure the time of flight spectrum of the recoil ion with a coincident beta, but use the additional information our beta telescope gives us about the beta direction and energy to make cuts on our data set.

Shown in Figure 6.1 is a Monte Carlo simulation of how our data might look assuming $a_{\beta\nu} = -1/3$ along with our experimental parameters, including the solid angle of our detectors, our electric field strength, and the distance from the MOT to the MCP. Projected on each axis of the central 2D plot is the simulated beta energy spectrum and recoil ion time of flight spectrum, respectively. Two peaks,

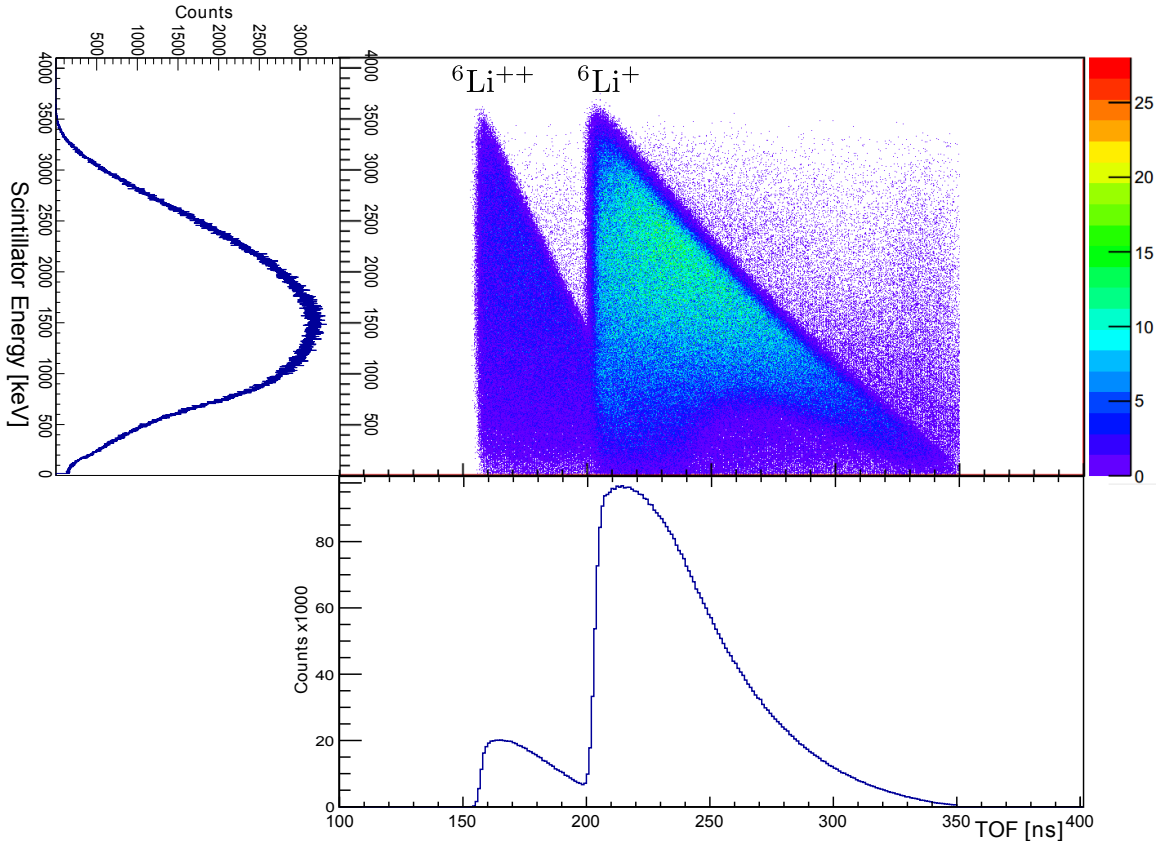

Figure 6.1: Monte Carlo simulation for our experiment assuming $a_{\beta\nu} = -1/3$. Projected onto the vertical axis (left-most plot) is the beta energy spectrum. Projected onto the horizontal axis (bottom-most plot) is the time of flight spectrum of the recoil ions.

corresponding to the two primary charge states of the recoil ion, appear in the 2D and TOF plots. Only events which lie within our TOF region of interest are plotted here. Events which lie outside the "triangles" in the central plot are due to beta scattering, and it is clear that the density of these events increases as the beta energy decreases. Because we have the information about the beta energy, many of these events can be removed during our analysis. Not included in this simulation are events due to untrapped/background atoms. While we have taken precautions to minimize these events, we will have to include them in later data analysis.

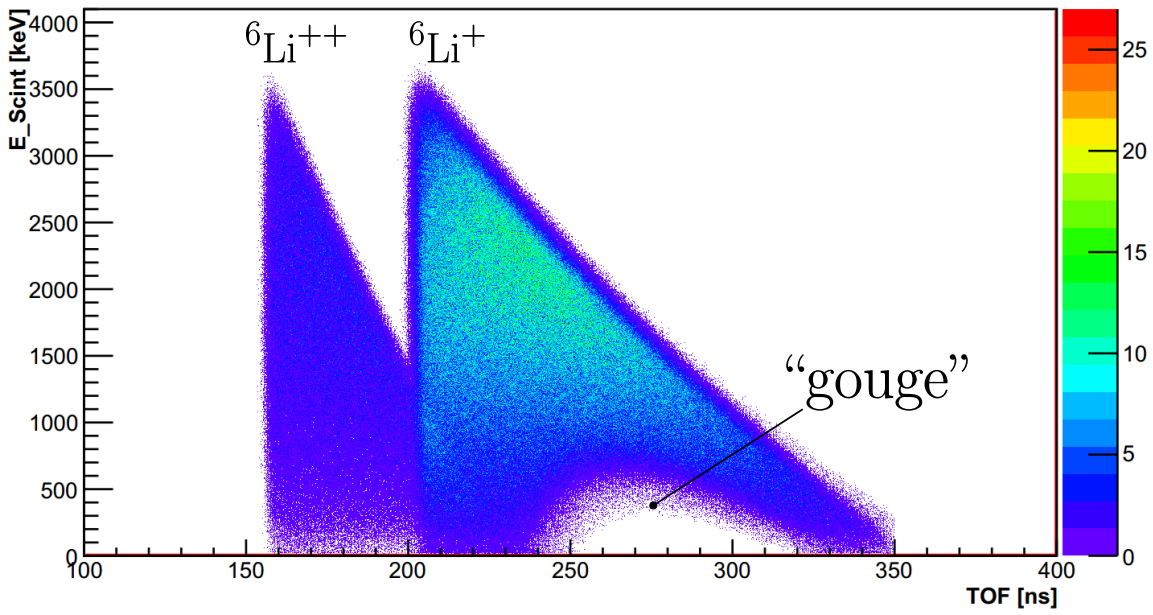

Figure 6.2: Same simulation parameters as in Fig. 6.1 but with all scattering events removed. At the bottom of the primary charge state triangle, a region of missing events is visible.

A region of low/scattered events can be seen at the bottom of the primary charge state triangle. The extent of this "gouge" is determined by the size of our recoil ion detector, or alternatively, by cuts we place on the radius of the detector. This "gouge" can be more easily seen in Figure 6.2, where scattering events have been removed from the simulation. This shape can be understood through a simple argument. The solid angle of our beta detector is $\sim 1\%$, meaning that the beta direction is essentially defined when detected. If the recoil ion detector, which is opposite the direction of the beta detector, also has a small radius, then the neutrino must be emitted either towards the beta detector (up) or away (down), since it shares most of the decay energy with the beta. If the neutrino were to be emitted perpendicular to either detector, the recoil would cause the ion to fall outside the detector radius. Thus, the ion would also be emitted up or down, resulting in two extreme times of flight: shortest

when the neutrino is emitted up, and longest when emitted down. As the beta energy increases less energy is shared by the neutrino, and consequently the difference the neutrino's direction makes in the time of flight of the recoil ion decreases. The two extreme times of flight converge to the shortest time of flight possible, as the large recoil from the beta is the determining factor. Therefore, as one decreases the radius of the MCP, only the outer edges of the triangles remain. Another influence to the shape is the beta energy cut, which removes events from the bottom of the triangles.

6.1 Preliminary Results

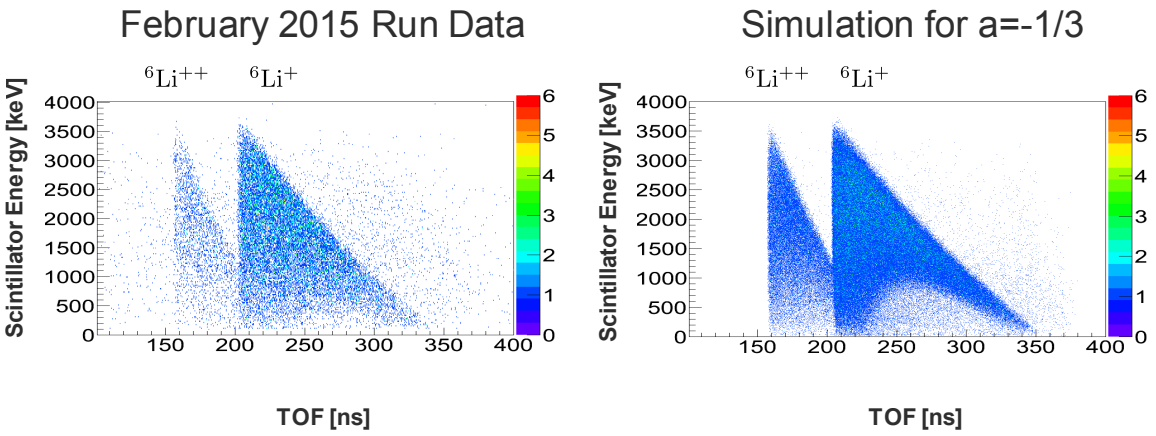

Figure 6.3: (left) Comparison between 2D plot of the recoil ion TOF vs. the β energy (before cuts) as read by the scintillator-PMT during the February 2015 run vs. Monte Carlo generated data (right). Events outside the two charge state triangles are due to scattered beta events and background.

The following is a brief analysis of preliminary time of flight data collected during a run in February of 2015. Shown in Figure 6.3 is a comparison between our raw data set and simulated spectra (assuming $a_{\beta\nu} = -1/3$) which incorporate our measured parameters such as the MOT-MCP distance, trap size and shape, etc. The two

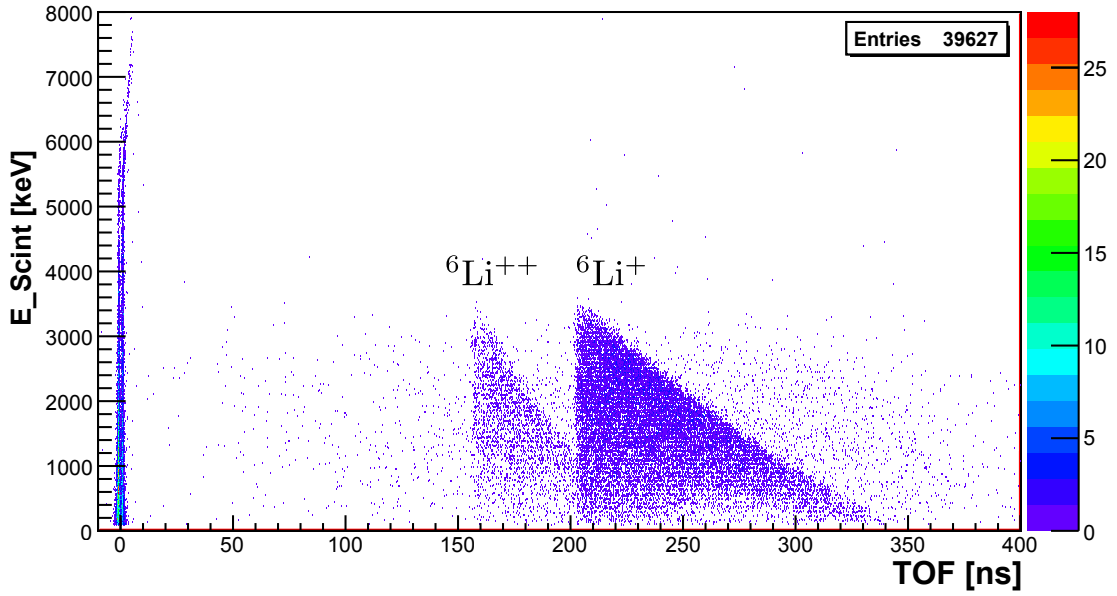

Figure 6.4: 2D plot of the recoil ion TOF vs. the β energy as read by the scintillator-PMT. All data taken during the February 2015 run and filtered with cuts on the β energy, MCP radius, and MWPC radius.

triangles correspond to the two most probable charge states of ^{6}Li, with most of the events landing in the $^6Li^+$ triangle. After making several cuts the data collected during this run amounted to 20,508 recorded triple-coincidence events, reduced from approximately 35,000 raw events recorded over an integrated beam-on-target time of about 24 hours. Among these cuts was an MCP radius cut which removed events which landed outside a 34 mm radius on the recoil detector. This was done to reduce distortion effects due to the electric fields near the edge of the MCP and delay line anodes, and this may change as our MCP position calibration procedures improve (see Section 5.3). We had set our $\beta-$detector threshold to be 800 keV to reduce the effects of beta backscattering. This threshold will likely change to a lower threshold as analysis on the interplay between the uncertainties in the effects of beta scattering

vs. beta energy resolution continues. An additional radius cut of 14 mm was placed on the MWPC to reduce the effects of fringe fields near the edges of the detector.

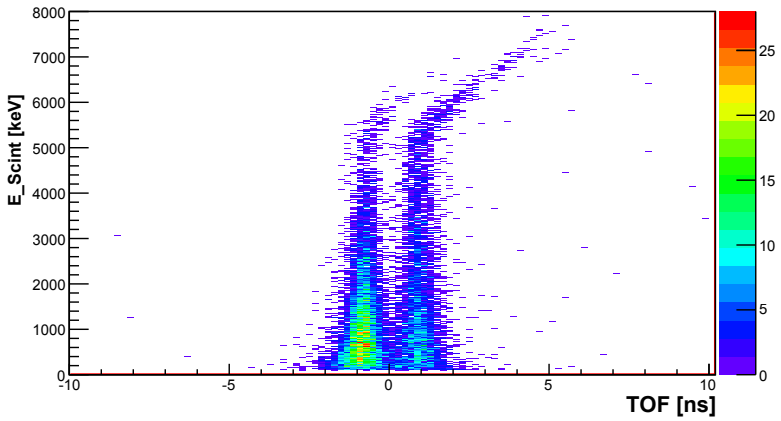

Figure 6.5: Same data as in Figure 6.4 zoomed in to the zero time region, showing the zero timing peaks used in part to calibrate the overall timing of the TOF spectrum. PMT saturation at high energies causes a distortion in the timing spectrum, but this is not a problem for us as the endpoint of our accepted events is at 3.5 MeV, well below this saturation level.

6.1.1 Zero Timing

Shown in Figure 6.4 is the 2D TOF vs. scintillator energy data obtained during the February run after preliminary cuts on the MCP radius and beta energy were introduced. A diffuse background of untrapped ^{6}He atoms generates erroneous events throughout the spectrum and will have to be taken into account in future work. The events at around zero time can be caused by several sources. Betas which backscatter from the scintillator and then go on to trigger the MCP, or which hit the MCP and scatter into the scintillator will cause an erroneous time of flight measurement. Since the order of these events is reversed, there is a small time shift between them of

approximately 2 ns. Radiation shining into the detection area from the accelerator tunnel can also produce a Compton scattered electron in the scintillator which can then trigger the MCP. These events can be much higher in energy than the endpoint energy of the betas produced in ^{6}He decay (3.508 MeV). These events provide a way to perform a preliminary TDC to TOF calibration. Shown in Figure 6.5 is the region of the spectrum near these zero timing peaks. Because our DAQ system defines the time of flight as the difference between the scintillator trigger and the MCP trigger, events which hit the MCP before the scintillator, such as can happen when a beta hits the MCP and scatters into the scintillator, will have a (more) negative time than those prompt events which hit the scintillator first. This difference in time is approximately equivalent to twice the time[1] it takes for a near lightspeed particle to travel from one detector to the other, and amounts to $\sim$2 ns. There is an overall delay caused by instrumentation (photon and electron transport through the scintillator and PMT, etc.) and cabling to the DAQ. We therefore shift the time spectrum such that the new zero is in the center of the two prompt peaks to account for this delay. However, we are interested in the zero time of the ion, and we must therefore also account for the slight delay induced by the beta as it travels from the trap center to the scintillator some 12 cm away. We therefore shift the spectrum by -0.4 ns to account for this delay. In practice this amounted to an overall shift of +63.0 ns (this time shift has already been applied in Fig. 6.4 and Fig. 6.5). At high energies, distortion of the timing spectrum is apparent as the PMT becomes saturated.

These peaks were generated from beta events in both the scintillator and the MCP. However, in our experiment we are interested in detecting ions with the MCP, and there may be a small ($\sim$ 1 ns) difference in the timing registered by the detector using ions as opposed to betas. Moreover, there are uncertainties in the electric field and

[1]It is twice the time since events which hit the MCP first have a negative delay, and those which hit the scintillator first have a positive delay, so the difference between these kinds of events is twice the magnitude of either delay.

MOT position which influence the shape and starting time of the TOF spectrum. For these reasons, we shift our spectrum according to the zero timing peaks, but we still allow the absolute time of the spectrum to float during our fits (see Sections 6.2 and 6.3). Fitting the leading edge of the TOF profile for the two charge states also serves as a consistency check against our measurements for the electric field and MOT-MCP position.

6.1.2 Q-Cut

As mentioned, we use a blend of approaches when extracting the parameter a, including making a rough kinematic reconstruction of the antineutrino's momentum. We do this to make an additional cut on our data rather than directly using this information to calculate the relative angles of the particles. The position sensitivity of the MWPC is a powerful tool in making this cut. We use this position information provided by the MWPC in conjunction with the measured energy of the beta to calculate the momentum of the beta. The time of flight and landing position of the recoil ion determines its momentum and energy as well. Using the conservation of momentum, we can reconstruct the antineutrino's momentum, and therefore its energy. If the sum of the energies of each particle do not sum up close to 3.508 MeV, the respective event is thrown away. We are presently quite conservative with this cut due to the broad energy resolution of the scintillator. Shown in Figure 6.6a is the plot of Q-values obtained in our data set. The two charge states are not entirely resolved in time (the region of overlap corresponds to the overlap in the time of flight seen in the triangles of Figure 6.4), so in reconstructing Q we make no assumptions about the initial charge state for each event. Shown in Figure 6.6 are the histograms obtained by a projection onto each axis. We fit these histograms to Gaussians and eliminate any event which falls outside the 3σ region. Shown in Figure 6.7 is a plot of the Q-value obtained for each event we have accepted in our data. After applying the

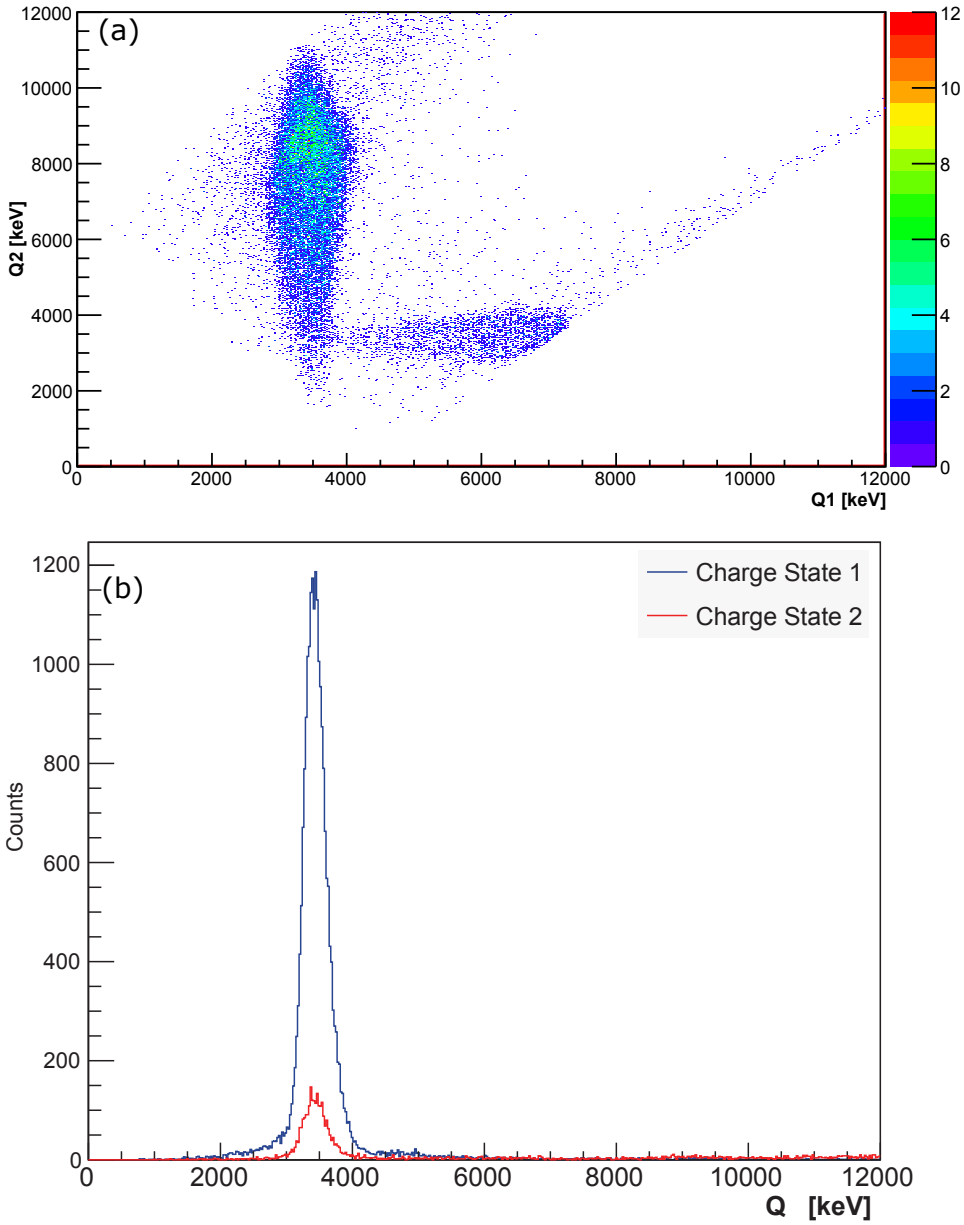

Figure 6.6: (a) Q-value reconstructions obtained for each event in our data set. Each axis represents the reconstructed Q under the assumption of a singly-charged (Q1) or doubly-charged ion (Q2). (b) Projections of (a) onto each charge state axis centered around 3.5 MeV, showing good agreement with the expected Q-value.

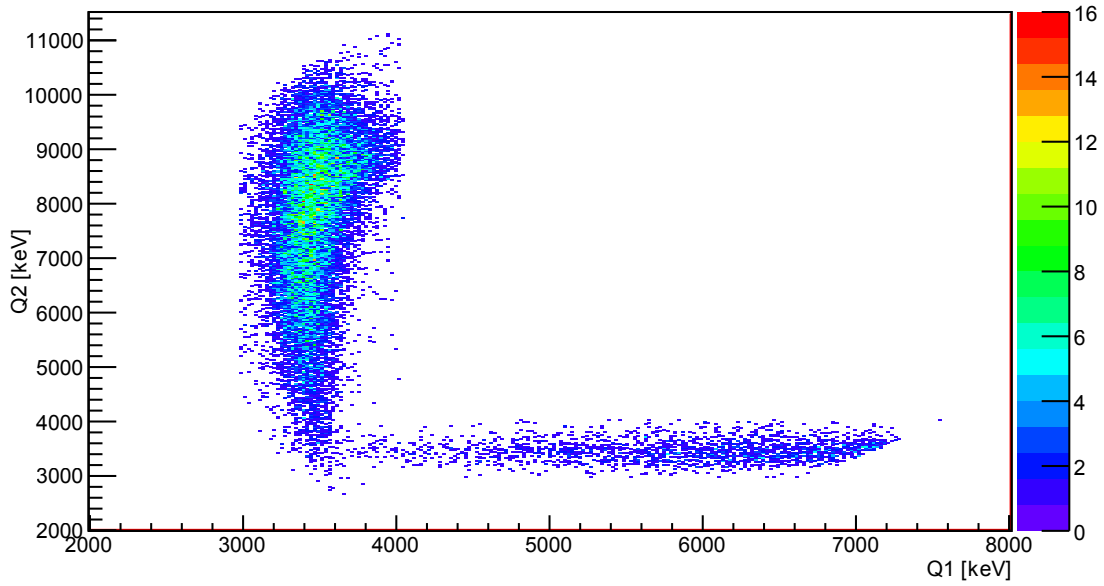

Figure 6.7: Accepted events from Fig. 6.6a after performing the Q-cut procedure.

Q-cut to our data, the diffuse background events which lie outside the triangles were almost entirely eliminated. Figure 6.8 shows the data after this additional filtering.

6.2 Fitting methods for $a_{\beta\nu}$

To extract the parameter a from our filtered data set, we must compare the recorded time of flight distribution to spectra generated by Monte Carlo simulation. The simulation workflow is separated into several steps. We first generate beta events by applying an acceptance-rejection algorithm to the beta decay rate function

$$\frac{d\Gamma}{dE_e d\Omega} \sim F(E_e, Z) p_e E_e (E_0 - E_e)^2 \left[1 + b_{\text{Fierz}} \frac{m_e}{E_e} + a_{\beta\nu} \frac{p_e}{E_e} \cos\theta\right] \tag{6.1}$$

where $F(E_e, Z)$ is the Fermi function for this nucleus, E_0 is the total energy released

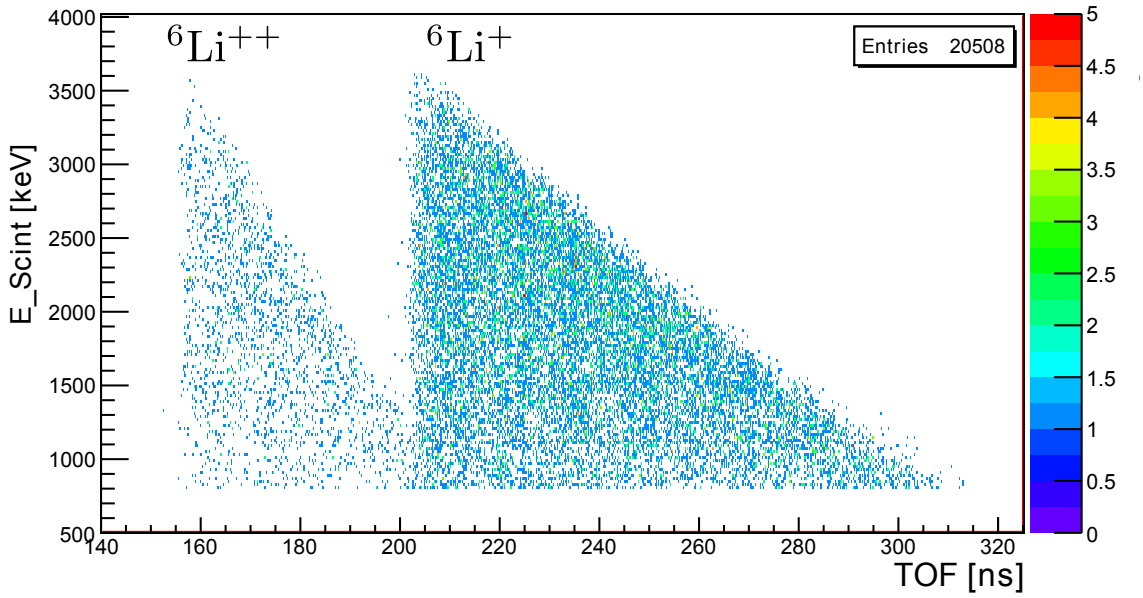

Figure 6.8: 2D plot of the recoil ion TOF vs. the β energy as read by the scintillator-PMT after additional filtering with a Q-cut. Spurious background events outside the two triangular regions as seen in Figure 6.4 are largely eliminated.

in the decay, b_{Fierz} is the Fierz interference term, which is variable but assumed to be zero for these simulations, $a_{\beta\nu}$ is the angular correlation coefficient, and θ is the angle between the beta and the antineutrino. These beta events are propagated throughout a realistic geometry using GEANT4 which tracks all primary and secondary particles generated during scattering events. This includes beta scattering and straggling due to the 127 μm Be foil separating the trap volume from the beta telescope. It is here where we include information about the size, shape, and location of the trapped atoms.

In a separate module, recoil ions are generated using the momentum information generated by the beta event module. These are then tracked according to the electric field map generated by COMSOL (see Section 5.4) onto a simulated recoil detector

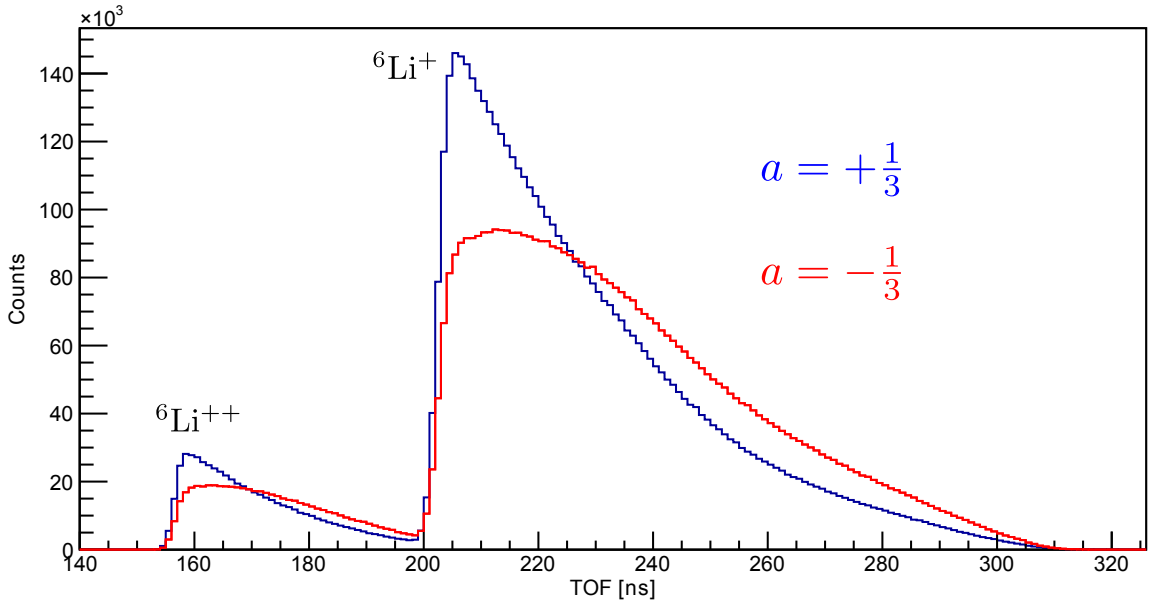

Figure 6.9: Monte Carlo simulations for the recoil ^{6}Li ion TOF spectra. These simulations were run using the known experimental conditions at the time of the February 2015 data run. The blue spectrum corresponds to a purely Tensor interaction, and the red spectrum corresponds to a purely Axial-Vector interaction, which is predicted by the Standard Model.

which yields a final simulated time of flight distribution. By separating these modules, we can track the recoil ions under many different electric field configurations to test the systematic effects of voltage fluctuations and non-uniformity without having to rerun the much more time consuming beta event generation and tracking module.

After folding in measured experimental features such as detector response, efficiency maps, and applying fiducial and energy threshold cuts, we can combine the information from both modules to generate simulated time of flight spectra. Shown in Figure 6.9 are time of flight spectra generated assuming either purely Tensor interactions ($a = +1/3$) or purely Axial-Vector interactions ($a = -1/3$). A linear combination of these "parent" spectra is made to best fit the experimental data, with

the resulting parameter a being the weighted average of the linear coefficients found to minimize the χ^2/dof.

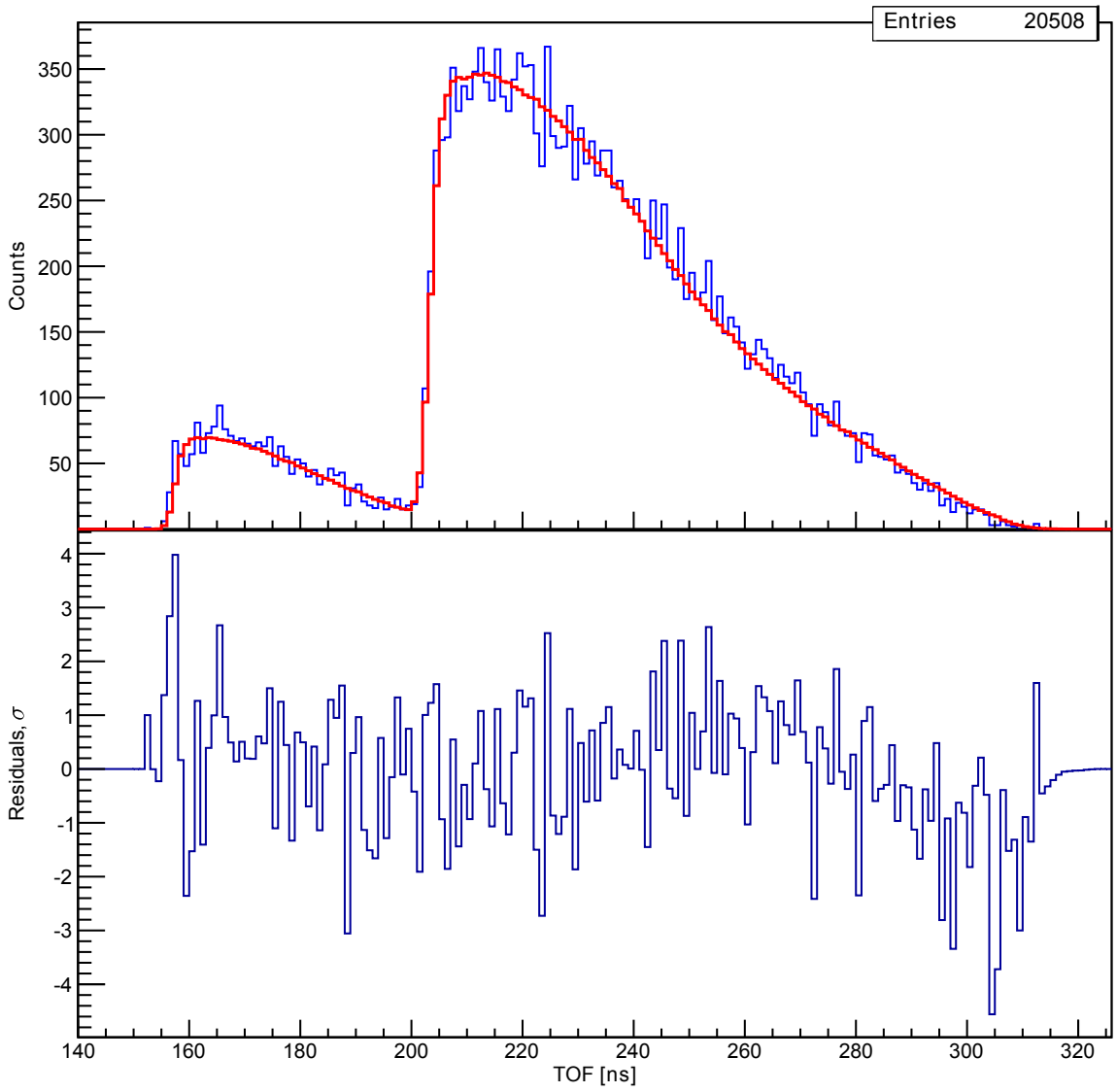

Figure 6.10: Top: Data with fit. Bottom: Residuals showing distortions at larger times of flight as well as a mismatch at the leading edge of the $^6Li^{++}$ events. χ^2/dof= 275/155.

6.3 Fit Results

Figure 6.10 shows the results of the fit to our February data. In the fitting procedure, the rising edge of the primary charge state in the simulated spectra is allowed to float within some defined range (typically 2 ns) to better match the rising edge of the data. After this procedure, the analyzer makes the fit via the linear combination. In the case of this fit, this timing shift amounted to less than 1 ns, showing good agreement between the ion transport times in our simulation and our experiment after having shifted the time using the zero timing peaks. The resulting value for a from this fit is

$$a = -0.278 \pm 0.015(\text{stat}) \tag{6.2}$$

This differs from the predicted value of $a = -1/3$ by $\sim 3.7\sigma$, however it's important to stress that the mean value extracted is not yet reliable at this point in that many important corrections were not considered. At the time that this data was taken, we were using an MCP unit that showed some damage. From the MCP data, it could be seen that there was non-uniformity in the efficiency of that MCP, and in particular there was a region near the edge which had far fewer events than expected assuming a uniform efficiency (see Figure 6.11). This non-uniformity is not present in the MCP we will use in the next data run, and has not been folded into the simulation used to extract the quoted value for a. We are still working to understand the systematic effect of uncertainties in the MCP uniformity on our value for a. The number of events per MCP bin were fairly small, so simply scaling the simulations to match this efficiency map introduces a large bias and in practice the fit is made poorer in doing so. We will need higher MCP statistics to properly fold the efficiency map into the simulation. Additionally, the residuals in Figure 6.10 show deviations near the leading edge of the $^6Li^{++}$ events as well as the tail of the TOF spectrum. This is still under investigation, but this indicates that we'll need to more carefully perform calibrations on our apparatus before we can trust our results. This is also reflected in the fit by the

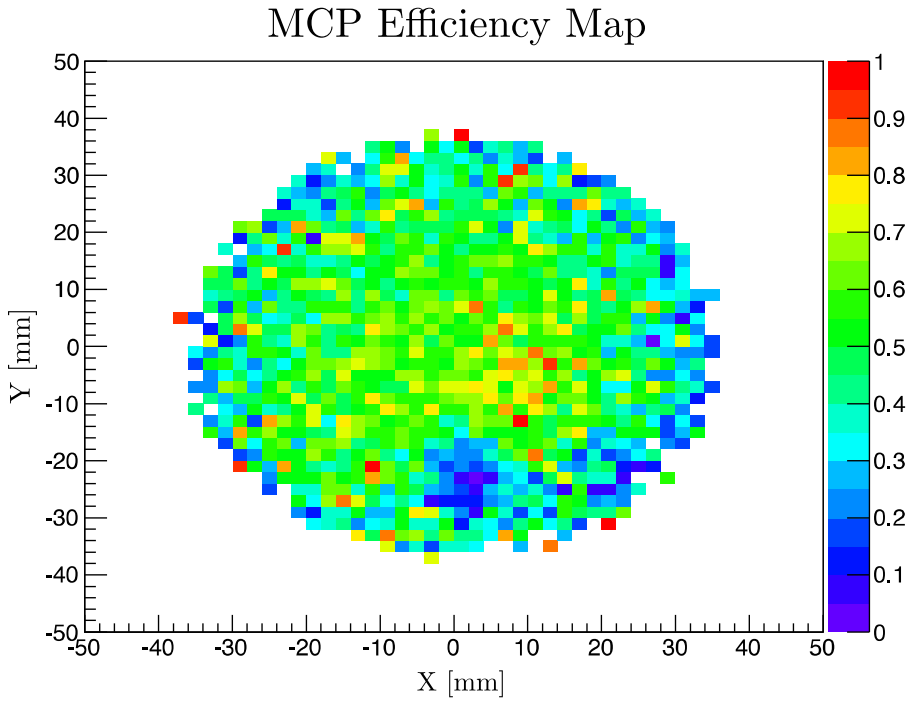

Figure 6.11: MCP efficiency map with ^{6}Li ions. A "hole" is present near the bottom of the MCP which likely introduces a significant distortion unaccounted for in the simulations used to fit the parameter a. We have since replaced this MCP with a newer one which has been calibrated for our next run (see Sec 5.3).

reduced χ^2 of 275/155. We are also in the process of subtracting the background using high-statistics measurements taken by filling our chamber with ^{6}He and measuring the associated coincidence events. There may be systematic uncertainties associated with this process which will need to be quantified.

This preliminary work amounts to a 4.5% measurement of $a_{\beta\nu}$ with just over 20,000 triple-coincidence events after cuts. In an upcoming run we plan to achieve a 1% statistical measurement, which will require just over 400,000 events after cuts. This run will serve as further guidance towards our final goal of a 0.1% measurement, and will incorporate a newly built recirculation system which is expected to boost our

capture efficiency and therefore our triple-coincidence rate by a factor of 3 or more (see Section 4.3 for a discussion on the past performance of such recirculation). This should provide a triple-coincidence rate of > 1 Hz, which amounts to < 85 hours of integrated beam time for the 1% measurement.

6.4 Studied Systematics

We are also actively working to understand the various systematic effects which might influence our results. Table 6.1 contains a list of systematic uncertainties for which we have present estimates. This list is not exhaustive and is a work in progress. I will briefly highlight our approach to how we study some of these systematics. We rely

$\beta-$Threshold = 800 keV	$\delta a/\delta x$	$(\delta a/\delta x)/a$	δx	$\Delta a/a$
MOT − MCP Distance	$-6.7 \times 10^{-5}/100$ μm	$-0.02\%/100$ μm	100 μm	0.02%
MCP Radius	$-5.0 \times 10^{-4}/100$ μm	$-0.15\%/100$ μm	50 μm	0.08%
MOT Radial Position Accuracy	$1.5 \times 10^{-4}/100$ μm	$0.05\%/100$ μm	50 μm	0.02%
MOT Width (Sigma)	$-5.6 \times 10^{-4}/100$ μm	$-0.17\%/100$ μm	50 μm	0.08%
Electrode Voltage Accuracy	1.0×10^{-4}/V	0.03%/V	0.4 V	0.01%
Electrode Spacing	$1.6 \times 10^{-3}/100$ μm	$0.48\%/100$ μm	70 μm	0.34%
Beta Energy Threshold	$4.4 \times 10^{-3}/10$ keV	1.32%/10 keV	2.4 keV	0.32%
Timing Resolution	-7.0×10^{-4}/ns	−0.21%/ns	0.04 ns	0.01%
Scattering				0.07%
Background		−1.2%/1%	0.40%	0.48%
Total				0.68%

Table 6.1: List of studied systematic effects. All effects are computed allowing the leading edge of the time of flight to float as a fitting parameter.

on simulations to inform us of the significance of many systematic effects, including uncertainties in the initial MOT position as well as the electric field strength. Due to the separation of our beta event generator and our ion tracker, both of these effects could be studied without time-intensive resampling of the beta distribution, since the solid angle of the beta detectors changes very little as a function of the MOT position for deviations of order 1 mm. By fitting a line to the extracted $a_{\beta\nu}$ values as a function of the MOT position, we could estimate the systematic effect of this uncertainty. The sensitivity of $a_{\beta\nu}$ to uncertainties in the MOT position amounts to $-0.02\%/100$ μm, as most of the distortion caused by an incorrect position manifests in the first few TOF bins, and this leading edge is allowed to float in our fitting procedure. Figure 6.12 shows the systematic effect of a shifted $Z-$position of the trap with the leading edge fit.

Both the MOT-MCP distance as well as the electric field, assumed here to be uniform in strength (see Section 5.4), influence the time of flight of the recoil ions in ways which are difficult to disentangle without knowing either parameter in absolute terms. Assuming the ions begin at rest, the time of flight to the MCP can be written the following way:

$$\mathrm{TOF} = \sqrt{2m/q}\sqrt{\alpha} + t_0 \tag{6.3}$$

where $\alpha = Z/E_0$, Z is the MOT-MCP distance, and E_0 is the electric field strength.

Section 5.3.2 explained how we can use photoionization to probe the uniformity and absolute strength of the electric field by measuring the time of flight of ionized ^{4}He in reference to prompt UV photon detection. However, this is ultimately measuring α, and it is still necessary to know the initial trap position to get an absolute measurement of this field strength. To make an absolute position measurement, we first carefully measured the distances from the top electrode to the MCP using precision-ground gauge blocks along with precision calipers. Next, a ruler was machined and laser engraved with a pattern of lines and reference marks. The lines were separated by 500 μm, and extra marks separated by 250 μm were placed along each axis for

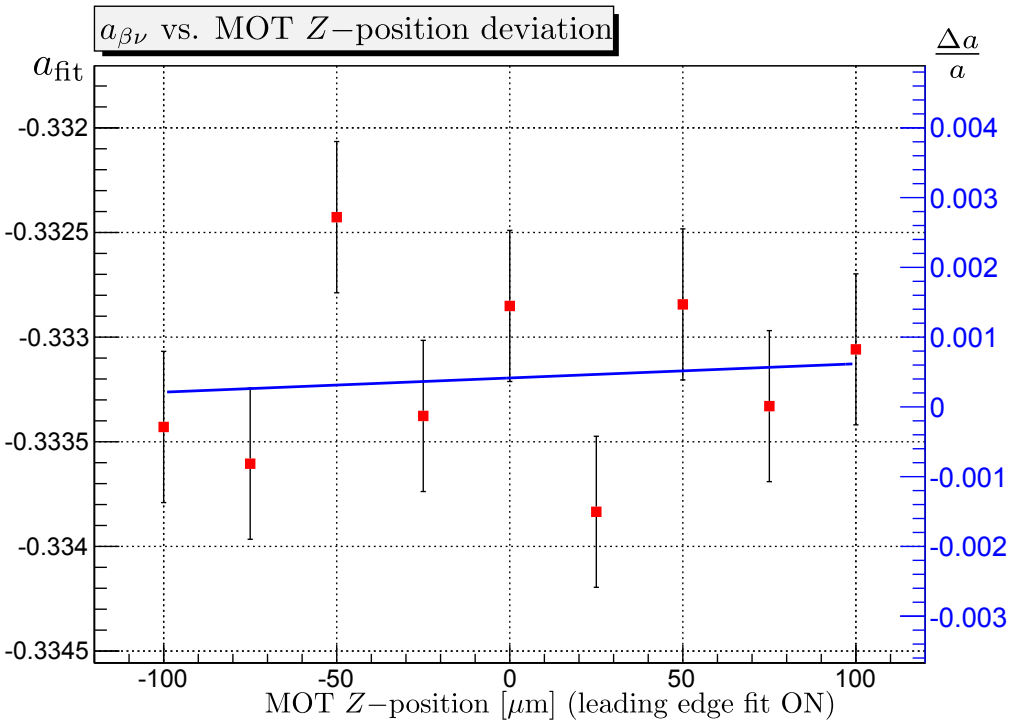

Figure 6.12: Systematic effect on $a_{\beta\nu}$ from uncertainties in the MOT-MCP distance, allowing the leading edge of the TOF spectrum to be a fitting parameter.

additional precision. This ruler was calibrated against a microscope to better than 10 μm. The ruler was then inserted into the top electrode such that the graduated marks could be seen via CCD camera near the center/MOT region of the chamber (see Figure 6.13). This combination allowed for a calibration of the position of the center of the CCD camera with respect to the ruler, and therefore the MCP. This was first tested under air and later under vacuum, and we found no significant deviation in the readings on the CCD.

The background rate due to untrapped atoms we detect is still being determined. During our data run, we split each 12 second cycle into two parts: 9 seconds of foreground data, and 3 seconds of background data. We can use rates of the background data to scale the number of background events we introduce into our simulation to correct for the presence of untrapped atoms on a. To test our simulation, we've taken several high-statistics background runs ($\sim$70,000 events) whereby we flooded our detection chamber with ^{6}He and by-passed the initial trapping stage. To estimate the magnitude of the shift on a from untrapped events, we performed a Monte Carlo simulation of a uniformly diffuse gas along with a central MOT. For every 1% contribution of background to the total number of detected events, a shifted by 1.2% (see Figure 6.14). By comparing the rate of events during background cycles to foreground cycles, we can make a preliminary estimate that the background amounts to $\sim$4% of our data. In principle we can measure the effects of background contributions and perform a background subtraction on our data, but if we conservatively assume we can understand this contribution to 10%, then the estimated systematic uncertainty associated with untrapped atoms is 0.5%.

6.5 Future Improvements

The path towards a 0.1% measurement of $a_{\beta\nu}$ has many obstacles. Each iteration of our experiment is intended to inform us about how we might reduce both our sta-

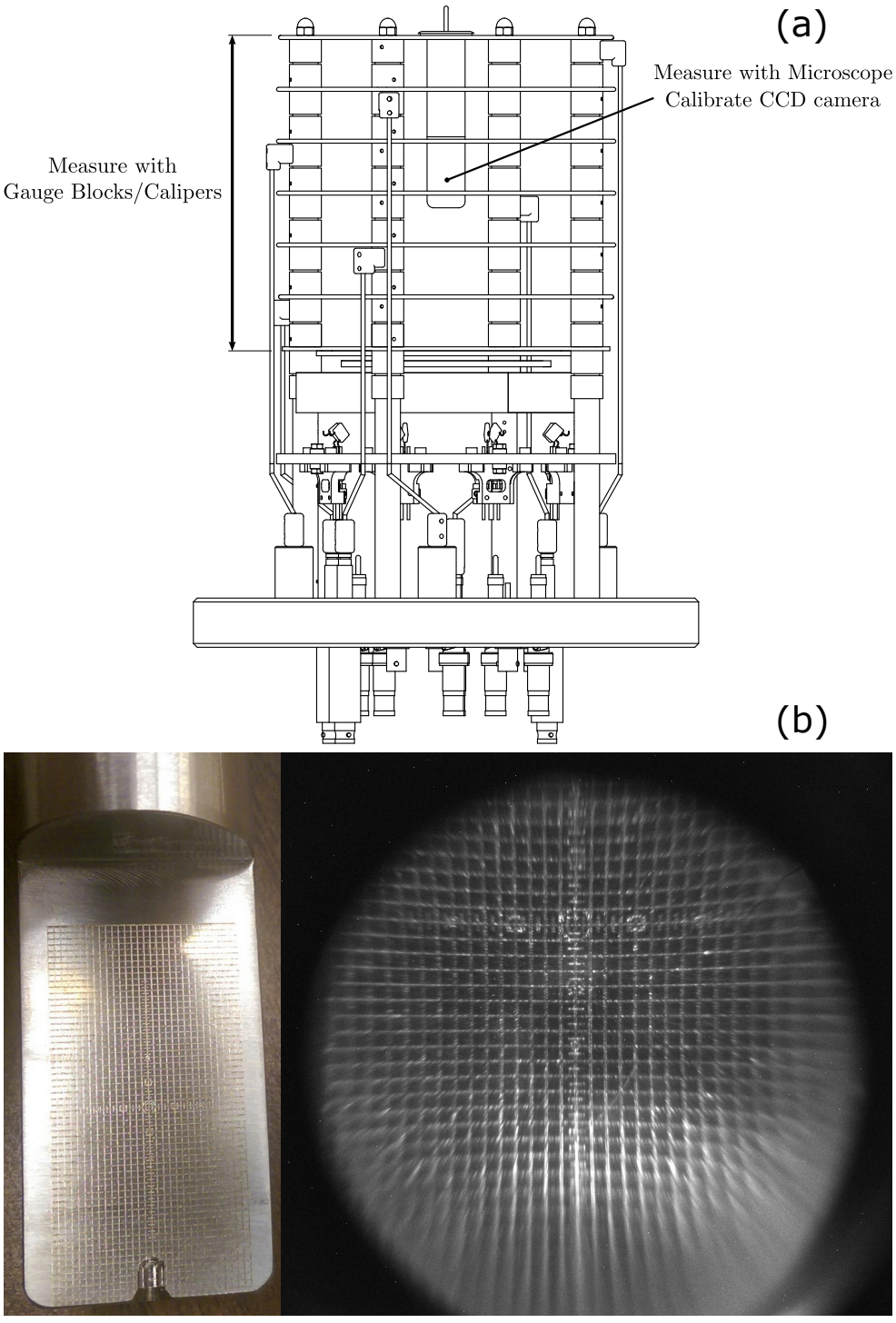

Figure 6.13: Absolute position measurement of the MOT-MCP distance. Panel (a) shows the schematic of the installation of the ruler while panel (b) shows the laser engraved ruler and CCD camera image with an adjustable aperture to precisely measure the MOT position relative to where the ruler was.

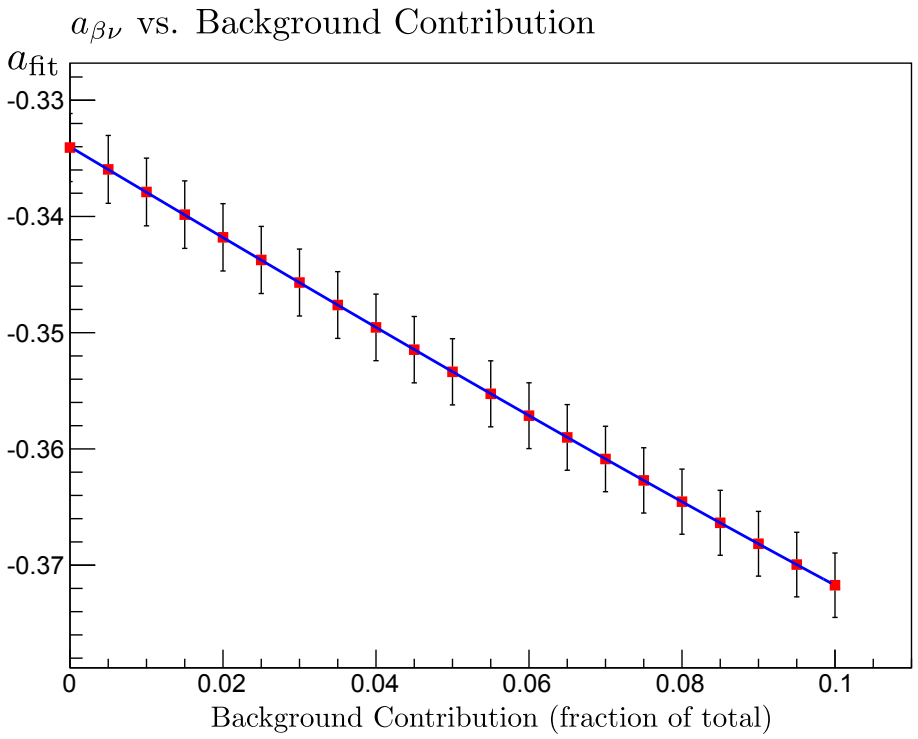

Figure 6.14: Estimation of the systematic effect due to untrapped atoms.

tistical and systematic uncertainties. In addition to the aforementioned recirculation upgrade which we anticipate will yield a data rate increase of a factor of 3, we are presently considering several other improvements to our apparatus.

We presently use a 1.5 inch diameter, 127 μm thick beryllium foil as a separating window between the trap vacuum and the $\beta-$telescope which is under 1 atm of pressure due to the Ar-CO_2 gas used for the MWPC. For our geometry this amounts to a 1.56% solid angle relative to the MOT. To increase our data rate further, we will push to increase this solid angle by at least a factor of two. To offset the increased force exerted on the bonded rim of the foil, we will likely reduce the MWPC gas pressure from 760 Torr to $\sim$50 Torr. This will require a precise gas handling system to monitor the pressure to monitor and minimize gain drifts in the MWPC. We will also consider using a thinner Kapton foil to lower beta backscattering and straggling effects.

Our uncertainty in the electrode spacing which is folded into the electric field uncertainty is presently 70 μm. This is calculated by measuring the individual spacings of each electrode, looking at the distribution of these spacings, and using the rms value as our uncertainty with the mean value used when performing the electric field analysis in COMSOL. However, we will later update the COMSOL simulation to include the individually-measured spacings, which can be measured to within 13 μm using precision-ground gauge blocks or alternatively with modern high-precision laser scanners. This would reduce our uncertainty in a due to unknown electrode spacings from 0.34% to 0.06%.

Given our electric field and MCP radius, we presently capture $\sim$95% of all ^{6}Li recoil ions. There is a significant systematic effect associated with missing some of these recoils which is manifest in our MCP radius cut (see Table 6.1). We believe we can measure the radius of our precisely-manufactured mask (see Section 5.3.1) down to 2 μm, which would reduce this uncertainty, but another approach is to replace our MCP with a MCP large enough, or to increase the electric field strength sufficiently,

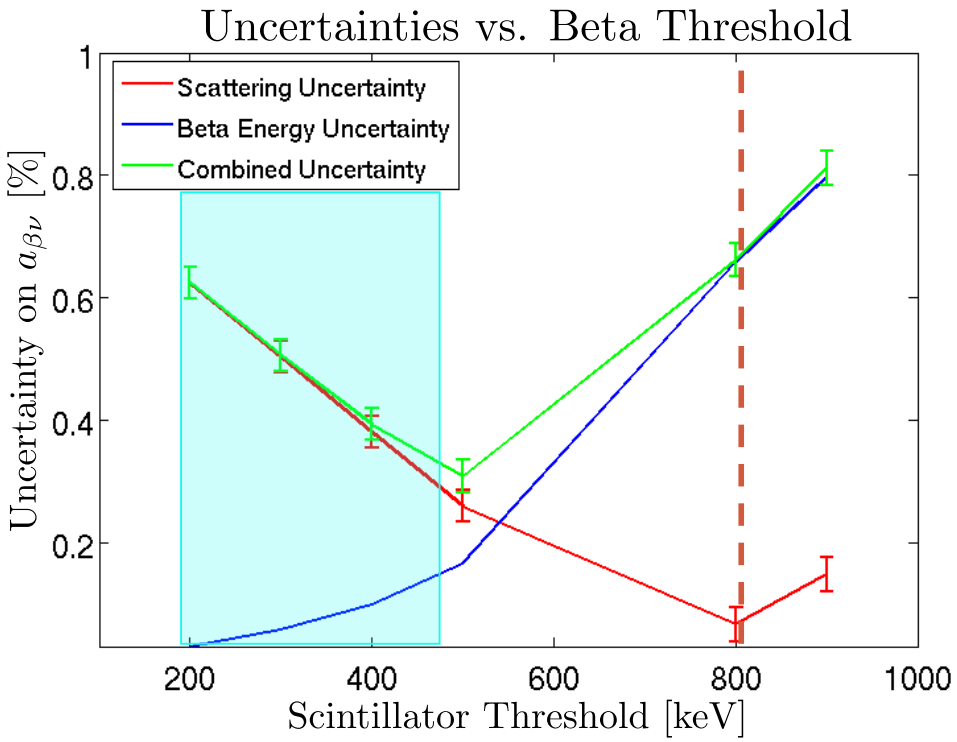

Figure 6.15: Plot of the estimated uncertainties in $a_{\beta\nu}$ due to scattering and beta threshold uncertainty as a function of the beta threshold. The vertical dashed line indicates our current beta threshold, chosen to minimize the effects of scattering. The green line is the combined uncertainty from both effects.

to capture all of the ions.

The systematic effect of the MCP radius cut is also dependent upon the $\beta-$threshold. Lowering the energy threshold of the β detector from 800 keV to 500 keV will decrease the systematic effect of uncertainties in the threshold by a factor of 4, to an overall uncertainty of 0.08%, but it will increase the sensitivity of the MCP radius cut by a factor of 3.65 unless the radius of the MCP is large enough to capture all of the ions.

The effect of β scattering also increases for this lowered energy threshold, presently from 0.07% to 0.26%, though this would be a smaller effect after replacing the beryl-

lium foil and its ring holder assembly with a thinner one, and changing the material for the electrodes from stainless steel to aluminum. This uncertainty assumes we can understand the scattering processes in our simulation to within 10%. Shown in Figure 6.15 is the uncertainty in $a_{\beta\nu}$ introduced by the effects of beta scattering and uncertainties in the beta threshold as a function of the threshold. The combined effects of these uncertainties is presently minimized around 500 keV, so in the future we will lower our threshold from the current value of 800 keV. The blue shaded region indicates the range of beta energy threshold values we will likely select, but we will need to lower the absolute number of scattered events to push below 500 keV. To date we have been using 2 mm stainless steel electrode plates, but we will explore lower Z materials such as gold-plated aluminum to further reduce the effects of β scattering. We may also consider lower Z electrodes made out of glassy carbon (SIGRADUR) rings which have been used in similar experiments by the TRINAT group [23], however glassy carbon is brittle and difficult to handle. In summary, we presented a preliminary analysis but much work remains to yield a precise determination of of $a_{\beta\nu}$ with proper estimations of systematic uncertainties.

Chapter 7

Summary

We developed from scratch a high-intensity source of ^{6}He using the ^{7}Li(d,^{3}He)^{6}He reaction. Deuterons accelerated to 18 MeV at 15 pμA by the in-house Van de Graaff accelerator located at CENPA at the University of Washington undergo a nucleon exchange reaction with lithium to deliver $> 2\times10^{10}$ ^{6}He atoms/s to a low-background experimental room for manipulation. After successive improvements, we can now reliably provide this high yield for weeks at a time.

We precisely measured the half-life of ^{6}He to be $806.89 \pm 0.11_{stat}{}^{+0.23}_{-0.19 syst}$ ms by pumping ^{6}He into a decay volume, measuring the decay rate using two scintillators in coincidence with a scaler-based DAQ, and fitting the shape of the decay spectrum over many cycles. We performed a detailed systematic study to account for uncertainties due to effects such as helium diffusion, detector gain shifts, and others. We also investigated and corrected raw data errors associated with the DAQ system. This represents an improvement in precision over previous experiments by a factor of 6. From this half-life we calculated an $ft-$value of $ft = 803.04^{+0.26}_{-0.23}$ s, and further extracted the Gamow-Teller matrix element of the transition to be $|M_{\mathrm{GT}}| = 2.1645(43)$, which shows agreement within the error estimates of *ab initio* calculations using the weak axial coupling constant g_A measured in free neutron decay.

We have set up a new experiment measuring the electron-neutrino angular cor-

relation, $a_{\beta\nu}$, in the decay of ^{6}He using magneto-optical traps and detectors developed at CENPA. The pure Gamow-Teller nature of this transition makes this decay uniquely sensitive to possible tensor contributions to the weak interaction. The use of a magneto-optical trap provides a cold, pure, backing-free source of localized decays. This precise localization allows for a determination of the initial momentum of the recoiling ^{6}Li ion by measuring its time of flight and landing position on a microchannel plate under the acceleration of a uniform 1.55 kV/cm electric field. The initial momentum of the electron can be determined by a position-sensitive multi-wire proportional chamber in coincidence with a thick scintillator coupled to a photomultiplier tube which measures the beta energy. This allows for a reconstruction of the momentum of invisible antineutrino and therefore allows for a determination of the electron-neutrino angular correlation.

We have coupled our high-intensity source to our MOT and have established ^{6}He trapping. We have taken proof of principle data, and have already recorded about 30,000 $\beta-$Li coincidence events. We have begun to thoroughly calibrate our detectors in preparation for a 1% determination of $a_{\beta\nu}$ ($\sim$400,000 events required). We will use those results to guide our efforts to reduce systematic uncertainties en route to a final 0.1% determination, which would represent an order of magnitude improvement in precision over present limits.

Bibliography

[1] H. Becquerel, *Sur la dispersion du rayonnement du radium dans un champ magnétique*, Comptes rendus de l'Académie des sciences, Paris **130** (1900), pp. 372–376

[2] C. Ellis and W. Wooster, *Average Energy of Disintegration of Radium E*, Proc. Roy. Soc. **A117** (1927) (109)

[3] J. Chadwick, *Possible Existence of a Neutron*, Nature **129** (1932) (3252), p. 312

[4] C. L. Cowan, F. Reines, F. B. Harrison, H. W. Kruse and A. D. McGuire, *Detection of the Free Neutrino: a Confirmation*, Science **124** (1956) (3212), pp. 103–104,
URL: `http://www.sciencemag.org/content/124/3212/103.short`

[5] P. Venkataramaiah, K. Gopala, A. Basavaraju, S. S. Suryanarayana and H. Sanjeeviah, *A simple relation for the Fermi function*, Journal of Physics G: Nuclear Physics **11** (1985) (3), p. 359,
URL: `http://stacks.iop.org/0305-4616/11/i=3/a=014`

[6] T. D. Lee and C. N. Yang, *Question of Parity Conservation in Weak Interactions*, Phys. Rev. **104** (1956), pp. 254–258,
URL: `http://link.aps.org/doi/10.1103/PhysRev.104.254`

[7] C. S. Wu, E. Ambler, R. W. Hayward, D. D. Hoppes and R. P. Hudson, *Experimental Test of Parity Conservation in Beta Decay*, Phys. Rev. **105** (1957), pp. 1413–1415,
URL: `http://link.aps.org/doi/10.1103/PhysRev.105.1413`

[8] B. M. Rustad and S. L. Ruby, *Gamow-Teller Interaction in the Decay of* ^{6}*He*, Phys. Rev. **97** (1955), pp. 991–1002,
URL: http://link.aps.org/doi/10.1103/PhysRev.97.991

[9] W. B. Herrmannsfeldt, D. R. Maxson, P. Stähelin and J. S. Allen, *Electron-Neutrino Angular Correlation in the Positron Decay of Argon 35*, Phys. Rev. **107** (1957), pp. 641–643,
URL: http://link.aps.org/doi/10.1103/PhysRev.107.641.2

[10] W. B. Herrmannsfeldt, R. L. Burman, P. Stähelin, J. S. Allen and T. H. Braid, *Determination of the Gamow-Teller Beta-Decay Interaction from the Decay of Helium-6*, Phys. Rev. Lett. **1** (1958), pp. 61–63,
URL: http://link.aps.org/doi/10.1103/PhysRevLett.1.61

[11] J. S. Allen, *Determination of the Beta-Decay Interaction from Electron-Neutrino Angular Correlation Experiments*, Rev. Mod. Phys. **31** (1959), pp. 791–796,
URL: http://link.aps.org/doi/10.1103/RevModPhys.31.791

[12] N. Severijns, M. Beck and O. Naviliat-Cuncic, *Tests of the standard electroweak model in nuclear beta decay*, Rev. Mod. Phys. **78** (2006), pp. 991–1040,
URL: http://link.aps.org/doi/10.1103/RevModPhys.78.991

[13] N. Severijns, M. Beck and O. Naviliat-Cuncic, *Tests of the standard electroweak model in nuclear beta decay*, Rev. Mod. Phys. **78** (2006), p. 991

[14] J. D. Jackson, S. B. Treiman and H. W. Wyld, *Possible Tests of Time Reversal Invariance in Beta Decay*, Phys. Rev. **106** (1957), pp. 517–521,
URL: http://link.aps.org/doi/10.1103/PhysRev.106.517

[15] J. C. Hardy and I. S. Towner, *Superallowed* $0^+ \to 0^+$ *nuclear* β *decays: A new survey with precision tests of the conserved vector current hypothesis and the standard model*, Phys. Rev. C **79** (2009), p. 055502

[16] C. H. Johnson, F. Pleasonton and T. A. Carlson, *Precision Measurement of the Recoil Energy Spectrum from the Decay of* He^6, Phys. Rev. **132** (1963), pp. 1149–1165,
URL: http://link.aps.org/doi/10.1103/PhysRev.132.1149

[17] F. Glück, *Order-*α *radiative correction to* ^{6}He *and* ^{32}Ar β *decay recoil spectra*, Nuclear Physics A **628** (1998), pp. 493 – 502

[18] T. A. Carlson, *Recoil Energy Spectrum of the Sodium Ions Following the β^- Decay of* Ne^{23}, Phys. Rev. **132** (1963), pp. 2239–2242,
URL: http://link.aps.org/doi/10.1103/PhysRev.132.2239

[19] C. Stratowa, R. Dobrozemsky and P. Weinzierl, *Ratio $|\frac{g_A}{g_V}|$ derived from the proton spectrum in free-neutron decay*, Phys. Rev. D **18** (1978), pp. 3970–3979,
URL: http://link.aps.org/doi/10.1103/PhysRevD.18.3970

[20] V. Egorov, C. Brianon, V. Brudanin, J. Dionisio, J. Deutsch, V. Gorozhankin, Y. Gurov, R. Prieels, V. Sandukovsky, N. Severijns, M. Simoes, Y. Shitov, C. Vieu, V. Vorobel, T. Vylov, I. Yutlandov and S. Zaparov, *Beta-neutrino angular correlation in the decay of 18Ne*, Nuclear Physics A **621** (1997) (3), pp. 745 – 753,
URL: http://www.sciencedirect.com/science/article/pii/S0375947497001784

[21] E. G. Adelberger, C. Ortiz, A. García, H. E. Swanson, M. Beck, O. Tengblad, M. J. G. Borge, I. Martel, H. Bichsel and the ISOLDE Collaboration, *Positron-Neutrino Correlation in the $0^+ \to 0^+$ Decay of* ^{32}Ar, Phys. Rev. Lett. **83** (1999), pp. 1299–1302,
URL: http://link.aps.org/doi/10.1103/PhysRevLett.83.1299

[22] J. Byrne, P. G. Dawber, M. G. D. van der Grinten, C. G. Habeck, F. Shaikh, J. A. Spain, R. D. Scott, C. A. Baker, K. Green and O. Zimmer, *Determination of the electronantineutrino angular correlation coefficient a_0 and the parameter $|\lambda| = |G_A/G_V|$ in free neutron β-decay from measurements of the integrated energy spectrum of recoil protons stored in an ion trap*, Journal of Physics G: Nuclear and Particle Physics **28** (2002) (6), p. 1325,
URL: http://stacks.iop.org/0954-3899/28/i=6/a=314

[23] A. Gorelov, D. Melconian, W. P. Alford, D. Ashery, G. Ball, J. A. Behr, P. G. Bricault, J. M. D'Auria, J. Deutsch, J. Dilling, M. Dombsky, P. Dubé, J. Fingler, U. Giesen, F. Glück, S. Gu, O. Häusser, K. P. Jackson, B. K. Jennings, M. R. Pearson, T. J. Stocki, T. B. Swanson and M. Trinczek, *Scalar Interaction Limits from the $\beta - \nu$ Correlation of Trapped Radioactive Atoms*, Phys. Rev. Lett. **94** (2005), p. 142501,
URL: http://link.aps.org/doi/10.1103/PhysRevLett.94.142501

[24] P. A. Vetter, J. R. Abo-Shaeer, S. J. Freedman and R. Maruyama, *Measurement of the β-ν correlation of* ^{21}Na *using shakeoff electrons*, Phys. Rev. C **77** (2008), p. 035502,
URL: http://link.aps.org/doi/10.1103/PhysRevC.77.035502

[25] X. Fléchard, P. Velten, E. Liénard, A. Méry, D. Rodríguez, G. Ban, D. Durand, F. Mauger, O. Naviliat-Cuncic and J. C. Thomas, *Measurement of the $\beta - \nu$ correlation coefficient $a_{\beta\nu}$ in the β decay of trapped $^6He^+$ ions*, Journal of Physics G: Nuclear and Particle Physics **38** (2011) (5), p. 055101,
URL: `http://stacks.iop.org/0954-3899/38/i=5/a=055101`

[26] G. Li, R. Segel, N. D. Scielzo, P. F. Bertone, F. Buchinger, S. Caldwell, A. Chaudhuri, J. A. Clark, J. E. Crawford, C. M. Deibel, J. Fallis, S. Gulick, G. Gwinner, D. Lascar, A. F. Levand, M. Pedretti, G. Savard, K. S. Sharma, M. G. Sternberg, T. Sun, J. Van Schelt, R. M. Yee and B. J. Zabransky, *Tensor Interaction Limit Derived From the α-β-$\overline{\nu}$ Correlation in Trapped ^{8}Li Ions*, Phys. Rev. Lett. **110** (2013), p. 092502,
URL: `http://link.aps.org/doi/10.1103/PhysRevLett.110.092502`

[27] M. Sternberg, Private communication

[28] J. A. Behr and A. Gorelov, *β-decay angular correlations with neutral atom traps*, Journal of Physics G: Nuclear and Particle Physics **41** (2014) (11), p. 114005,
URL: `http://stacks.iop.org/0954-3899/41/i=11/a=114005`

[29] X. Fléchard, Private communication

[30] F. Wauters, A. García and R. Hong, *Limits on tensor-type weak currents from nuclear and neutron β decays*, Phys. Rev. C **89** (2014), p. 025501,
URL: `http://link.aps.org/doi/10.1103/PhysRevC.89.025501`

[31] A. S. Carnoy, J. Deutsch, T. A. Girard and R. Prieels, *Limits on nonstandard weak currents from the polarization of ^{14}O and ^{10}C decay positrons*, Phys. Rev. C **43** (1991), pp. 2825–2834,
URL: `http://link.aps.org/doi/10.1103/PhysRevC.43.2825`

[32] V. Cirigliano, M. Gonzlez-Alonso and M. Graesser, *Non-standard charged current interactions: beta decays versus the LHC*, Journal of High Energy Physics **2013** (2013) (2), 46

[33] S. Chatrchyan, *Search for leptonic decays of W' bosons in pp collisions at $\sqrt{s} = 7$ TeV*, Journal of High Energy Physics **2012** (2012) (8), 23

[34] R. Raabe, J. Büscher, J. Ponsaers, F. Aksouh, M. Huyse, O. Ivanov, S. R. Lesher, I. Mukha, D. Pauwels, M. Sawicka, D. Smirnov, I. Stefanescu, J. Van de Walle, P. Van Duppen, C. Angulo, J. Cabrera, N. de Séréville, I. Martel, A. M. Sánchez-Benítez and C. A. Diget, *Measurement of the branching ratio of the ^{6}He β-decay channel into the $\alpha + d$ continuum*, Phys. Rev. C **80** (2009), p. 054307

[35] A. Knecht, R. Hong, D. W. Zumwalt, B. G. Delbridge, A. García, P. Müller, H. E. Swanson, I. S. Towner, S. Utsuno, W. Williams and C. Wrede, *Precision measurement of the* ^{6}He *half-life and the weak axial current in nuclei*, Phys. Rev. C **86** (2012), p. 035506

[36] L.-B. Wang, P. Mueller, K. Bailey, G. W. F. Drake, J. P. Greene, D. Henderson, R. J. Holt, R. V. F. Janssens, C. L. Jiang, Z.-T. Lu, T. P. O'Connor, R. C. Pardo, K. E. Rehm, J. P. Schiffer and X. D. Tang, *Laser Spectroscopic Determination of the* ^{6}He *Nuclear Charge Radius*, Phys. Rev. Lett. **93** (2004) (14), p. 142501

[37] I. Tanihata, D. Hirata, T. Kobayashi, S. Shimoura, K. Sugimoto and H. Toki, *Revelation of thick neutron skins in nuclei*, Physics Letters B **289** (1992) (34), pp. 261 – 266,
URL: http://www.sciencedirect.com/science/article/pii/037026939291216V

[38] P. Zucchelli, *A novel concept for a* $\overline{\nu_e}/\nu_e$ *neutrino factory: the beta-beam*, Physics Letters B **532** (2002) (3 - 4), pp. 166 – 172,
URL: http://www.sciencedirect.com/science/article/pii/S0370269302015769

[39] F. Pleasonton and C. H. Johnson, *System for Continuous Generation and Fast Transfer of Radioactive Gases*, Review of Scientific Instruments **35** (1964) (1), pp. 97–102,
URL: http://scitation.aip.org/content/aip/journal/rsi/35/1/10.1063/1.1718717

[40] A. J. Koning and D. Rochman (2015),
URL: http://www-nds.iaea.org/exfor/endf.htm

[41] T. Stora, E. Noah, R. Hodak, T. Y. Hirsh, M. Hass, V. Kumar, K. Singh, S. Vaintraub, P. Delahaye, H. Franberg-Delahaye, M.-G. Saint-Laurent and G. Lhersonneau, *A high intensity* ^{6}*He beam for the* β*-beam neutrino oscillation facility*, EPL (Europhysics Letters) **98** (2012) (3), p. 32001,
URL: http://stacks.iop.org/0295-5075/98/i=3/a=32001

[42] Alfa Aesar (2011),
URL: http://www.alfa.com/en/GP100w.pgm?DSSTK=010773

[43] K. B. Swartz, D. W. Visser and J. M. Baris, *A Java-based data acquisition system for nuclear physics*, Nucl. Instrum. Methods A **463** (2001) (1-2), pp. 354 – 360

[44] J. Sempau, E. Acosta, J. Baro, J. M. Fernandez-Varea and F. Salvat, *An algorithm for Monte Carlo simulation of coupled electron-photon transport*, Nucl. Instrum. Methods B **132** (1997) (3), pp. 377 – 390

[45] J. F. Ziegler, *SRIM-2008* (2011),
URL: `http://www.srim.org/`

[46] A. H. Wuosmaa, J. P. Schiffer, K. E. Rehm, J. P. Greene, D. J. Henderson, R. V. F. Janssens, C. L. Jiang, L. Jisonna, J. C. Lighthall, S. T. Marley, E. F. Moore, R. C. Pardo, N. Patel, M. Paul, D. Peterson, S. C. Pieper, G. Savard, R. E. Segel, R. H. Siemssen, X. D. Tang and R. B. Wiringa, *Structure of* ^{7}He *by proton removal from* ^{8}Li *with the (d,*^{3}He*) reaction*, Phys. Rev. C **78** (2008) (4), p. 041302

[47] R. H. Stokes and P. G. Young, *Search for Excited States of* ^{6}He, Phys. Rev. C **3** (1971) (3), pp. 984–991

[48] L. L. Shreir, *Corrosion: Metal/Environment Reactions* (Newnes-Butterworths, 1976)

[49] LabVIEW System Design Software,
URL: `http://www.ni.com/labview/`

[50] A. Knecht, D. Zumwalt, B. Delbridge, A. García, G. Harper, R. Hong, P. Müller, A. Palmer, R. Robertson, H. Swanson, S. Utsuno, D. Will, W. Williams and C. Wrede, *A high-intensity source of* ^{6}He *atoms for fundamental research*, Nuclear Instruments and Methods in Physics Research Section A: Accelerators, Spectrometers, Detectors and Associated Equipment **660** (2011) (1), pp. 43 – 47

[51] F. Landré-Pellemoine, J. Angelique, O. Bajeat, C. Barué, R. Bennett, F. Clapier, M. Ducourtieux, G. Gaubert, S. Gibouin, Y. Huguet, P. Jardin, S. Kandri-Rody, C. Lau, N. Lecesne, R. Leroy, M. Lewitowicz, R. Lichtenthäler, C. Marry, L. Maunoury, J. Obert, N. Orr, J. Pacquet, M. Saint-Laurent, C. Stodel, J. Rataud and A. Villari, *Recent results at the SIRa test bench: Diffusion properties of carbon graphite and B4C targets*, Nuclear Physics A **701** (2002) (1-4), pp. 491 – 494

[52] P. Müller, L. B. Wang, K. Bailey, G. W. F. Drake, X. Du, J. Greene, A. M. Heinz, R. J. Holt, D. Henderson, R. V. Janssens, C. L. Jiang, C. Law, Z. T. Lu, I. D. Moore, T. P. O'Connor, R. C. Pardo, M. Paul, T. Pennington, K. E.

Rehm and J. P. Schiffer, *Towards measuring the charge radius of* ^{6}He *and* ^{8}He, Nucl. Instrum. Methods B **204** (2003), pp. 536 – 539

[53] X. Fléchard, E. Liénard, A. Méry, D. Rodríguez, G. Ban, D. Durand, F. Duval, M. Herbane, M. Labalme, F. Mauger, O. Naviliat-Cuncic, J. C. Thomas and P. Velten, *Paul Trapping of Radioactive* ^{6}He$^+$ *Ions and Direct Observation of Their* β *Decay*, Phys. Rev. Lett. **101** (2008) (21), p. 212504

[54] J. B. Vise and B. M. Rustad, *Electron-Neutrino Angular Correlation in the Decay of* ^{6}He, Phys. Rev. **132** (1963) (6), pp. 2573–2581

[55] F. Pleasonton and C. H. Johnson, *System for Continous Generation and Fast Transfer of Radioactive Gases*, Rev. Sci. Instrum. **35** (1964), p. 97

[56] F. Ajzenberg-Selove, *Energy levels of light nuclei A = 5 – 10*, Nuclear Physics A **413** (1984), p. 1

[57] D. E. Alburger, *Half-life of* ^{6}He, Phys. Rev. C **26** (1982), p. 252

[58] T. Lauritsen and F. Ajzenberg-Selove, *Energy levels of light nuclei (VII). A = 5 – 10*, Nuclear Physics **78** (1966), p. 1, this reference compiles all ^{6}He half-life measurements before 1966

[59] R. M. Kline and D. J. Zaffarano, *Decay Characteristics of Some Short-Lived Nuclides of Low Atomic Number*, Phys. Rev. **96** (1954), p. 1620

[60] J. K. Bienlein and F. Pleasonton, *The half-life of* ^{6}He, Nuclear Physics **37** (1962), p. 529

[61] D. H. Wilkinson and D. E. Alburger, *Half-lives of* ^{6}He*,* ^{19}Ne*, and* ^{42}Sc^m, Phys. Rev. C **10** (1974), p. 1993

[62] P. H. Barker, T. B. Ko and M. J. Scandle, *The half-life of* ^{6}He, Nuclear Physics A **372** (1981), p. 45

[63] D. Anthony *et al.*, β*-delayed deuteron emission from* ^{6}He, Phys. Rev. C **65** (2002), p. 034310

[64] K. Kubodera and M. Rho, *Effective Field Theory and High-Precision Calculations of Nuclear Electroweak Processes* (2011)

[65] S. C. Pieper and R. B. Wiringa, *QUANTUM MONTE CARLO CALCULATIONS OF LIGHT NUCLEI*, Ann. Rev. Nucl. Part. Sci. **51** (2001), p. 53

[66] P. F. Bedaque and U. van Kolck, *Effective field theory for few-nucleon systems* , Ann. Rev. Nucl. Part. Sci. **52** (2002), p. 339

[67] P. Navrátil and W. E. Ormand, *Ab initio shell model with a genuine three-nucleon force for the p-shell nuclei*, Phys. Rev. C **68** (2003), p. 034305

[68] B. A. Brown and B. H. Wildenthal, *Experimental and Theoretical Gamow-Teller Beta-Decay Observables for the sd-Shell Nuclei*, Atom. Data Nucl. Data **33** (1985), p. 347

[69] W.-T. Chou, E. K. Warburton and B. A. Brown, *Gamow-Teller beta-decay rates for $A \leq 18$ nuclei*, Phys. Rev. C **47** (1993), p. 163

[70] F. Osterfeld, *Nuclear spin and isospin excitations*, Rev. Mod. Phys. **64** (1992), p. 491

[71] J. Rapaport and E. Sugarbaker, *Isovector Excitations in Nuclei*, Ann. Rev. Nucl. Part. Sci. **44** (1994), p. 109

[72] E. Caurier, A. Poves and A. P. Zuker, *Missing and Quenched Gamow-Teller Strength*, Phys. Rev. Lett. **74** (1995), pp. 1517–1520

[73] W. C. Haxton and C.-L. Song, *Morphing the Shell Model into an Effective Theory*, Phys. Rev. Lett. **84** (2000), p. 5484

[74] J. Menéndez, D. Gazit and A. Schwenk, *Chiral Two-Body Currents in Nuclei: Gamow-Teller Transitions and Neutrinoless Double-Beta Decay*, Phys. Rev. Lett. **107** (2011), p. 062501

[75] R. Schiavilla and R. B. Wiringa, *Weak transitions in $A = 6$ and 7 nuclei*, Phys. Rev. C **65** (2002), p. 054302

[76] M. Pervin, S. C. Pieper and R. B. Wiringa, *Quantum Monte Carlo calculations of electroweak transition matrix elements in $A = 6, 7$ nuclei*, Phys. Rev. C **76** (2007), p. 064319

[77] S. Vaintraub, N. Barnea and D. Gazit, ^{6}He *β-decay rate and the suppression of the axial constant in nuclear matter*, Phys. Rev. C **79** (2009), p. 065501

[78] ROOT Data analysis framework,
URL: http:/http://root.cern.ch/drupal/

[79] X. Fléchard *et al.*, *"Measurement of the* ^{8}Li *half-life"*, Phys. Rev. C **82** (2010), p. 027309

[80] G. F. Knoll, *Radiation detection and measurement* (New York: Wiley, 2000)

[81] A. P. Baerg, *Variation on the Paired Source Method of Measuring Dead Time*, Metrologia **1** (1963), p. 131

[82] G. F. Grinyer *et al.*, *High precision measurements of* ^{26}*Na* β^- *decay*, Phys. Rev. C **71** (2005), p. 044309

[83] R. M. Barrer, *Diffusion in and Through Solids*, Cambridge University Press, Cambridge (1941)

[84] P. Sturm, M. Leuenberger, C. Sirignano, R. E. M. Neubert, H. A. J. Meijer, R. Langenfelds, W. A. Brand and Y. Tohjima, *Permeation of atmospheric gases through polymer O-rings used in flasks for air sampling*, Journal of Geophysical Research: Atmospheres **109** (2004) (D4), pp. n/a–n/a,
URL: http://dx.doi.org/10.1029/2003JD004073

[85] S. J. Schowalter, C. B. Connolly and J. M. Doyle, *Permeability of noble gases through Kapton, butyl, nylon, and Silver Shield*, Nuclear Instruments and Methods in Physics Research Section A: Accelerators, Spectrometers, Detectors and Associated Equipment **615** (2010) (3), pp. 267 – 271,
URL: http://www.sciencedirect.com/science/article/pii/S0168900210001099

[86] National Institute of Standards and Technology NIST,
URL: http://nist.time.gov

[87] M. Brodeur, T. Brunner, C. Champagne, S. Ettenauer, M. J. Smith, A. Lapierre, R. Ringle, V. L. Ryjkov, S. Bacca, P. Delheij, G. W. F. Drake, D. Lunney, A. Schwenk and J. Dilling, *First Direct Mass Measurement of the Two-Neutron Halo Nucleus* ^{6}He *and Improved Mass for the Four-Neutron Halo* ^{8}He, Phys. Rev. Lett. **108** (2012), p. 052504

[88] B. J. Mount, M. Redshaw and E. G. Myers, *Atomic masses of* ^{6}Li,^{23} Na,^{39,41} K,^{85,87} Rb*, and* ^{133}Cs, Phys. Rev. A **82** (2010), p. 042513

[89] G. Audi, A. Wapstra and C. Thibault, *The* AME*2003 atomic mass evaluation: (II). Tables, graphs and references*, Nuclear Physics A **729** (2003) (1), p. 337

[90] S. Cohen and D. Kurath, *Effective interactions for the 1p shell*, Nuclear Physics **73** (1965), p. 1

[91] E. K. Warburton and B. A. Brown, *Effective interactions for the 0p1s0d nuclear shell-model space*, Phys. Rev. C **46** (1992), p. 923

[92] B. R. Holstein, *Recoil effects in allowed beta decay: The elementary particle approach*, Rev. Mod. Phys. **46** (1974), p. 789

[93] TUNL Nuclear Data Evaluation Project,
URL: `http://www.tunl.duke.edu/nucldata/`

[94] H. J. Metcalf and P. van der Straten, *Laser Cooling and Trapping* (Springer, 1999)

[95] C. J. Foot, *Atomic Physics* (Oxford University Press, 2005)

[96] S. S. Hodgman, R. G. Dall, L. J. Byron, K. G. H. Baldwin, S. J. Buckman and A. G. Truscott, *Metastable Helium: A New Determination of the Longest Atomic Excited-State Lifetime*, Phys. Rev. Lett. **103** (2009), p. 053002

[97] n. F. Pereira Dos Santos, F. Perales, J. Lonard, A. Sinatra, J. Wang, F. S. Pavone, E. Rasel, C. S. Unnikrishnan and M. Leduc, *Efficient magneto-optical trapping of a metastable helium gas*, The European Physical Journal - Applied Physics **14** (2001), pp. 69–76

[98] C. Y. Chen, K. Bailey, Y. M. Li, T. P. OConnor, Z.-T. Lu, X. Du, L. Young and G. Winkler, *Beam of metastable krypton atoms extracted from a rf-driven discharge*, Review of Scientific Instruments **72** (2001) (1), pp. 271–272

[99] L. Wang, *Determination of the* ^{6}He *Nuclear Charge Radius using High-Resolution Laser Spectroscopy* (2004)

[100] W. D. Phillips and H. Metcalf, *Laser Deceleration of an Atomic Beam*, Phys. Rev. Lett. **48** (1982), pp. 596–599,
URL: `http://link.aps.org/doi/10.1103/PhysRevLett.48.596`

[101] P. Mueller, I. A. Sulai, A. C. C. Villari, J. A. Alcántara-Núñez, R. Alves-Condé, K. Bailey, G. W. F. Drake, M. Dubois, C. Eléon, G. Gaubert, R. J. Holt, R. V. F. Janssens, N. Lecesne, Z.-T. Lu, T. P. O'Connor, M.-G. Saint-Laurent, J.-C. Thomas and L.-B. Wang, *Nuclear Charge Radius of* ^{8}He, Phys. Rev. Lett. **99** (2007), p. 252501,
URL: http://link.aps.org/doi/10.1103/PhysRevLett.99.252501

[102] D. W. Preston, *Dopplerfree saturated absorption: Laser spectroscopy*, American Journal of Physics **64** (1996) (11), pp. 1432–1436

[103] J. H. Shirley, *Modulation transfer processes in optical heterodyne saturation spectroscopy*, Opt. Lett. **7** (1982) (11), pp. 537–539

[104] B. E. A. Saleh and M. C. Teich, *Fundamentals of Photonics* (John Wiley and Sons, Inc., 1991)

[105] G. Ritt, G. Cennini, C. Geckeler and M. Weitz, *Laser frequency offset locking using a side of filter technique*, Applied Physics B **79** (2004) (3), pp. 363–365

[106] Eljen Technology EJ-200 Scintillator,
URL: http://www.eljentechnology.com/index.php/component/content/article/31-general/48-ej-200

[107] R. Hong, *In preparation* (2015)

[108] R. H. GmbH,
URL: http://www.roentdek.com/products/detectors/

[109] Hamamatsu, *MCP Assembly Guide*,
URL: http://www.triumf.ca/sites/default/files/Hamamatsu MCP guide.pdf

[110] T. A. Carlson, F. Pleasonton and C. H. Johnson, *Electron Shake Off following the* β^- *Decay of* ^{6}He, Phys. Rev. **129** (1963), pp. 2220–2226,
URL: http://link.aps.org/doi/10.1103/PhysRev.129.2220

[111] MACOR®Machinable Glass Ceramic, Corning, Inc.,
URL: http://www.corning.com/specialtymaterials/macor

[112] COMSOL AC/DC Module,
URL: http://www.comsol.com/acdc-module

[113] P. R. Bevington and D. K. Robinson, *Data Reduction and Error Analysis, 3rd Edition* (McGraw Hill Higher Education, 2003)

[114] L. de physique corpusculaire (LPC-Caen), *Fast Acquisition System for nuclEar Research (FASTER)*,
URL: `http://faster.in2p3.fr/`